INVESTIGATION OF NONLINEAR CRACK TIP DEFORMATION INCLUDING THE EFFECTS OF UNSYMMETRIC SPATIAL VARIATIONS OF MATERIAL PROPERTIES

by

Prasad K. Nair

Dissertation submitted to the Graduate Faculty of the
Virginia Polytechnic Institute and State University
in partial fulfillment of the requirements for the degree of
DOCTOR OF PHILOSOPHY
in
Engineering Mechanics

APPROVED:

K. L. Reifsnider, Chairman

D. Frederick

G. Swift

C. W. Smith

D. Mook

C. B. Ling

May, 1974

Blacksburg, Virginia

ACKNOWLEDGEMENT

This work was supported in part by the Department of Defense, U. S. Army Contract No. DAA-F07-69-C-0444. The author wishes to thank Dr. Kenneth L. Reifsnider of the Department of Engineering Science and Mechanics for his guidance and time spent in consultation. Also, thanks to Dr. G. Swift and the department's research facilities for their help during this work period.

TABLE OF CONTENTS

LIST OF FIGURES

INTRODUCTION

There is substantial need to know more about the nonlinear deformation behavior near crack tips, especially for real material situations. The most obvious motivation is provided by questions concerning the (stable or unstable) motion of cracks, for although elastic singular stress analysis may enjoy reasonable success in the description of static stress fields, crack extension in any form will involve local plasticity in engineering materials. For fatigue extension, for example, the local plasticity is thought to be controlling. Moreover, real materials are commonly welded, forged, riveted, joined, heat treated or otherwise affected by manufacturing and service so that ideal laboratory materials are rather unsatisfactory representations of them in general. Local crack tip nonlinear deformation fields would certainly be expected to be sensitive to local variations of material properties (such as yield strength) for example. The engineering consequences of a more careful examination of nonlinear crack tip behavior might appear in the context of crack arrest, or crack initiation and propagation at welds and joints, or the direction of (running or fatigue) crack propagation in composite materials, or more simply, the prediction of a correct stress and strain intensity factor.

Research in fracture mechanics has provided important progress in the understanding of crack extensional problems. Current fracture

mechanics research focuses attention on how to correlate crack extension behavior in sub-critical growth by fatigue or stress corrosion or in critical growth due to an overload, in terms of parameters from analytical solutions which characterize the near tip stress field. In an elastic system, the above mentioned correlation is in terms of the elastic stress intensity factor. It serves to characterize the influence of applied loads and flaw geometry on the near tip field for small scale yielding conditions.

Crack extension behavior is always accompanied by a crack tip plastic zone. The size of the plastic zone depends on the material characteristics and load level. Elastic analysis is not wholly valid near the plastic zone. Larsson and Carlsson [1] have shown recently that the range of validity of the "small scale yielding" assumptions for crack tip plastic zones is much more limited than previously expected. Rice [2] has discussed the existence of non-singular stresses at the crack tip, in order to account for the shortcomings of "small scale yielding" approximations. In that case, there is no single parameter which can uniquely characterize the near crack tip field.

The development of stress intensity factors for various types of specimens and loadings has been the keynote of fracture mechanics analysis. In all such analyses, uniform material properties are assumed. Also, the single parameter characterization of fracture, i.e., Irwin's stress intensity factor is most reliable for brittle fracture.

An extensive amount of literature exists on the subject of deformation fields near crack tips. Although linear elastic considerations are preponderant in that body of literature, nonlinear elastic, elastic-plastic, and elasto-plastic considerations are receiving increasing attention. Of particular interest are the discussions of near-tip plastic stress and strain fields in hardening materials provided by Hutchinson [3, 4] and Rice and Rosengren [5], and the plastic intensity factors for cracked plates described by Hilton and Hutchenson [6]. Most recently, Knowles and Sternberg [7] and McGowan and Smith [8] have considered the finite-deformation elastostatic field near the tip of a crack as represented by an asymptotic analysis.

Various concepts and criteria have been introduced over the years to characterize fracture behavior. Among the widely accepted criteria is the strain energy release rate "g". "g" is a measure of the crack extension force. Crack opening displacement (c.o.d.) is yet another criterion that has wide experimental application.

More recently, Rice's J-Integral [9] has generated wide applicability of a path independent integral in assessing near crack tip behavior. The J-integral concept can be used to solve non-linear fracture mechanics problems. It can also be used in problems where deformation plasticity assumptions are valid.

Directional considerations for possible crack extension have been investigated by Sih [10]. He postulates a "strain energy density" concept as the controlling quantity. The strain energy

density concept is useful only for linear elastic fracture mechanics. Analytical solutions to inclined cracks have been generated by Pu, Scanlon and Hussain [11] for elastic biface materials.

The finite element method (FEM) has also been very widely used for crack analysis. Analysis of crack tip deformation fields has been obtained by using very small sized elements near the crack tip. This type of analysis is most satisfactory if the very near crack tip region is not of primary interest. However, a clearer understanding of crack tip behavior is important if a non-brittle material is considered. Semi-brittle and ductile materials have considerable regions of plasticity ahead of the crack tip. In the study of real materials it is, therefore, necessary to investigate, very accurately, what happens near the crack tip.

A crack tip, essentially, presents a singularity. Therefore, decreasing the element size at the crack tip becomes a hopeless process. Linear elastic fracture mechanics predicts a $\frac{1}{r^{1/2}}$ type singularity as $r \to 0$.

In the stiffness method of analysis, displacement functions are assumed for the discretized elements. Then the finite element method is carried out by a minimization of the total potential energy. In the usual FEM, the displacement function assumed for all the elements in the field is the same. Since a crack presents a singularity problem, it suggests the use of special crack tip finite elements which embed the inverse root singularity.

Chan, Tuba, and Wilson [12] have discussed extrapolation methods of determining stress intensity factors (K) from constant strain triangles. Chan et. al. have reported an agreement within 4 to 5% of known solutions for K, when approximately 2000 degrees of freedom were used.

Hayes [13] determined K from a calculation of the decrease in potential energy of a body due to an increase in crack length, with applied loads and displacement constraints remaining fixed. He obtained an accuracy of about 5% when 1000 degrees of freedom were allowed.

For crack extensional analysis, Rice's J-integral has been very successfully applied by Chan et. al. Kobayashi et. al. [14] have also used the J-integral concept to advantage. The J-integral has a value which is independent of the particular path chosen; there is no restriction that the material be linear elastic, but instead only that its stress-strain relations be consistent with the existence of a strain energy function.

Other methods of solving for K have been discussed by Barone and Robinson [15] and Rice [16]. These methods use elastic reciprocity properties to formulate new boundary value problems whose solution leads to a determination of K, but through calculations which do not require numerical accuracy in the near tip region.

Some current analysis lays emphasis on the embedding of the elastic singular term in the displacement assumption for the near tip finite elements. Wilson (for Mode III) [17] and Hilton and Hutchinson

[6], Byskov [18] and Tracey [19] (for Mode I) have used the embedded Singularity Concept.

In other recent developments, computational accuracy has been improved by using the J-integral and other methods of asymptotic analysis. Among these are the works by Levy et. al. [20], Rice and Tracey [21] and Tracey [22]. An overall review of plane stress fracture analysis has been completed by Verette and Wilhem [23].

Most of the singular element procedures determine elastic stress intensity factors with a range of 1 to 5% accuracy. Experimentally, there have been a number of related investigations such as the photoelastic studies of Kawata [24], Dixion [25], Ault [26], Post [27], Fessler and Mansell [28] and Smith and Smith [29]. Gerberich [30] used a photoelastic technique to study plastic strains and energy density in cracked plates. Hahn and Rosenfield [31] investigated the size of locally yielded regions, the stress distributions and displacements in a Mode I analysis. Underwood, Swedlow and Kendall [32] used a light interference technique to study crack tip strains in edge cracked sheet specimen.

Accounting for plasticity in fracture has brought about various modelling of plastic zones ahead of the crack tip. Noteworthy contributions are those of Barrenblatt-Dugdale [33] and Bilby, Cottrell and Swinden [34].

In an effort to bring the investigation of near-tip nonlinear deformation one step closer to real engineering circumstances, Kahl and Reifsnider [35] considered the influence of local variations of

yield strength on plastic enclave development at crack tips. The shape and size of the plastic zones and the near tip stress distributions were determined, by analysis and experiment, to be significantly altered by such variations. Using a J-integral approach for analysis and a large number of experimental tests, Reifsnider and Kahl later showed that fatigue crack propagation was also influenced by one-dimensional spatial variations in material (yield) strength [36]. The so-called strength gradient effects were shown to be independent of level of strength considerations.

All of the investigations cited above were concerned with situations wherein the crack axis represented an axis of symmetry with respect to the resulting deformation fields. However, it is reasonable to expect that if, as Hutchinson and others have shown, the stress (and strain) distributions near a crack tip in a hardening material are controlled by the dominant nonlinear response, and if the local hardening and strength characteristics of the material vary with position, then the resulting deformation field may not be symmetric around the crack axis. Work will be presented here to determine the extent to which such an expectation is borne out by an analysis and to establish a significance of the result by demonstrating the effect experimentally.

A major forte of fracture mechanics has been, as mentioned earlier, that a fairly sophisticated elasticity analysis can be brought to bear on problems of considerable engineering consequence to yield results which can be characterized by a single simple

concept--the stress intensity factor. At the same time, a major weakness of those (elastic-plastic) analyses which have been developed to handle problems beyond the scope of linear elastic fracture mechanics is that they cannot, in general, be represented or used in a sufficiently simple, versatile, general way so as to put them firmly in the grasp of engineering practitioners.

Most engineering materials develop zones of plastic deformation at the tip of a crack under load. For small-scale yielding, the elastic, singular solutions are usually still adequate representations of the stress and strain distributions at distances of one or two diameters of the plastic zone away from the crack tip, and beyond. However, if the remote stress reaches a value which is at least as great as one half of the net section yield stress in ductile or semi-brittle materials, it is quite likely that the elastic, singular solution is not a good approximation to any part of the stress distribution. More generally, there is a rather large class of problems in which the nature of the stress (or strain) singularity at the crack tip depends on the level of applied load so that any elastic singularity having a fixed functional form is inadequate. An obvious example of the latter is the situation where local material properties vary as a function of position, as would be the case in composite materials.

Considerable attention has been given to the development of finite element techniques in fracture mechanics. In particular, a variety of discrete-element techniques has been developed to handle

problems which are beyond the scope of linear elastic fracture mechanics. These techniques are generally highly sophisticated, however, and application to a particular problem (crack size, specimen geometry, material response characteristics, and prescribed type of loading) usually requires a fair amount of specialized effort. Also, even the simplest subsequent geometry change or change of crack length requires that a new discrete-element grid be established requiring considerable effort. The choice of a grid to analyze a crack problem (or any problem involving a singularity) is, in itself, a tedious procedure and has been the subject of much study. (See, for example, reference [38].) In many instances, the analysis scheme to be presented here, Unimod, can be used to solve these elastic-plastic problems with comparable (in some cases, superior) accuracy. At the same time, changes of specimen geometry, crack size and local material response characteristics can be handled with almost negligible effort, especially in comparison to other numerical methods.

In the present work, a comprehensive study has been carried out to investigate the nature and importance of nonlinear and non-symmetric deformation patterns in fracture, especially in the presence of local material nonuniformities. This study includes a theoretical analysis, an extensive finite element analysis (including the introduction of a new concept-Unimod) and an experimental verification of the non-symmetric effects.

CHAPTER II

A STRESS FUNCTION FORMULATION AND APPROXIMATE SOLUTION OF THE UNSYMMETRIC DEFORMATION PROBLEM FOR CRACKS IN NON-UNIFORM MATERIALS

In this chapter, relative stress and strain distributions are presented for the near-tip deformation field corresponding to a homogeneous cracked plate with spatially variable mechanical properties. Using a nonlinear (strain-hardening) stress-strain relationship and deformation plasticity, a first approximation asymptotic stress function solution is determined which shows that unsymmetric deformation fields develop in homogeneous materials with non-uniform properties. The amplitude of the stress singularity at the tip is shown to be dependent upon the non-uniformity.

2.1 DEVELOPMENT OF CONTROLLING RELATIONSHIP

The constitutive relationship between stress and strain which was used was the Ramberg-Osgood model in nondimensionalized form, i.e.,

$$\varepsilon = \sigma + \alpha\sigma^n \qquad (2\text{-}1)$$

where n is the hardening coefficient of the material.

It was assumed in the analysis that the total deformation theory of plasticity was valid and that the Mises yield condition was appropriate.

The yield strength was being allowed to vary in the vicinity of the crack tip, and was assumed to be a function of the coordinates times an amplitude factor y_o.

The stress function, to be determined, was nondimensionalized with respect to y_o.

The generalized stress-strain relation for simple tension was written as:

$$\varepsilon_{ij} = (1+\nu)\, s_{ij} + \frac{1-2\nu}{3}\, \sigma_{pp}\, \delta_{ij} + \frac{3}{2}\, \alpha \sigma_e^{n-1}\, s_{ij} \qquad (2\text{-}2)$$

where s_{ij} is the stress deviator and σ_e is the effective stress.

The following equations were used for the generalized plane stress case.

Stress function relations:

$$\left.\begin{aligned} \sigma_r &= \frac{1}{r}\frac{\partial \phi}{\partial r} + \frac{1}{r^2}\frac{\partial^2 \phi}{\partial \theta^2} \\ \sigma_\theta &= \frac{\partial^2 \phi}{\partial r^2} \\ \sigma_{r\theta} &= -\frac{\partial}{\partial r}\left(\frac{1}{r}\frac{\partial \phi}{\partial \theta}\right) \end{aligned}\right\} \qquad (2\text{-}3)$$

Effective stress:

$$\sigma_e^2 = \sigma_r^2 + \sigma_\theta^2 - \sigma_r \sigma_\theta + 3\sigma_{r\theta}^2 \qquad (2\text{-}4)$$

Stress-strain relations:

$$\left.\begin{aligned} \varepsilon_r &= \sigma_r - \nu\sigma_\theta + \alpha\,\sigma_e^{n-1}\left(\sigma_r - \tfrac{1}{2}\sigma_\theta\right) \\ \varepsilon_\theta &= \sigma_\theta - \nu\sigma_r + \alpha\,\sigma_e^{n-1}\left(\sigma_\theta - \tfrac{1}{2}\sigma_r\right) \\ \varepsilon_{r\theta} &= (1+\nu)\,\sigma_{r\theta} + \tfrac{3}{2}\,\alpha\,\sigma_e^{n-1}\,\sigma_{r\theta} \end{aligned}\right\} \qquad (2\text{-}5)$$

Compatibility equation:

$$\frac{1}{r}\frac{\partial^2}{\partial r^2}(r\,\varepsilon_\theta) + \frac{1}{r^2}\frac{\partial^2\varepsilon_r}{\partial\theta^2} - \frac{1}{r}\frac{\partial\varepsilon_r}{\partial r} - \frac{2}{r^2}\frac{\partial}{\partial r}\left(\frac{\partial}{\partial\theta}\,\varepsilon_{r\theta}\cdot r\right) = 0. \qquad (2\text{-}6)$$

Substituting the stress function relations (2-3) into equations (2-5) and subsequently into (2-6), the compatibility equation reduces to:

$$\frac{1}{r}\frac{\partial^2}{\partial r^2}\left\{r\left[\frac{\partial^2\phi}{\partial r^2} - \nu\left(\frac{\partial\phi}{\partial r} + \frac{1}{r^2}\frac{\partial^2\phi}{\partial\theta^2}\right)\right]\right\} + \frac{1}{r}\frac{\partial^2}{\partial r^2}\left\{r\,\alpha\,\sigma_e^{n-1}\left[\frac{\partial^2\phi}{\partial r^2} - \frac{1}{2}\left(\frac{1}{r}\frac{\partial\phi}{\partial r}\right.\right.\right.$$

$$\left.\left.\left. + \frac{1}{r^2}\frac{\partial^2\phi}{\partial\theta^2}\right)\right]\right\} + \frac{1}{r^2}\frac{\partial^2}{\partial\theta^2}\left\{\frac{1}{r}\frac{\partial\phi}{\partial r} + \frac{1}{r^2}\frac{\partial^2\phi}{\partial\theta^2} - \nu\frac{\partial^2\phi}{\partial r^2}\right\} + \frac{1}{r^2}\frac{\partial^2}{\partial\theta^2}\left\{\alpha\,\sigma_e^{n-1}\left[\frac{1}{r}\frac{\partial\phi}{\partial r}\right.\right.$$

$$\left.\left. + \frac{1}{r^2}\frac{\partial^2\phi}{\partial\theta^2} - \frac{1}{2}\frac{\partial^2\phi}{\partial r^2}\right]\right\} - \frac{1}{r}\frac{\partial}{\partial r}\left\{\frac{1}{r}\frac{\partial\phi}{\partial r} + \frac{1}{r^2}\frac{\partial^2\phi}{\partial\theta^2} - \nu\frac{\partial^2\phi}{\partial r^2}\right\}$$

$$- \frac{1}{r}\frac{\partial}{\partial r}\left\{\alpha\,\sigma_e^{n-1}\left[\frac{1}{r}\frac{\partial\phi}{\partial r} + \frac{1}{r^2}\frac{\partial^2\phi}{\partial\theta^2} - \frac{1}{2}\frac{\partial^2\phi}{\partial r^2}\right]\right\}$$

$$+ \frac{2}{r^2}\frac{\partial}{\partial r}\left\{\frac{\partial}{\partial\theta}\left[(1+\nu)\,\frac{\partial}{\partial r}\left(\frac{1}{r}\frac{\partial\phi}{\partial\theta}\right)\right]\cdot r\right\}$$

$$+ \frac{3}{r^2} \frac{\partial}{\partial r} \left\{ \frac{\partial}{\partial \theta} \left[\alpha \, \sigma_e^{n-1} \, \frac{\partial}{\partial r} \left(\frac{1}{r} \frac{\partial \phi}{\partial \theta} \right) \right] \cdot r \right\} = 0 \tag{2-7}$$

which further reduces to:

$$\nabla^4 \phi + \frac{1}{r} \frac{\partial^2}{\partial r^2} \left\{ \alpha \, \sigma_e^{n-1} \, \chi_1 \right\} + \frac{1}{r^2} \frac{\partial^2}{\partial \theta^2} \left\{ \alpha \, \sigma_e^{n-1} \, \chi_2 \right\}$$

$$+ \frac{1}{r} \frac{\partial}{\partial r} \left\{ \alpha \, \sigma_e^{n-1} \, \chi_3 \right\} + \frac{3}{r^2} \frac{\partial^2}{\partial r \partial \theta} \left\{ \alpha \, \sigma_e^{n-1} \, \chi_4 \right\} = 0 \tag{2-8}$$

where

$$\left.\begin{aligned} \chi_1 &= r \frac{\partial^2 \phi}{\partial r^2} - \frac{1}{2} \frac{\partial \phi}{\partial r} - \frac{1}{2r} \frac{\partial^2 \phi}{\partial \theta^2} \\ \chi_2 &= \frac{1}{r} \frac{\partial \phi}{\partial r} + \frac{1}{r^2} \frac{\partial^2 \phi}{\partial \theta^2} - \frac{1}{2} \frac{\partial^2 \phi}{\partial r^2} \\ \chi_3 &= - \frac{\partial \phi}{\partial r} - \frac{1}{r^2} \frac{\partial^2 \phi}{\partial \theta^2} + \frac{1}{2} \frac{\partial^2 \phi}{\partial r^2} \\ \chi_4 &= \frac{\partial^2 \phi}{\partial r \partial \theta} - \frac{1}{r} \frac{\partial \phi}{\partial \theta} \end{aligned}\right\} . \tag{2-9}$$

Focusing our attention on a crack tip for a Mode I loading analysis, as $r \to 0$ the stresses become unbounded. Hence, an asymptotic expansion of a solution for (2-8) can be assumed. Then the dominant term in the solution for ϕ can be written as:

$$\phi = K \, r^s \, \bar{\phi}(\theta) \tag{2-10}$$

where K is an amplitude factor.

Substituting (2-10) into equations (2-9), we get

$$\left.\begin{aligned} \chi_1 &= \frac{K}{2}\left[s(2s-3)\bar{\phi} - \bar{\phi}''\right] r^{s-1} \\ \chi_2 &= K\left[\frac{s}{2}(3-s)\bar{\phi} + \bar{\phi}''\right] r^{s-2} \\ \chi_3 &= K\left[\frac{s}{2}(s-3)\bar{\phi} - \bar{\phi}''\right] r^{s-2} \\ \chi_4 &= K\,(s-1)\bar{\phi}'\, r^{s-1} \end{aligned}\right\} \qquad (2\text{-}11)$$

where $\bar{\phi}'$ and $\bar{\phi}''$ indicate $\frac{\partial\bar{\phi}}{\partial\theta}$ and $\frac{\partial^2\bar{\phi}}{\partial\theta^2}$ respectively.

Yield strength variations were introduced by considering α to be spatially variable. Assuming separation of variables, α was written as

$$\alpha = \beta\, r^p\, \bar{\alpha}(\theta) \qquad (2\text{-}12)$$

where β is a constant and p is a yield strength variation characteristic.

Using equations (2-11) and equation (2-12), equation (2-8) becomes:

$$\begin{aligned} &K\left[\nabla^4\bar{\phi}\right] r^{s-4} + K\beta\left[p(p-1)\,\frac{\bar{\alpha}}{2}\,\sigma_e^{\,n-1}\left\{s(2s-3)\bar{\phi} - \bar{\phi}''\right\} + 3p\bar{\alpha}'\,\sigma_e^{\,n-1}\,(s-1)\bar{\phi}'\right. \\ &\quad + 3p\bar{\alpha}\,\frac{\partial\sigma_e^{\,n-1}}{\partial\theta}\,(s-1)\bar{\phi}' + 3p\bar{\alpha}\,\sigma_e^{\,n-1}\,(s-1)\bar{\phi}'' \\ &\quad + \bar{\alpha}''\,\sigma_e^{\,n-1}\left\{\frac{s}{2}(3-s)\bar{\phi} + \bar{\phi}''\right\} + \sigma_e^{\,n-1}\,p\bar{\alpha}(s-1)\left\{s(2s-3)\bar{\phi} + \bar{\phi}''\right\} \\ &\quad + 2p\bar{\alpha}'\,\frac{\partial\sigma_e^{\,n-1}}{\partial\theta}\left\{\frac{s}{2}(3-s)\bar{\phi} + \bar{\phi}''\right\} + 2p\bar{\alpha}'\,\sigma_e^{\,n-1}\left\{\frac{s}{2}(3-s)\bar{\phi}' + \bar{\phi}'''\right\} \\ &\quad \left. + p\bar{\alpha}\,\sigma_e^{\,n-1}\left\{s(2s-3)\bar{\phi} - \bar{\phi}''\right\} + 3\bar{\alpha}'\,\sigma_e^{\,n-1}\,(s-1)^2\bar{\phi}\right. \end{aligned}$$

$$+ \bar{\alpha}\,\sigma_e^{n-1}\,(s-1)(s-2)\left\{s(2s-3)\bar{\phi} - \bar{\phi}''\right\} + \bar{\alpha}\,\frac{\partial^2\sigma_e^{n-1}}{\partial\theta^2}\left\{\frac{s}{2}(3-s)\bar{\phi} + \bar{\phi}''\right\}$$

$$+ 2\bar{\alpha}\,\frac{\partial\sigma_e^{n-1}}{\partial\theta}\left\{\frac{s}{2}(3-s)\bar{\phi}' + \bar{\phi}'''\right\} + \bar{\alpha}\,\sigma_e^{n-1}\left\{\frac{s}{2}(3-s)\bar{\phi}'' + \bar{\phi}^{iv}\right\}$$

$$+ \bar{\alpha}\,\sigma_e^{n-1}\left\{\frac{s}{2}(s-3)\phi - \phi''\right\}(s-2) + 3\bar{\alpha}\,\frac{\partial\sigma_e^{n-1}}{\partial\theta}\,(s-1)^2\bar{\phi}'$$

$$+ 3\bar{\alpha}\,\sigma_e^{n-1}\,(s-1)^2\bar{\phi}''\Big]\,r^{s+p-4} + K\beta\left[p\bar{\alpha}\,\frac{\partial\sigma_e^{n-1}}{\partial r}\left\{s(2s-3)\bar{\phi} - \bar{\phi}''\right\}\right.$$

$$+ 3\bar{\alpha}'\,\frac{\partial\sigma_e^{n-1}}{\partial r}\,(s-1)\bar{\phi}' + \bar{\alpha}\,\frac{\partial\sigma_e^{n-1}}{\partial r}\left\{s(2s-3)\bar{\phi} - \bar{\phi}''\right\}(s-1)$$

$$+ \bar{\alpha}\,\frac{\partial\sigma_e^{n-1}}{\partial r}\left\{\frac{s}{2}(s-3)\bar{\phi} - \bar{\phi}''\right\} + 3\bar{\alpha}\,\frac{\partial^2\sigma_e^{n-1}}{\partial r\partial\theta}\,(s-1)\bar{\phi}'$$

$$\left.+ 3\bar{\alpha}\,\frac{\partial\sigma_e^{n-1}}{\partial r}\,(s-1)\bar{\phi}''\right]\,r^{s+p-3}$$

$$+ K\beta\left[\frac{\bar{\alpha}}{2}\,\frac{\partial^2\sigma_e^{n-1}}{\partial r^2}\left\{s(2s-3)\bar{\phi} - \bar{\phi}''\right\}\right]\,r^{s+p-2} = 0 \qquad (2\text{-}13)$$

where $(\,)'$ and $(\,)''$ indicate differentiation with respect to θ.

Using equation (2-10) and equation (2-4), we can write

$$\sigma_e^{n-1} = K^{(s-2)(n-1)}\,r^{(s-2)(n-1)}\,\bar{\sigma}_e^{n-1}(\theta) \qquad (2\text{-}14)$$

where $\bar{\sigma}_e^{n-1}(\theta)$ is a nonlinear function of ϕ, ϕ' and ϕ''.

Substituting equation (2-14) into equation (2-13), the following equation is obtained:

$$K\,[\nabla^4\bar{\phi}]\,r^{s-4}$$

$$+ K^{(s-2)(n-1)+1}\beta\left[\left\{p(p-1)\,\frac{\bar{\alpha}}{2}\left\{s(2s-3)\bar{\phi} - \bar{\phi}''\right\} + 3p\bar{\alpha}'\,(s-1)\bar{\phi}'\right.\right.$$

$$+ 3p\bar{\alpha}\,(s-1)\bar{\phi}'' + \bar{\alpha}''\left\{\frac{s}{2}(3-s)\bar{\phi} + \bar{\phi}''\right\} + p\bar{\alpha}\,(s-1)\left\{s(2s-3)\bar{\phi} - \bar{\phi}''\right\}$$

$$+ 2\alpha'\left\{\frac{s}{2}(3-s)\phi' + \phi'''\right\} + p\bar{\alpha}\left\{s(2s-3)\bar{\phi} - \bar{\phi}''\right\}$$

$$+ 3\bar{\alpha}\,(s-1)^2\bar{\phi} + \bar{\alpha}\,(s-1)(s-2)\left\{s(2s-3)\bar{\phi} - \bar{\phi}''\right\} + \bar{\alpha}\left\{\frac{s}{2}(3-s)\bar{\phi}'' + \bar{\phi}^{iv}\right\}$$

$$+ \bar{\alpha}\left\{\frac{s}{2}(s-3)\phi - \phi''\right\}(s-2) + 3\bar{\alpha}\,(s-1)^2\bar{\phi}'' + p\bar{\alpha}\,(s-2)(n-1)\left\{s(2s-3)\bar{\phi}\right.$$

$$\left. - \bar{\phi}''\right\} + 3\bar{\alpha}'\,(s-2)(n-1)(s-1)\bar{\phi}' + \bar{\alpha}\,(s-2)(n-1)\left\{s(2s-3)\bar{\phi} - \bar{\phi}''\right\}(s-1)$$

$$+ \bar{\alpha}\,(s-2)(n-1)\left\{\frac{s}{2}(s-3)\bar{\phi} - \bar{\phi}''\right\} + 3\bar{\alpha}\,(s-2)(n-1)(s-1)\bar{\phi}''$$

$$+ \frac{\bar{\alpha}}{2}(s-2)(n-1)\left\{(s-2)(n-1)-1\right\}\left\{s(2s-3)\bar{\phi} - \bar{\phi}''\right\}\Bigg\}\,\bar{\sigma}_e^{\,n-1}$$

$$+ \left\{3p\bar{\alpha}\,(s-1)\bar{\phi}' + 2p\bar{\alpha}'\left\{\frac{s}{2}(3-s)\bar{\phi} + \bar{\phi}''\right\} + 2\bar{\alpha}\left\{\frac{s}{2}(3-s)\bar{\phi}' + \bar{\phi}'''\right\}\right.$$

$$\left. + 3\alpha\,(s-1)^2\bar{\phi}' + 3\alpha\,(s-2)(n-1)(s-1)\bar{\phi}'\right\}\frac{\partial\sigma_e^{\,n-1}}{\partial\theta}$$

$$\left. + \left\{\bar{\alpha}\,\frac{s}{2}(3-s)\bar{\phi} + \bar{\phi}''\right\}\right\}\frac{\partial^2\sigma_e^{\,n-1}}{\partial\theta^2}\Bigg]\, r^{n(s-2)+p-2} = 0\,. \qquad (2\text{-}15)$$

In order that the elastic part of the equation be consistent with existing solutions for ϕ, we require that $s < 2$ and

$$p < \frac{n-1}{2}\,. \qquad (2\text{-}16)$$

Under these conditions, the nonlinear terms are dominant. Considering the case of large n values; that is, approaching a perfectly plastic state, the "effective stress" may be considered to be nearly constant.

Hence, as an approximation, $\frac{\partial \bar{\sigma}_e^{n-1}}{\partial \theta}$ and $\frac{\partial^2 \bar{\sigma}_e^{n-1}}{\partial \theta^2}$ were taken to be small, relative to $\bar{\sigma}_e^{n-1}$ and the corresponding terms are neglected for a first approximation in equation (2-15).

After eliminating the elastic part, equation (2-15) simplifies to a fourth order differential equation, namely,

$$K^{(s-2)(n-1)+1} \beta \bar{\sigma}_e^{n-1} \left[\bar{\phi}^{iv} + y_1 \bar{\phi}''' + y_2 \bar{\phi}'' + y_3 \bar{\phi}' + y_4 \right] = 0 \quad (2\text{-}17)$$

where

$$y_1 = 2 \frac{\bar{\alpha}'}{\bar{\alpha}}$$

$$y_2 = -\frac{p}{2}(p-1) + 3p(s-1) + \frac{\bar{\alpha}''}{\bar{\alpha}} - p(s-1) - p - (s-1)(s-2)$$
$$+ \frac{s}{2}(3-s) - (s-2) + 3(s-1)^2 - p(s-2)(n-1) - (s-2)(n-1)(s-1)$$
$$- (s-2)(n-1) + 3(s-2)(n-1)(s-1) - \frac{1}{2}(s-2)(n-1)\left\{(s-2)(n-1)-1\right\}$$

$$y_3 = \frac{\bar{\alpha}'}{\bar{\alpha}} [3p(s-1) + s(3-s) + 3(s-2)(n-1)(s-1)]$$

and

$$y_4 = p(p-1)\frac{s}{2}(2s-3) + \frac{s}{2}(3-s)\frac{\bar{\alpha}''}{\bar{\alpha}} + p(s-1)(s)(2s-3)$$
$$+ ps(2s-3) + 3(s-1)^2 \frac{\bar{\alpha}'}{\bar{\alpha}} + (s-1)(s-2)s(2s-3) + \frac{s}{2}(s-3)$$
$$+ p(s-2)(n-1)s(2s-3) + (s-2)(n-1)s(2s-3)(s-1)$$
$$+ (s-2)(n-1)\frac{s}{2}(s-3) + \frac{1}{2}(s-2)(n-1)\left\{(s-2)(n-1)-1\right\} s(2s-3).$$

Equation (2-17) is a fourth-order differential equation with variable coefficients and the solution depends on the values taken by s, n and p.

A lower limit on the value of p can be obtained using a J-integral formulation.

$$J = \int_{\Gamma} (wdy - \sigma_{ij} n_j u_{i,x} ds). \tag{2-18}$$

Assume a path Γ around a crack tip as shown below.

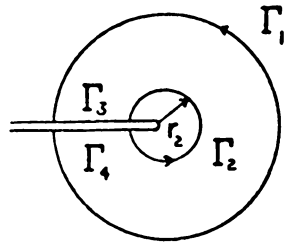

where $\Gamma = \Gamma_1 - \Gamma_2 + \Gamma_3 + \Gamma_4$.

The path of Γ_2 lies in the dominant singularity region, while Γ_1 encloses the elastic far field region.

The J integral vanishes along the free crack surface, i.e., along Γ_3 and Γ_4.

Along Γ_1 in dimensionless terms for Mode I type loading

$$J_{\Gamma_1} = \pi \sigma^{\infty 2} \tag{2-19}$$

$J_{\Gamma} = 0$ i.e., around a closed path.

Therefore,

$$J_{\Gamma_1} = J_{\Gamma_2} . \tag{2-20}$$

In the region of dominant singularity

$$J_{\Gamma_2} = \beta K^{n+1} r_2^{(n+1)(s-2)+1+p} \cdot I_1 , \tag{2-21}$$

where

$$I_1 = \int_{-\pi}^{\pi} \left\{ \frac{n}{n+1} \bar{\bar{\alpha}}\, \bar{\bar{\sigma}}_e^{n+1} \cos\theta - \left[\sin\theta \left\{ (\bar{\sigma}_r(\bar{u}_\theta - \bar{u}_r') \right. \right. \right.$$

$$\left. \left. \left. - \bar{\sigma}_{r\theta}\,(\bar{u}_r + \bar{u}_\theta') \right\} + \left\{ n(s-2)+1 \right\} (\bar{\sigma}_r \bar{u}_r + \bar{\sigma}_{r\theta}\bar{u}_\theta) \cos\theta \left[\bar{\alpha} \right\} \right] d\theta. \quad (2\text{-}22)$$

Rewriting Equation (2-20), we obtain

$$\pi\sigma^{\infty 2} = \beta K^{n+1} r_2^{(n+1)(s-2)+1+p} \cdot I_1 , \quad (2\text{-}23)$$

where r_2 is a radius in the dominant singularity region ($r_2 \to 0$).

Equation (2-23) is valid if

$$(n+1)(s-2)+1+p = 0$$

i.e.,
$$s = \frac{2n+1-p}{n+1} . \quad (2\text{-}24)$$

Therefore, the amplitude factor, K, obtained from Equation (2-23) is

$$K = \left(\frac{1}{\beta}\right)^{\frac{1}{n+1}} \left(\frac{\pi}{I_1}\right)^{\frac{1}{n+1}} \left(\sigma^{\infty}\right)^{\frac{2}{n+1}} . \quad (2\text{-}25)$$

From Equation (2-24), we find

$$p > -1 . \quad (2\text{-}26)$$

The stress expressions will then have the form:

$$\sigma_{ip} = K \frac{1}{r^{\frac{p+1}{n+1}}} f_{ij}\,(\bar{\Phi}(\theta)) \quad (2\text{-}27)$$

where f_{ij} $(\bar{\Phi}(\theta))$ is determined by the strain-displacement relations and $\bar{\Phi}(\theta)$.

2.2 SOLUTIONS TO THE FOURTH-ORDER DIFFERENTIAL EQUATION

Two cases were considered. First, $\bar{\alpha}(\theta)$ was taken to be a constant and second, $\bar{\alpha}(\theta)$ was given a functional form.

Case 1. $\bar{\alpha}(\theta)$ = constant

When $\bar{\alpha}$ = constant, $\frac{\bar{\alpha}'}{\bar{\alpha}}$ and $\frac{\bar{\alpha}''}{\bar{\alpha}}$ are zero. Equation (2-17) reduces to

$$\bar{\phi}^{iv} + y_2\,\bar{\phi}'' + y_4 = 0 \ . \tag{2-28}$$

In this case, the strength variation is represented only by p. Conditions of symmetry exist. An exact solution of (2-21) is possible. The boundary conditions used were:

$$1)\ \bar{\phi}(\pm\pi) = 0 \qquad 2)\ \bar{\phi}'(\pm\pi) = 0 \qquad 3)\ \bar{\phi}'(0) = 0 \ .$$

The elastic stress function for a cracked tensile plate is given by

$$\phi_{el} = k_1\, r^{3/2}\,(\cos\theta/2 + 1/3\cos 3\theta/2) \tag{2-29}$$

From the singularity analysis with p = 0 in equations (2-12)

$$\phi_s = k_2\, r^s\, \bar{\phi}_s\,(\theta)$$
$$s = \frac{2n+1}{n+1} \tag{2-30}$$

where k_1 and k_2 are amplitude factors. In this brief discussion ϕ_{el} is to mean $\phi_{(elastic)}$ as opposed to ϕ_s, i.e., $\phi_{(singular)}$. Solutions obtained for $\bar{\phi}_s$ (θ) are of the form

$$\bar{\phi}_s\ (\theta) = A[\cos r_1\ \theta + b_1 \sin r_1\ \theta + b_2\ e^{r_2\theta} + b_3\ e^{-r_2\theta}] \qquad (2\text{-}31)$$

where, A is an unknown constant, r_1, r_2, b_1, b_2 and b_3 are constants depending on n.

The interface between the region where ϕ_s is dominant and the region where ϕ_{el} is dominant was obtained from

$$\phi_{el} = \phi_s \qquad (2\text{-}32)$$

$$\text{i.e., } k_1\ r^{3/2}\ (\cos \theta/2 + 1/3 \cos 3\theta/2) = k_2\ A\ r^s\ [\cos r_1\ \theta + b_1 \sin r_1\ \theta + b_2\ e^{r_2\theta} + b_3\ e^{-r_2\theta}] \qquad (2\text{-}33)$$

The shape of the boundary was then found to be

$$r = k \left\{ \frac{(\cos r_1\ \theta + b_1 \sin r_1\ \theta + b_2\ e^{r_2\theta} + b_3\ e^{-r_2\theta})}{(\cos \theta/2 + 1/3 \cos 3\theta/2)} \right\}^{s-3/2} \qquad (2\text{-}34)$$

where

$$k = \left(\frac{k_2 A}{k_1} \right)^{s-3/2} \qquad (2\text{-}35)$$

The resulting plot of equation (2-34) is shown in Figure 2-1, for different values of n. It is interesting to note that the shape of the boundary resembles a cardioid. In Figure 2-1, it is seen that with increasing n, the greater the region covered by the singular solution. A very similar boundary shape exists for the elasto-plastic

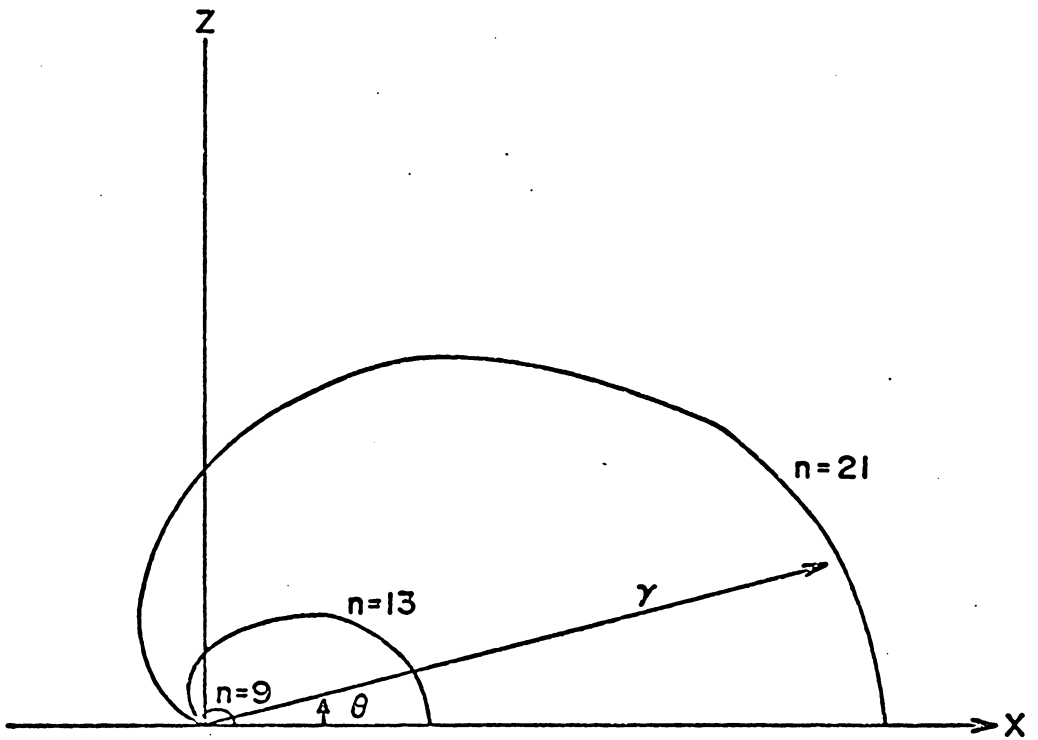

Figure 2-1 Elastic - Singular Boundaries

boundary for an antiplane deformation of a perfectly plastic material [38]. The maximum vertical extension of the boundary occurred at about the 45 degree angle.

Case 2. $\bar{\alpha}(\theta) = a \cos\theta + b \sin\theta + |a| + |b|$

Where a and b were chosen constants, these constants reflect the angle or slope of the strength variation. Here it is not possible to obtain constant coefficients for equation (2-17). Hence, the solution becomes more complex.

However, with further approximations, it is possible to study approximate nature of $\bar{\phi}(\theta)$ behavior. Expanding $\bar{\alpha}$, $\bar{\alpha}'$ and $\bar{\alpha}''$ in a Maclaurin Series, we can write

$$\left.\begin{aligned} \frac{\bar{\alpha}'}{\bar{\alpha}} &= \frac{b}{a+|a|+|b|} \\ \text{and} \\ \frac{\bar{\alpha}''}{\bar{\alpha}} &= \frac{a}{a+|a|+|b|} \end{aligned}\right\} \qquad (2\text{-}36)$$

Because of the nature of the nonsymmetric equation obtained in this case, it was necessary to consider separate solutions for regions i) 0 to π and ii) 0 to $-\pi$.

The boundary conditions used were

$$\left.\begin{array}{ll} \text{i)} & \text{a) } \bar{\phi}(\pi) = 0 \\ & \text{b) } \bar{\phi}'(\pi) = 0 \\ & \text{c) } \bar{\phi}'(0) = 0 \\ \text{ii)} & \text{a) } \bar{\phi}(-\pi) = 0 \\ & \text{b) } \bar{\phi}'(-\pi) = 0 \\ & \text{c) } \bar{\phi}'(0) = 0 \end{array}\right\} \qquad (2\text{-}37)$$

It should be noted that one of the constants in the solution was absorbed into the amplitude factor of ϕ; as a result, quantitative evaluations cannot be made between the two regions mentioned above.

2.3 RESULTS

The approximate solutions described earlier are only valid for large n values. Therefore, n = 21 was chosen for the development of the data.

Figures 2-2, 2-3, and 2-4 represent the distributions obtained when $\bar{\alpha}$ is constant. In this case, the problem is symmetric around the crack axis and the strength variations occur along radial directions for p nonvanishing. Positive values of p correspond to a material which becomes softer in radial directions--a so-called decreasing gradient, and negative p values correspond to soft-to-hard radial distributions of strength, or "positive strength gradients". As explained earlier, the manner in which the boundary conditions are applied makes the ordinates of all curves arbitrary. The abscissa for all figures will be in degrees of angle, plus or minus, as measured from the crack axis.

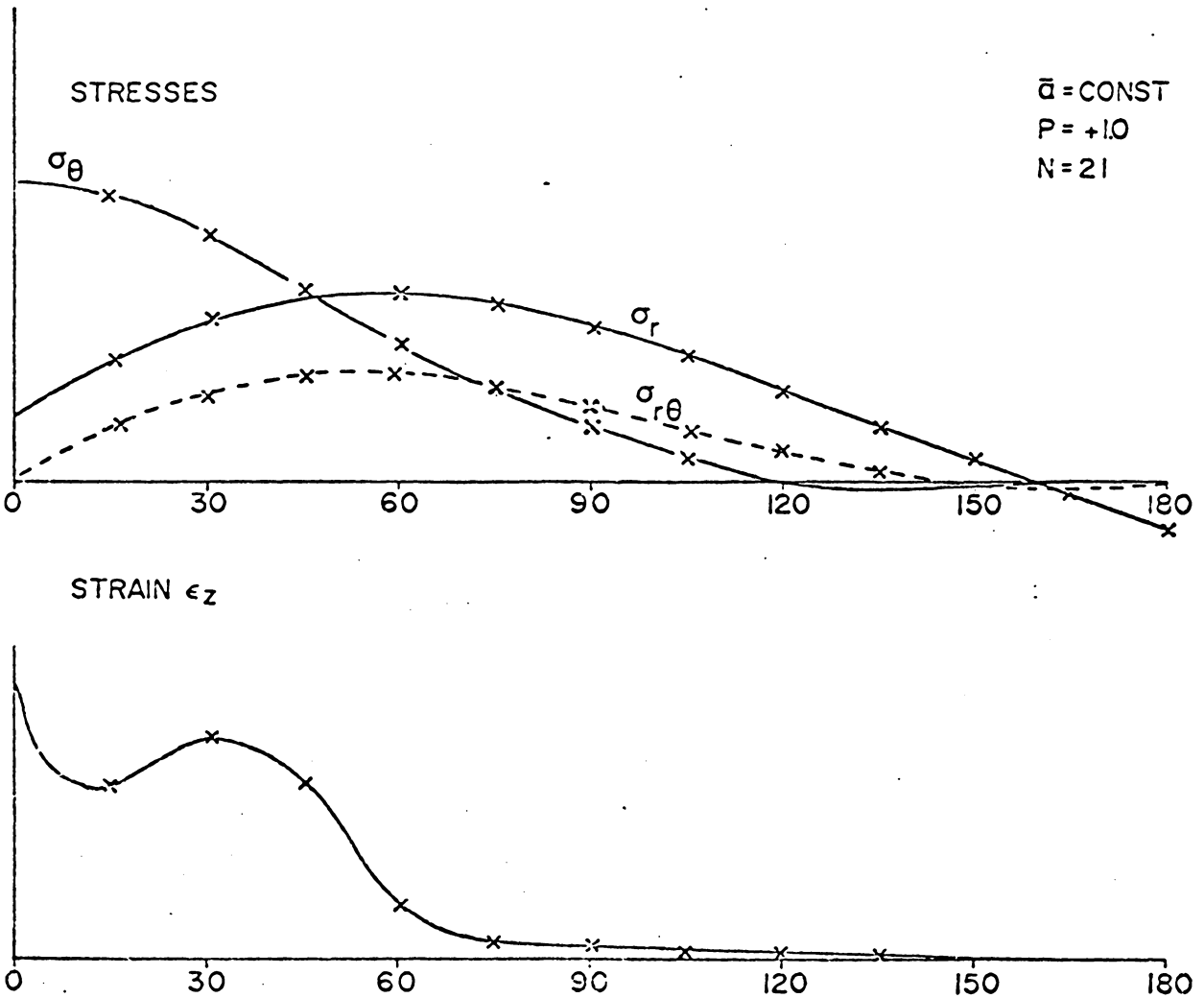

Figure 2-2 Angular variation of stresses and strain (ϵ_z) at a crack tip for $\bar{\alpha}$ = constant and decreasing gradient.

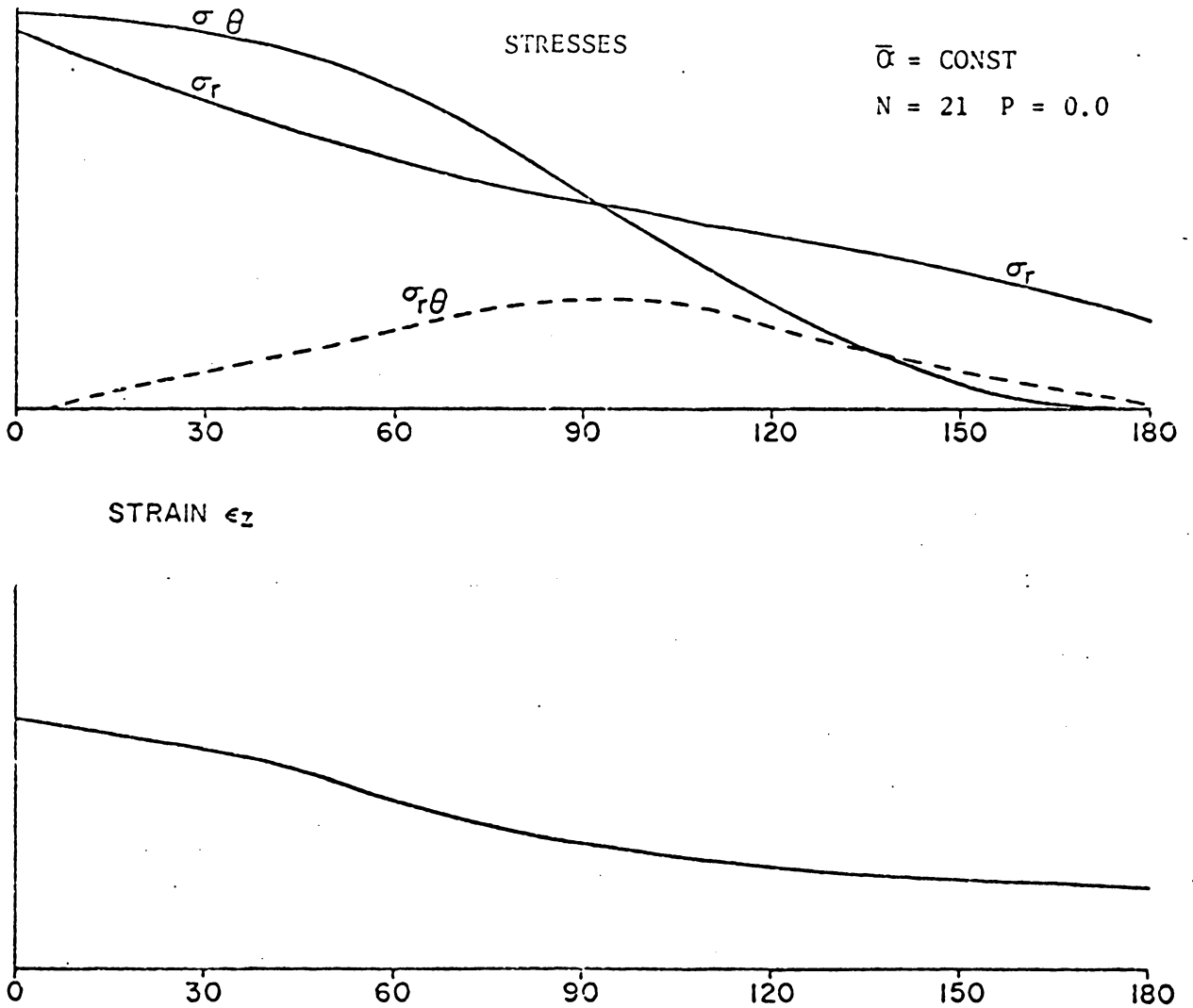

Figure 2-3 Angular variation of stresses and strain (ϵ_z) at a crack tip for uniform material.

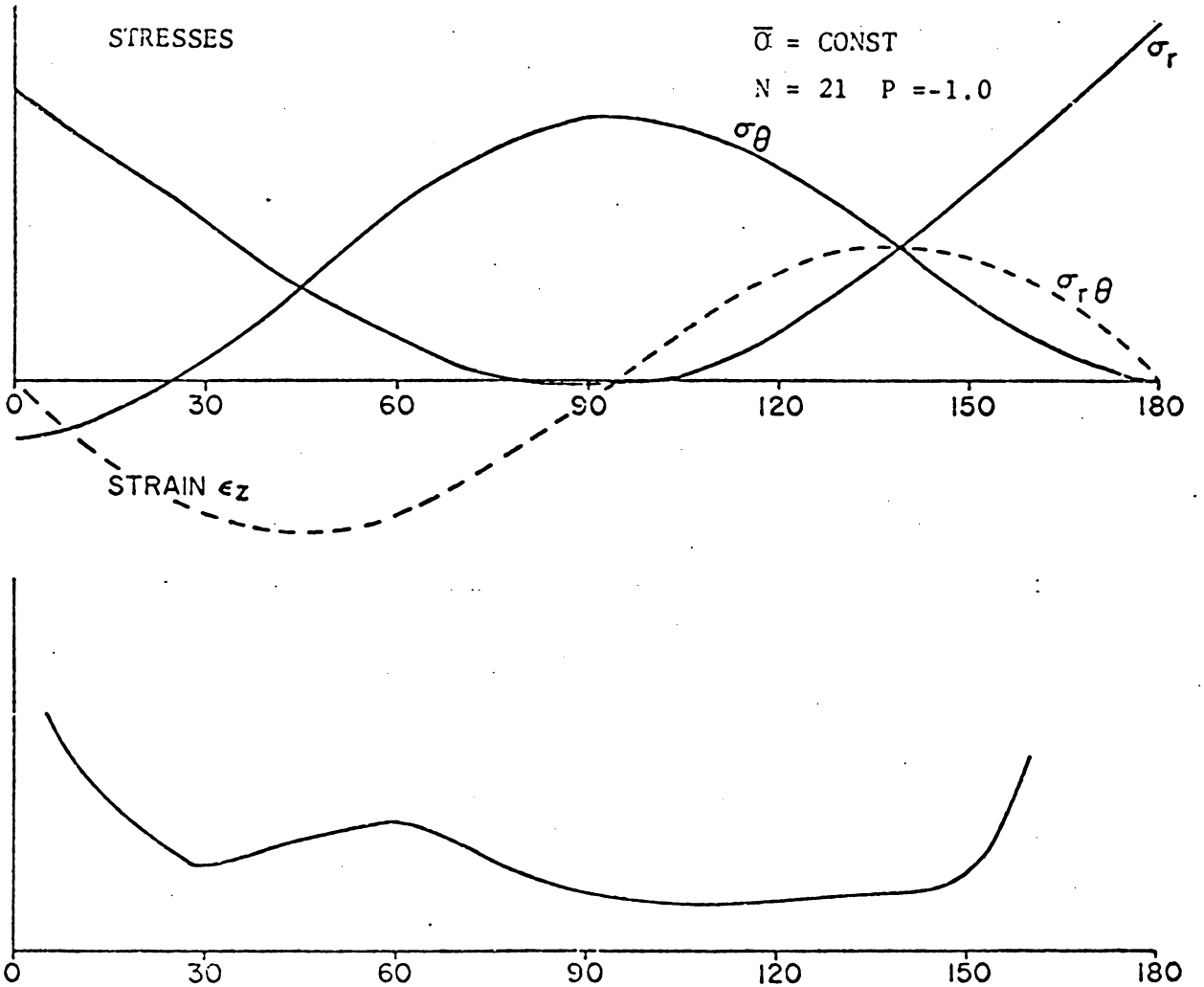

Figure 2-4 Angular variation of stresses and strain (ϵ_z) at a crack tip for $\bar{\alpha}$ = constant and increasing gradient.

The strain, ε_z, sometimes called the total strain, is the algebraic sum of the two principal in-plane strains. Ordinate values above the abscissa are positive and those below are negative as usual.

In Figures 2-5, 2-6, and 2-7 data is presented for the unsymmetric case created by an increasing gradient in the -45° direction. The coefficients of $\bar{\alpha}$ (where $\bar{\alpha} = a \cos\theta + b \sin\theta + |a| + |b|$), i.e., a and b, are so chosen so as to minimize $\bar{\alpha}$ in the +135° direction. In Figure 2-5, only $\bar{\alpha}$ causes the gradient since p = 0. The fact that the magnitudes of the stresses and ε_z show a jump across $\theta = 0°$ is a result of the undetermined constant in our approximate solution as mentioned earlier. Interpretations of the data are best made by allowing for magnitude differences on the plus and minus angle sides in proportion to the jump at $\theta = 0°$.

The data for a decreasing gradient with principal direction at -45° is shown in Figures 2-8 and 2-9. Figure 2-8 has a small gradient slope (p=1) while Figure 2-9 represents the steep gradient case. It can be seen that these negative gradient data are not reflections of the positive gradient data, but represent a discrete case.

Figures 2-10, 2-11, and 2-12 represent gradients with -60° as a principal direction. The increasing gradient data appears in Figure 2-10 for a zero-slope case. Slopes of 1 and 9 are shown for decreasing gradient cases in Figures 2-11 and 2-12.

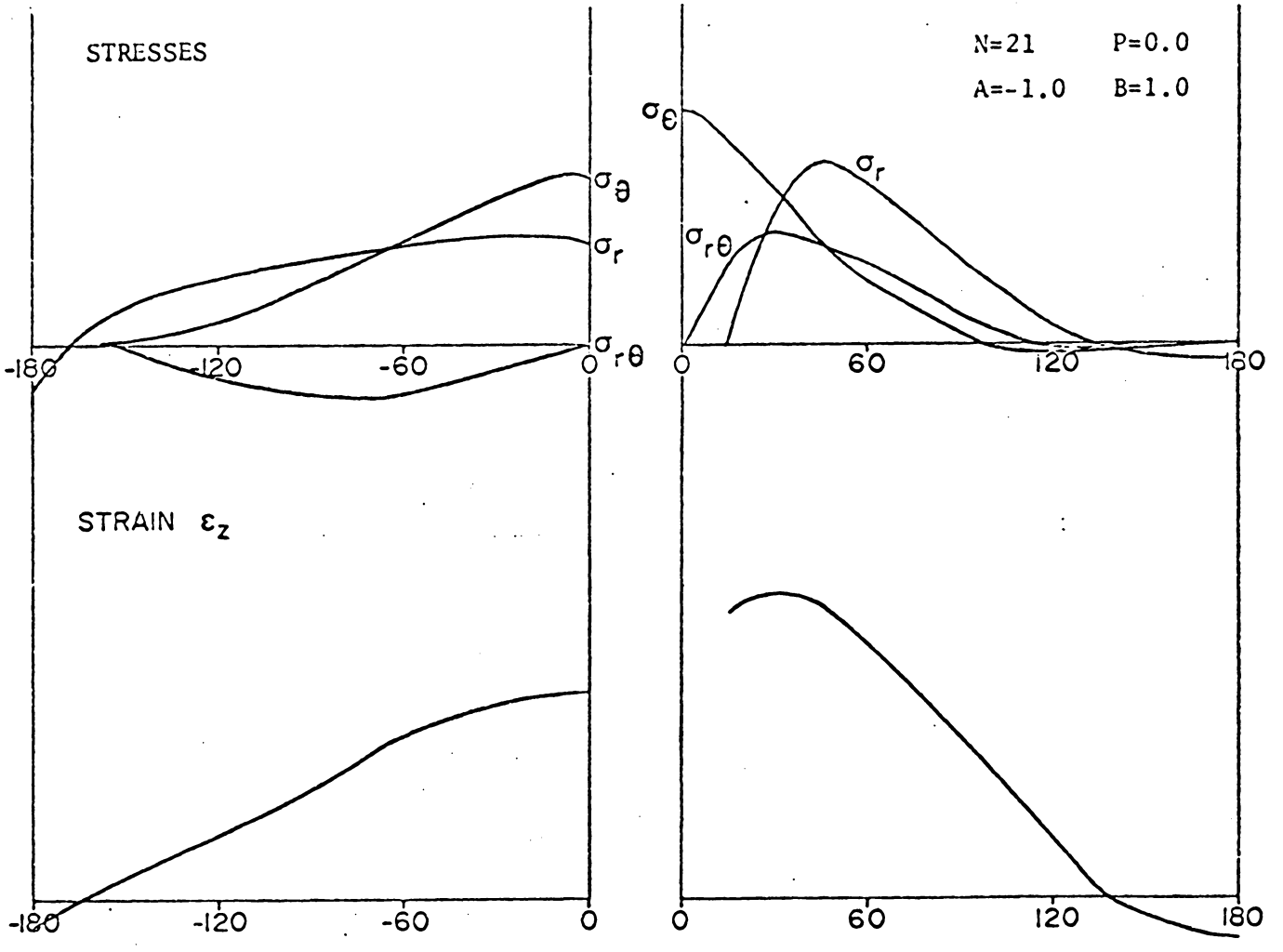

Figure 2-5 Angular variation of stresses and strain (ε_z) at a crack tip for -45° increasing gradient with p = 0.

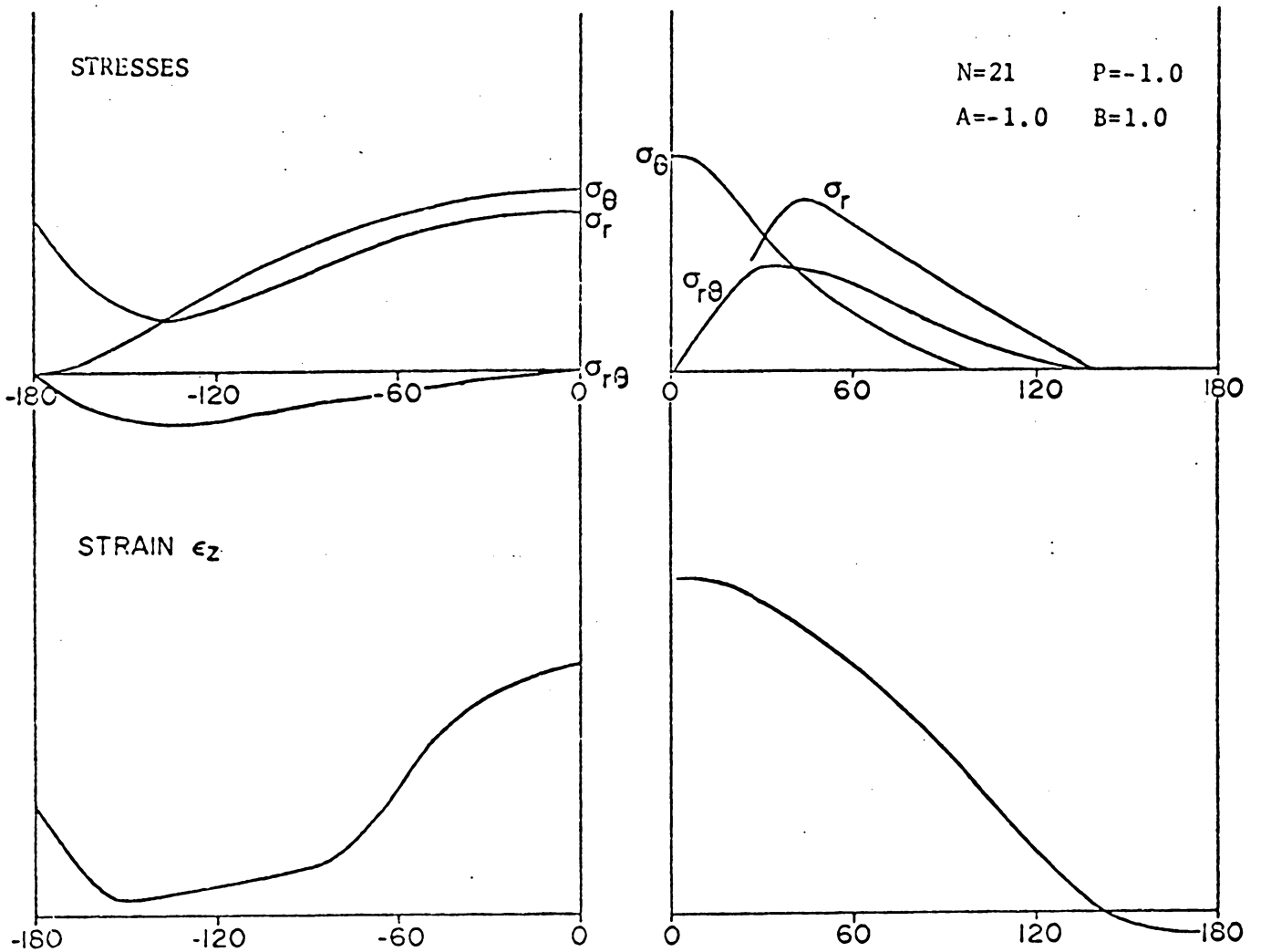

Figure 4-6 Angular variation of stresses and strain (ϵ_z) at a crack tip for -45° increasing gradient with p = -1.0.

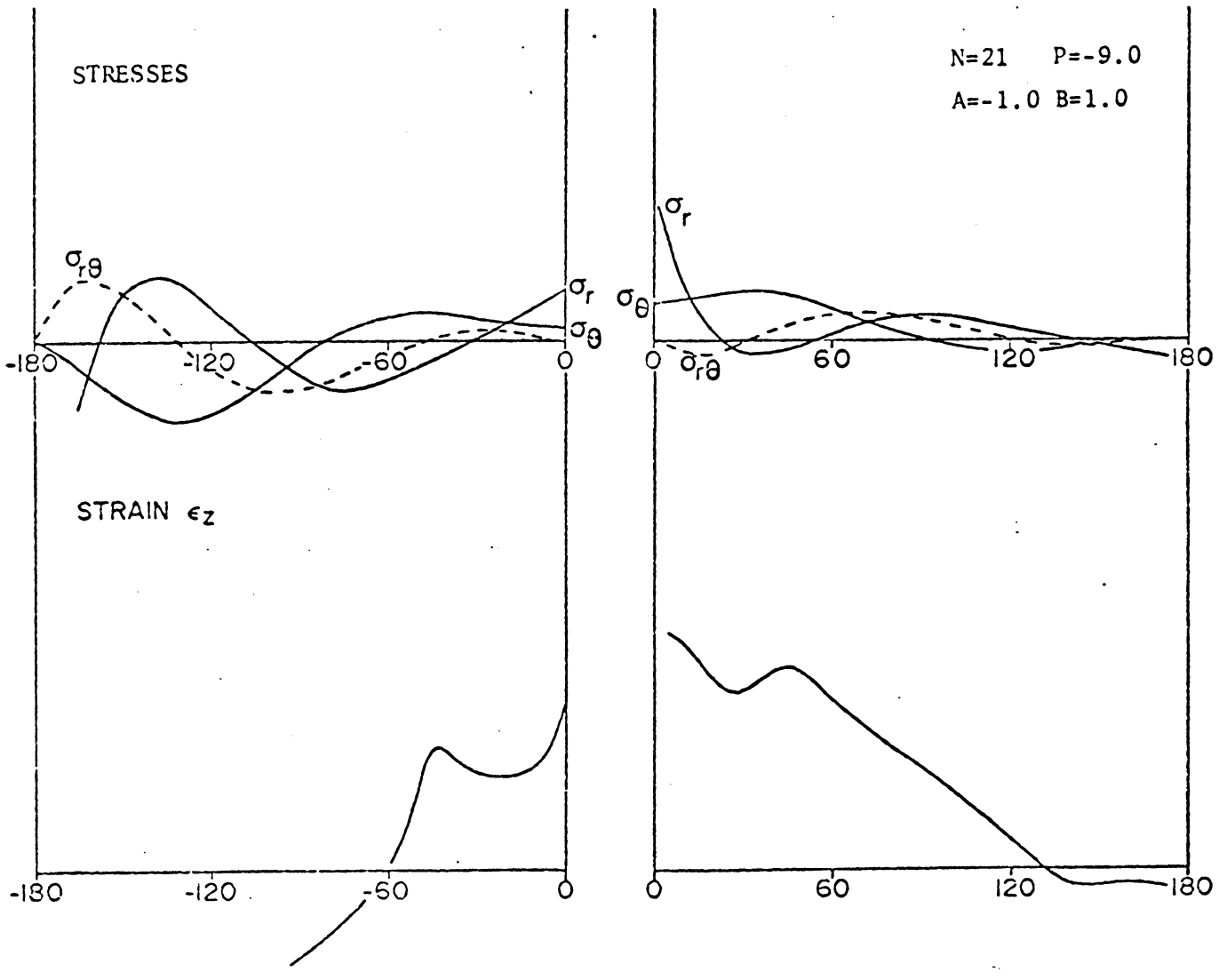

Figure 2-7 Angular viaration of stresses and strain (ϵ_z) at a crack tip for -45° increasing gradient with p = -9.0.

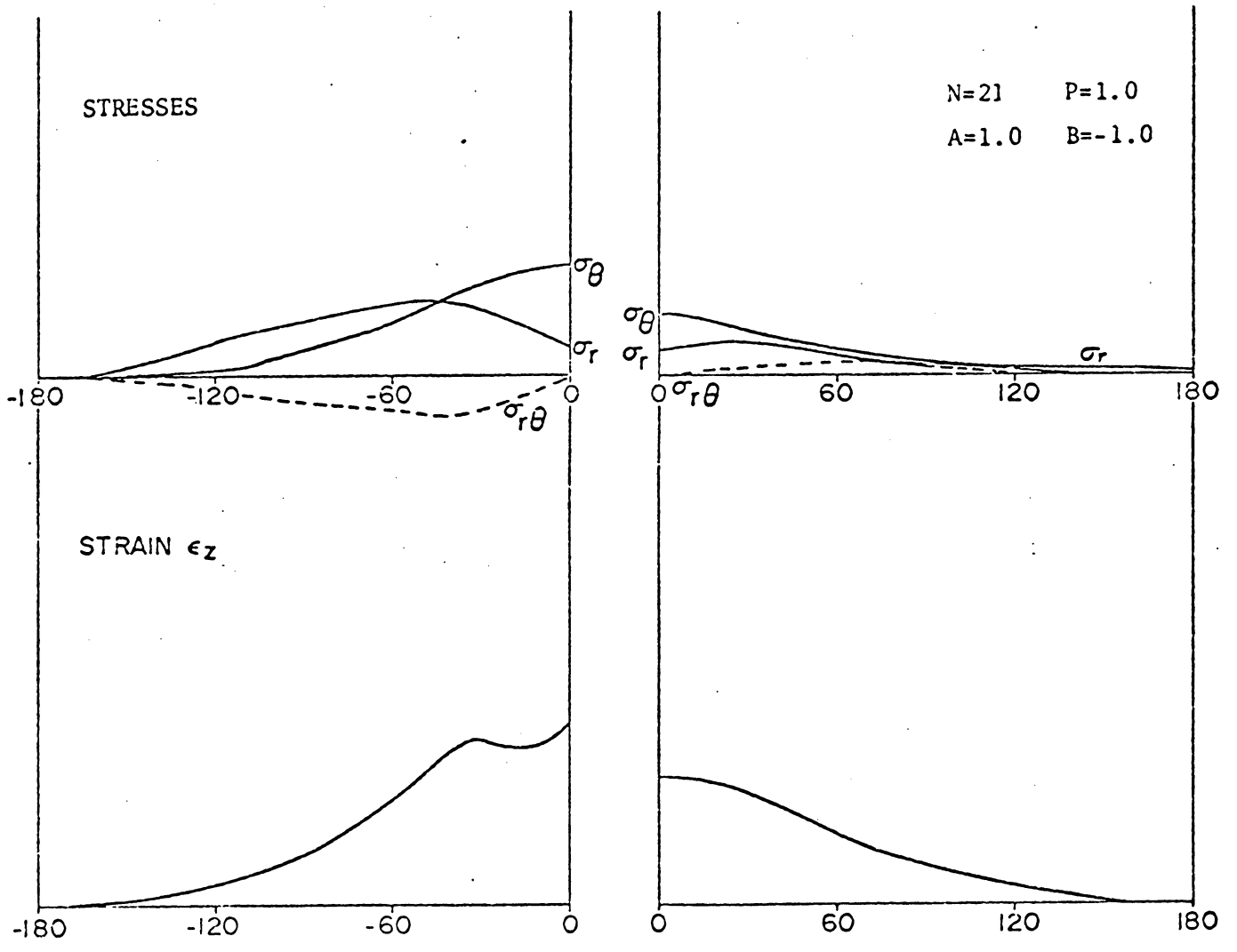

Figure 2-8 Angular variation of stresses and strain (ϵ_z) at a crack tip for -45° decreasing gradient with p = 1.0.

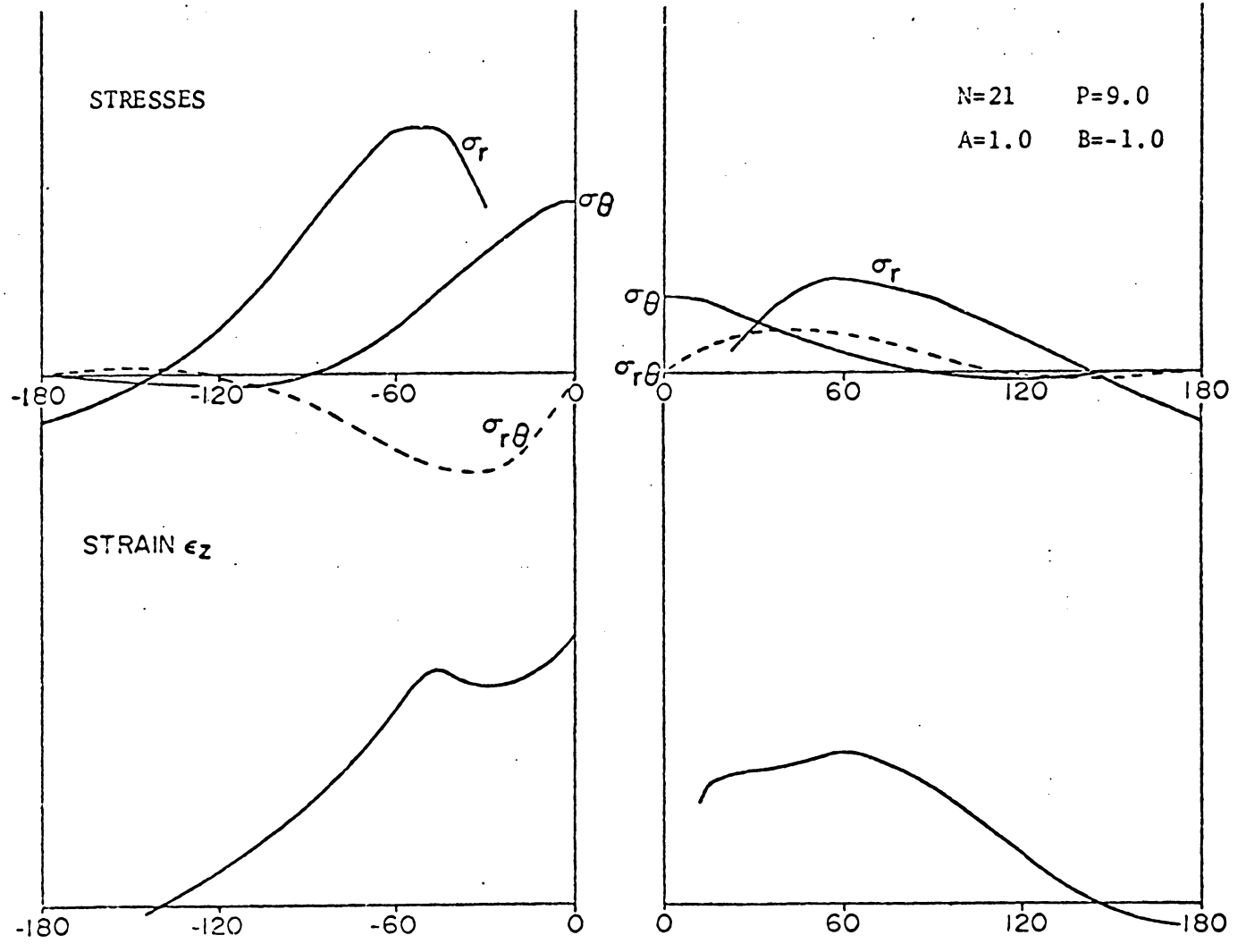

Figure 2-9 Angular variation of stresses and strain (ϵ_z) at a crack tip for -45° decreasing gradient with p = 9.0.

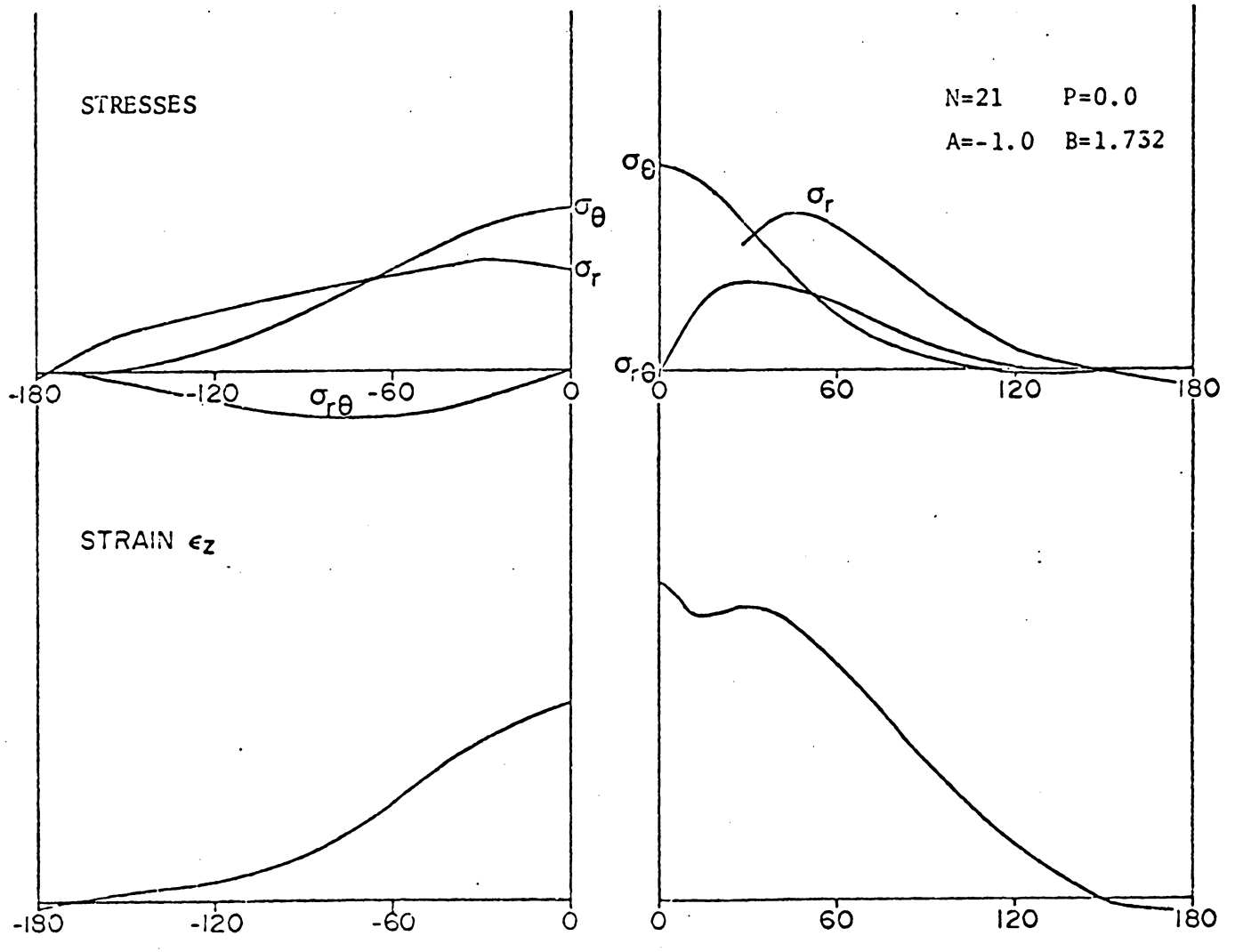

Figure 2-10 Angular variation of stresses and strain (ϵ_z) at a crack tip for -60° increasing gradient with p = 0.0.

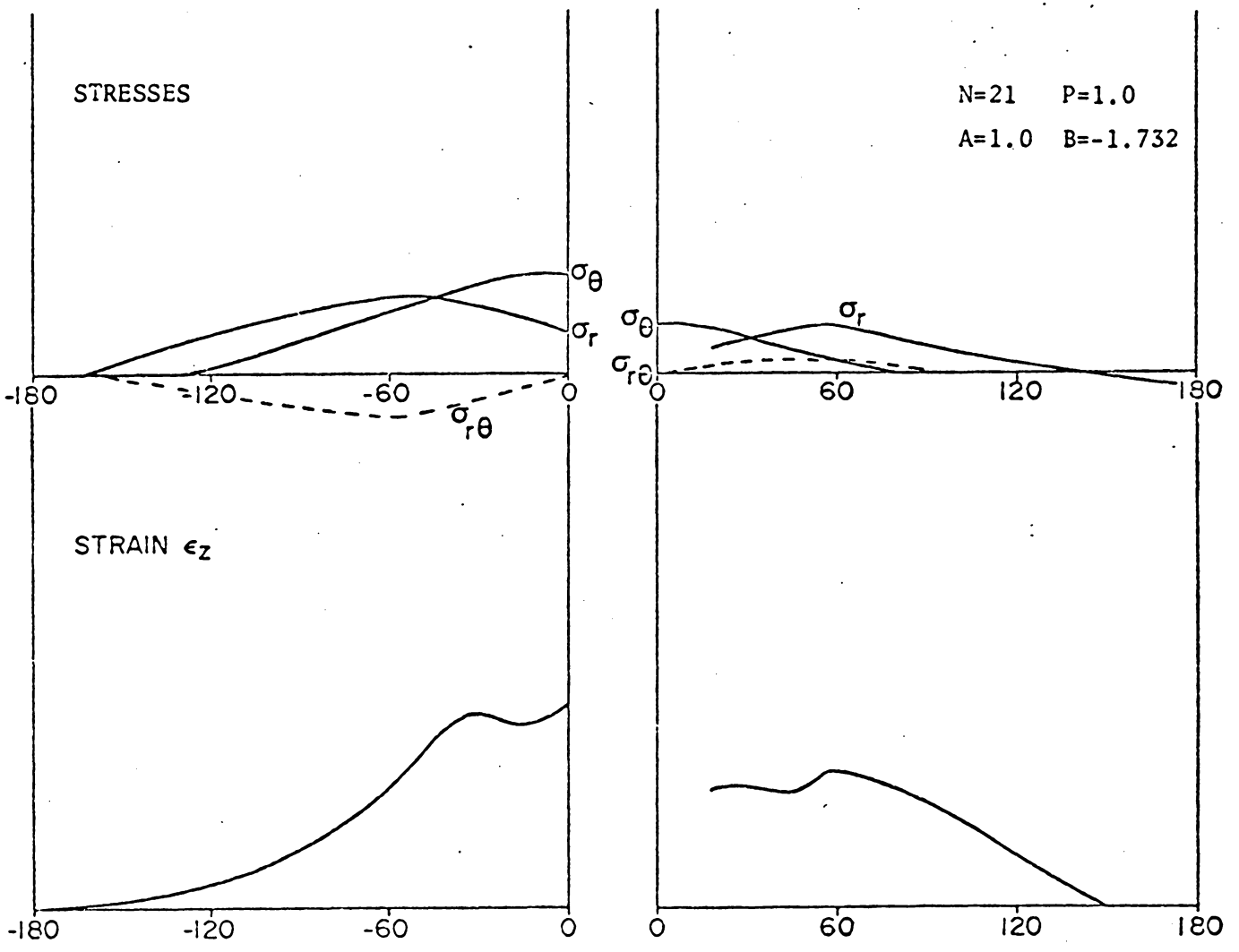

Figure 2-11 Angular variation of stresses and strain (ε_z) at a crack tip for -60° decreasing gradient with p = 1.0.

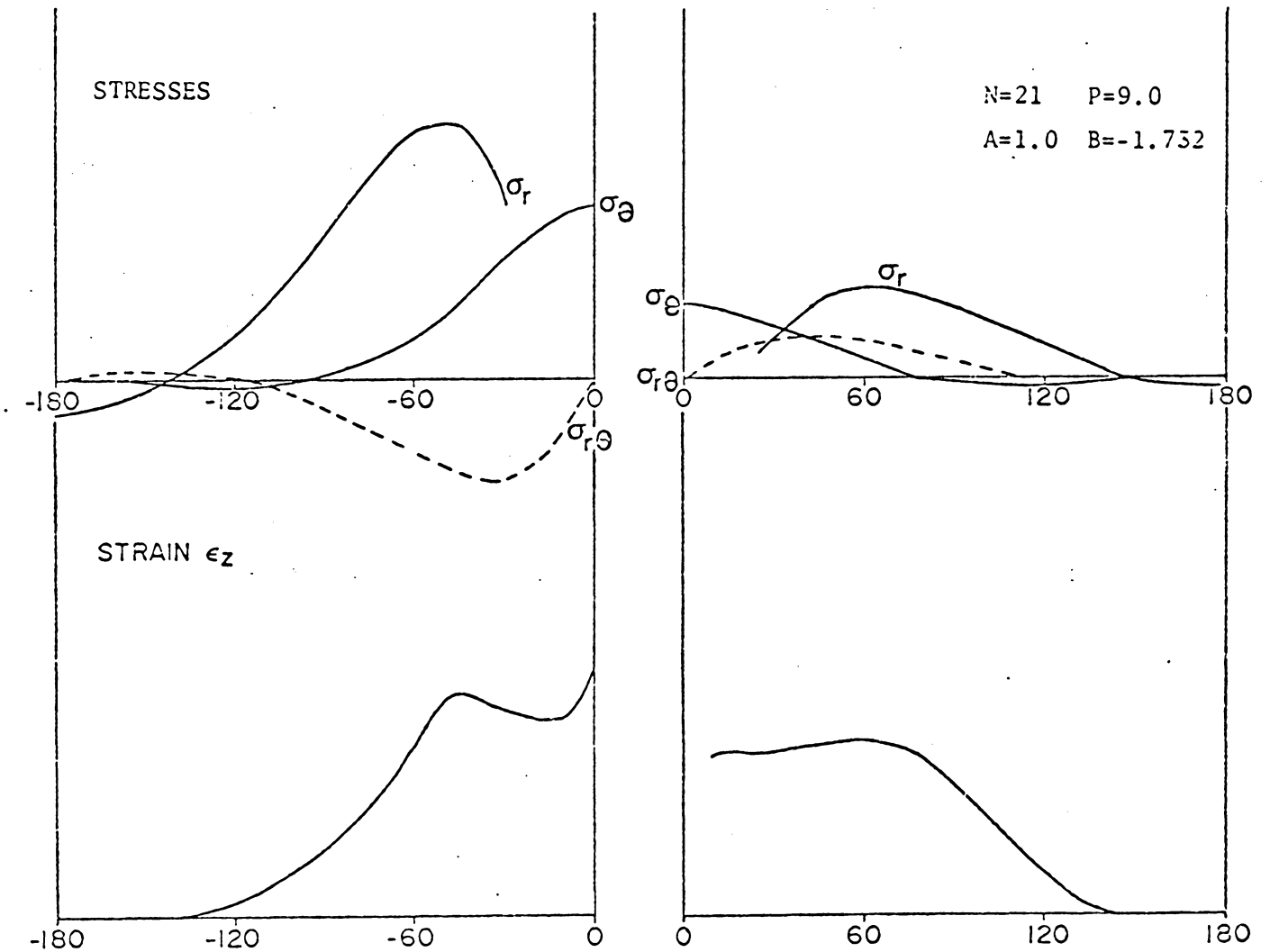

Figure 2-12 Angular variation of stresses and strain (ϵ_z) at a crack tip for -60° decreasing gradient with p = 9.0.

2.4 DISCUSSION AND SUMMARY

The present analysis has shown that the singular stress field at a crack tip can be controlled and dominated by nonlinear terms in the governing equation (2-15) that result from the nonlinear material response relationship which allows for spatial variations in material strength. Moreover, the analysis shows that if these strength variations, or yield strength gradients, do not occur with any natural symmetry about the crack axis, the resulting deformation field will not be symmetric. An approximate solution was used to establish the characteristic behavior predicted by the analysis. As a check on the method of solution, stress distributions predicted for the symmetric case when there are no strength gradients can be compared with earlier data from reference [3] and with the finite element results presented here. The data shown in Figure 2-3 is very similar to that shown in Figure 3a in reference [3], and general features of the data in Figure 2-2 can be compared with finite element results shown in Chapter III. It would appear that the analysis yields established results in familiar cases.

The first indication of the effect of strength gradients is seen by examining Figures 2-2 through 2-4 collectively. The stress distributions in the near-tip regions are enormously altered by the gradients. The crack-opening normal stress (σ_θ) is of special interest. That component reaches a sharper maximum at $\theta = 0°$ for the negative gradient case (p=+1) than for the uniform material case. But most interesting is the fact that σ_θ reaches its maximum at about

90° for the increasing gradient case and is much lower near $\theta = 0°$ in sharp contrast to the uniform case. This shift of the maximum crack opening normal stress was previously predicted by Kahl and Reifsnider on the basis of a much less exact finite element analysis [35]. Reifsnider and Kahl also reported experimental investigations which showed that this shift, and related effects, can be used to arrest crack propagation to various degrees by selectively heat-treating a material to achieve desirable strength gradients [36]. The present analysis indicates, by comparison, that the alteration of the stress distributions in general, and σ_θ in particular, is much greater in the near-tip region than in the more remote regions (still within the plastic enclave) considered by finite element methods.

It is not possible to make such strong ties with previous work for the unsymmetric case since no comparable examination has been carried out. However, some intuitive concepts are supported by the analysis and the basic prediction of unsymmetric deformation fields can be demonstrated experimentally. Figures 2-5, 2-6, and 2-7 show predicted distributions for a positive strength gradient in the -45° direction. The stresses and total deformation (ε_z) shift to the "weak" side of the crack axis, i.e., to positive positions. The basic symmetry of the deformation field no longer exists. As the strength of the gradient increases, the deformation in the positive gradient direction is inhibited, an effect shown earlier by Kahl and Reifsnider by analysis and experiment [35]. For large $|p|$ values, the stress distributions become very complex.

Instead of being an analogue to the positive gradient case, as it would be for the symmetric problem, the negative gradient case is separate and distinct as seen from Figures 2-8 and 2-9. As expected, the deformation now occurs preferentially in the gradient direction (-45°) since the material is weaker there. However, as the strength gradient becomes steeper (p=9), the deformation increases a great deal. Also, the stress distributions are quite distinct from the increasing gradient case. (Compare, for example, Figures 2-7 and 2-9).

Figures 2-10, 2-11, and 2-12 show related effects for a gradient direction of -60°. In Figure 2-10 the material is getting harder in the -60° direction (positive gradient) and, as for the 45° case, the deformation shifts to the weak positive-angle side. In fact, the stress distributions are quite similar to those of Figure 2-5. Figures 2-11 and 2-12 are negative gradient cases and show results quite similar to those of Figures 2-8 and 2-9.

The present work represents only a suggested beginning on the unsymmetric crack problem. Although the formulation is exact, several approximations were made during the subsequent characterization. A more thorough solution should be carried out to obtain more quantitative results. Experimental investigation of the problem is also needed and is presented in a later chapter.

CHAPTER III

FINITE ELEMENT TECHNIQUE - UNIMOD

In this chapter, a new concept in elastic-plastic analysis using finite element techniques is analyzed. The resulting procedural scheme, called Unimod, is found to be an effective method of performing stress analyses of complex elastoplastic defect problems which cannot be handled by classical elastic fracture mechanics. Advantages of the Unimod scheme include extreme versatility, universal applicability to existing programs and conceptual as well as operational simplicity.

3.1 UNIMOD - THE TECHNIQUE

The concept of Unimod can be extracted from an intuitive argument. A crack or defect is commonly analyzed by using a finite element grid with a very fine grid size (small elements) in the vicinity of the expected singularity, or by using special singularity elements to surround the tip. However, one is limited in the fineness of the grid by truncation error and, in other cases, by the size of the resulting system of equations that must be solved in view of available computer facilities. In any case, since the elements at the crack tip always have finite size, or employ a truncated series

representation, they are unable to represent a deformation singularity with complete accuracy. For the case of the common method of analysis based on the variational principal of minimum potential energy, the finite elements near a crack tip will always be too stiff. In a sense, the local stiffness of the material will always be overestimated, especially in the presence of plasticity. In such a situation, the singularity occurs in strain at the tip of the crack, while the stress distribution becomes relatively flat (although still singular if the material strain hardens). Strain hardening will control the actual value of stress near the tip, but the effective stiffness of the near-tip material is greatly reduced in the real material during plastic deformation near the strain singularity as large plastic strains develop. Since finite elements at the crack tip represent an average value of strain throughout their individual regions, that value, and the corresponding stiffness assigned to the element, will always be unrepresentative of the singular strain region. In particular, those elements will be too stiff compared to reality, and the predicted strains will be too small. The present scheme advances a simple solution to that problem, brought about by reducing the stiffness of a crack tip element or elements to a negligible value by definition, thereby forcefully creating a strain amplification which is constrained only by the surrounding "normal" elements. For convenience, a value of one psi is found to be an adequate approximation to a zero modulus value, without causing computational problems, hence the name Unimod. It so happens that any value which is two orders of

magnitude (or more) less than the elastic modulus produces essentially identical results. Actually, that fact makes Unimod an analysis scheme rather than a numerical manipulation. This process allows strain to develop at the crack tip more nearly as it does in real materials for elasto-plastic situations.

A conceptual similarity exists between Irwin's correction factor for small scale yielding and the Unimod scheme. The former argument states, among other things, that the linear elastic stress field description is reasonably accurate for the case of small scale yielding if the crack is assumed to be larger than reality by the amount:

$$r_y = \frac{1}{2\pi}\left(\frac{K}{\sigma_y}\right)^2 \qquad (3\text{-}1)$$

where K is the field stress amplitude (stress intensity factor) and σ_y is the material yield strength [39]. In other words, a certain volume (or strip) of material ahead of the crack tip is assumed to have negligible stiffness in order to determine the correct stress distribution with an elastic analysis for a mildly elasto-plastic case. Unimod can be thought of as a carry over of that concept to finite element analysis. In fact, we will see in the discussion section that r_y, as determined by elastic parameters, is, in many cases, an excellent estimate of the distance ahead of the crack which should be reduced to unit modulus if good agreement with experimental results is to be obtained. Hence, (3-1) can frequently be used to determine how many elements ahead of the crack should be relaxed to unit stiffness

for any grid to be used for such an investigation.

The results in the present report were obtained using the grid system shown in Figure 3-1 where nodes 1-33 define the crack axis which is an axis of symmetry for mode I loading. The crack was effected by releasing nodes 1-8 and 1-10 to model a single-edge-notched plate. For the experimental results used for comparison, the elements near the crack represented material elements 30 mils x 30 mils. As will be shown in the section on results, the results were extremely insensitive to any value of an element modulus below about 10^4 psi when that element (or several such elements) was embedded at the singularity in a matrix of normal elements. Fortunately, then, one need not attempt to determine a specific value for the stiffness of the singularity element. There is no loss of generality by reducing it to unity.

3.2 RESULTS USING UNIMOD

The technique of relaxing the modulus of elasticity has been carried out using E. L. Wilson's "Axisymmetric Solids Finite Element Program." [40] Plane stress conditions were assumed. Two strain hardening materials were considered, namely, 6061-T6 AL with a strain hardening ratio, $E_{plastic}/E_{elastic} = 0.04$ and 90-10 Brass with $E_{plastic}/E_{elastic} = 0.16$. A case of $E_{plastic} \simeq 0.0$ for AL was also examined to study the effect of change in grid size on stored strain energy.

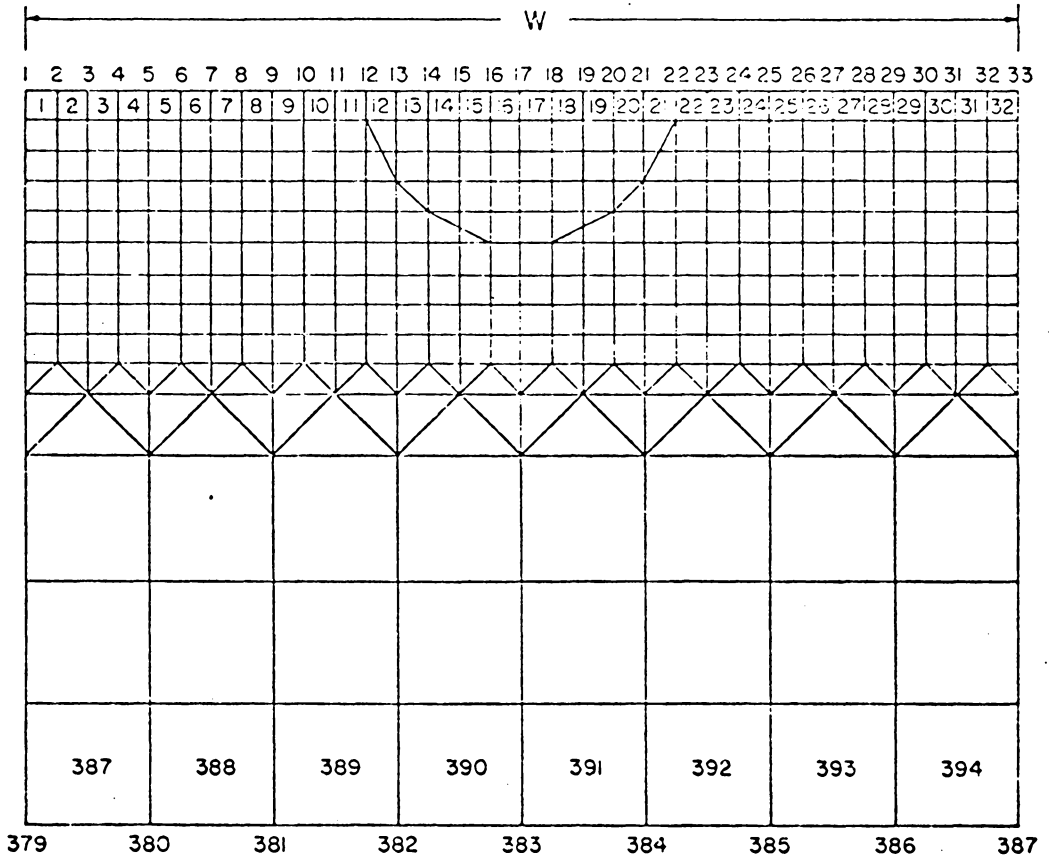

Figure 3-1. Finite Element Grid for the Geometry Modelled.

In the various figures described below, plots of stress and strain are made against distance along the crack axis, normalized by the crack length measured from the crack tip. Unimod I (8) is understood to mean that the elastic modulus of element number 8 (a crack tip element) has been reduced to the extent indicated. Unimod I (9), Unimod I (10) and Unimod I (11) have similar meanings. Unimod II (8 and 9) and Unimod II (10 and 11) have two elements, 8 and 9 and 10 and 11 respectively, with reduced modulus. The amount to which the modulus is reduced is indicated in the figures as $E = 10$, $E = 10^2$ or $E = 10^3$. The number of iterations carried out by the finite element analysis is denoted by "5 iterations," etc. All data will be compared with previous established results as reported by Underwood, et al., hereafter referred to as "the WVT report." [32] The constitutive bilinear idealizations used in the present analysis are compared to the actual stress-strain curves of the materials used in the WVT report in Figure 3-2.

In Figure 3-3, the remote applied stress is 15.13 ksi. Figure 3-3 shows the plastic strain distribution and clearly illustrates the manner in which the Unimod technique develops a more accurate high strain region close to the crack tip. Our normal program (with no modulus reduction) is seen to be unsatisfactory near the crack tip as it fails to rise quickly enough to pick up the singular strains. Calculated values from the WVT report are somewhat better than our normal program. However, the WVT reports' calculated values also rise much too slowly very near the crack tip.

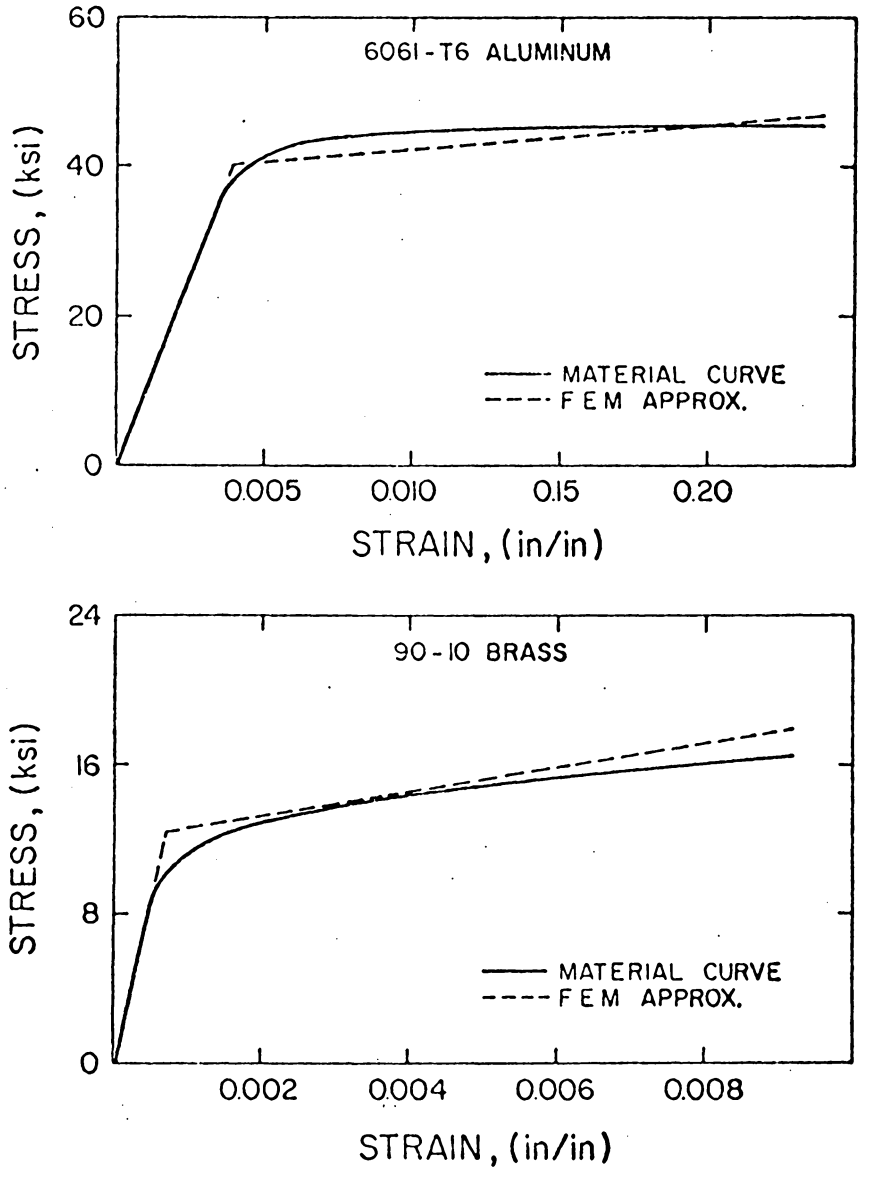

Figure 3-2. Approximations of Material Stress-Strain Response Used for Finite Element Method.

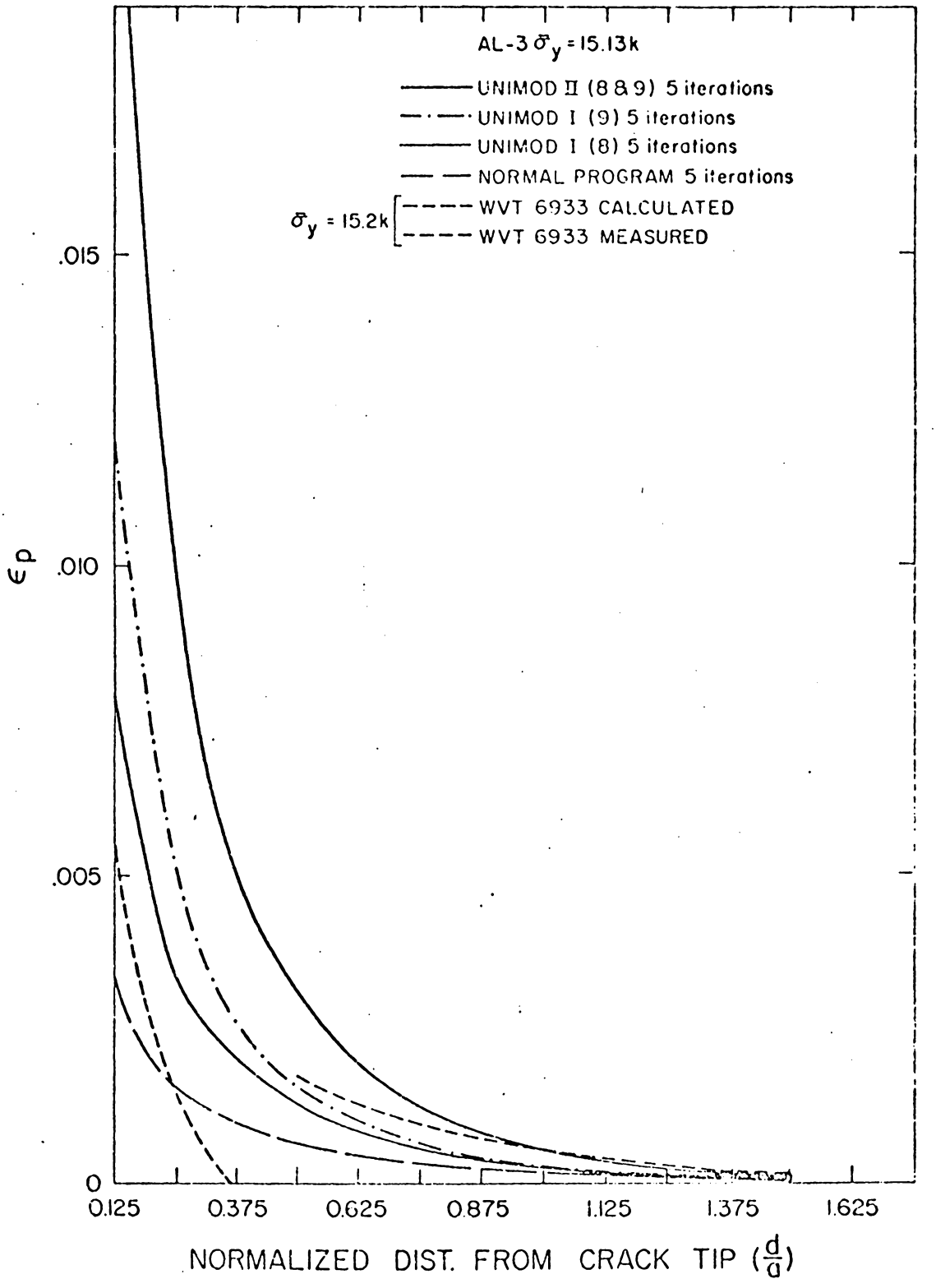

Figure 3-3. Plastic Strain Distribution vs. Distance Ahead of Crack Tip for 6061-T6 AL-3. $\bar{\sigma}_y$ = 15.13 ksi.

The WVT reports' measured plastic strains are very close to the Unimod data. Unimod I (8), Unimod I (9) and Unimod II (8 and 9) appear to be more representative of true plastic strains than both the WVT calculated values and our normal program. The lack of experimental measurements of plastic strains right up to the crack tip prevents complete comparisons. Corresponding stress distributions were found to be marginally different; the Unimod analyses indicated higher stresses close to the crack tip. It should be emphasized that the "normal program" data and that produced by Unimod II (8 and 9) were produced by the same computer program. The only change that was made was that elements 8 and 9 near the crack tip were required to have an elastic modulus of unity in the second case. The grid used was rectangular, with characteristic dimensions of about 0.03 in. near the crack tip (see Figure 3-1).

With increasing remote load, the inadequacy of the normal program becomes more apparent, as shown in Figure 3-4. Here the remote stress is 20 ksi, i.e., about half the yield stress. There is also a marked underestimation of the plastic strains by the WVT (calculated) data. An interesting feature of Figure3-4 is the nature of the good fit between Unimod II (8 and 9) for total strains and the WVT (measured) unloaded strains. In cases of high remote loading ($\sigma_y \simeq \frac{\sigma_{yield}}{2}$), the plastic zone apparently prevents some relaxation of the elastic singular stresses near the elasto-plastic boundary. Plastic strains calculated by the Unimod II (8 and 9) scheme, and the measured strains match well nearer the crack tip. Again, the

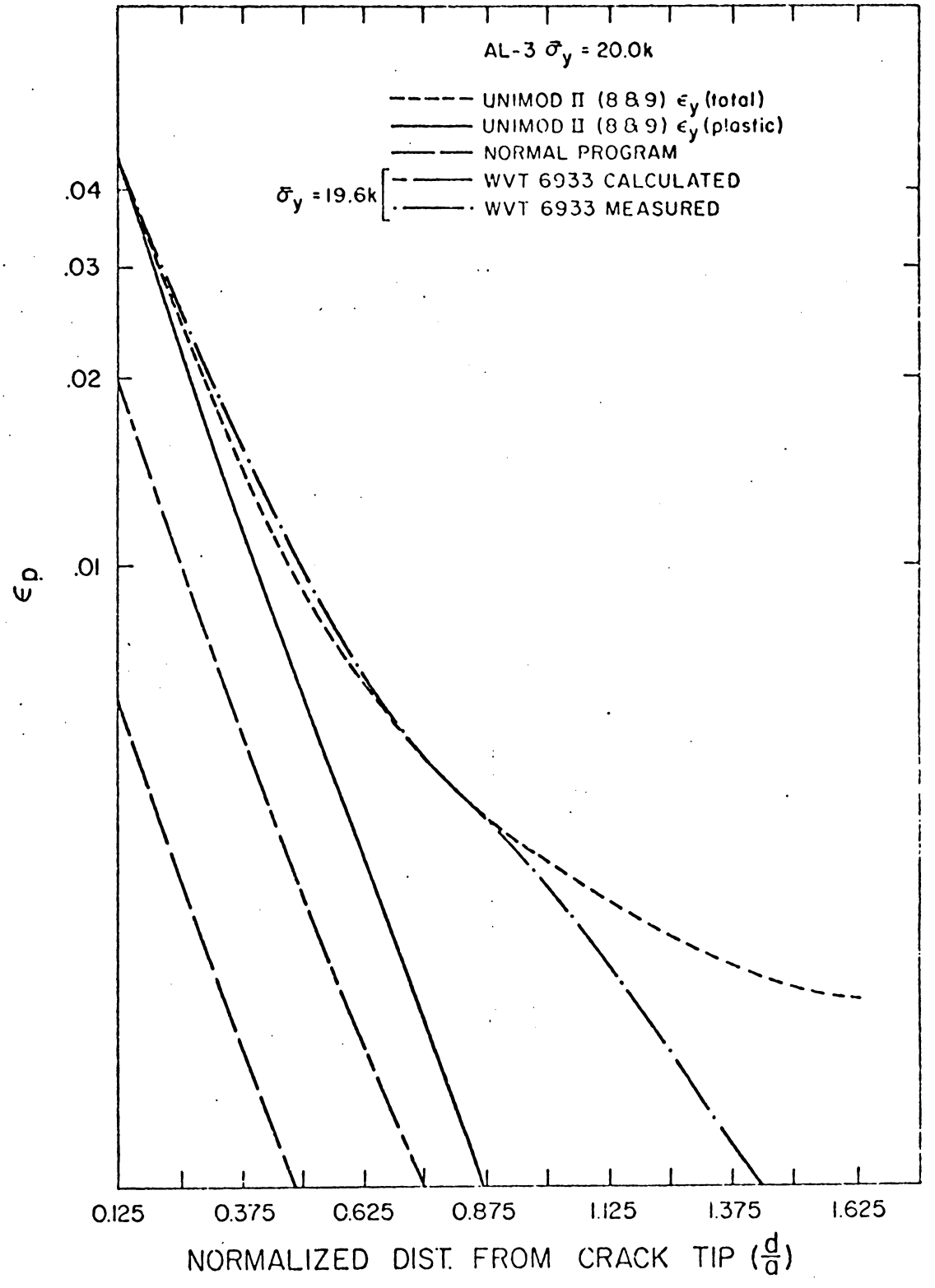

Figure 3-4. Strain Distributions vs. Distance Ahead of Crack Tip. 6061-T6 AL-3. $\bar{\sigma}_y$ = 20.0 ksi.

stress distributions were found to be comparable to each other.

In Figures 3-5 through 3-7, a different strain-hardening material, 90-10 Brass, is analyzed. For a remote stress of $\bar{\sigma}_y$ = 7.5 ksi, Figure 3-5 clearly differentiates the high strain region developed by Unimod II and the normal program. Here the yield stress is much lower than that of aluminum; consequently, $\bar{\sigma}_y$ = 7.5 ksi is greater than half the yield stress. As expected, the Unimod II (8 and 9) analysis comes closer to the available measured data. As noted previously, the total strains calculated by the Unimod II analysis more accurately match the elastic singular region of the measured values. Strain distributions for an increased loading ($\bar{\sigma}_y$ = 8.5 ksi) are shown in Figure 3-6. In this case, the Unimod II results appear to overestimate the strains. The effect of changing the value of the local elastic modulus was also studied in this figure. It was found that there was no apparent change in the strain (or stress) distributions when the elastic modulus of the Unimod elements was varied by three orders of magnitude, i.e., E = 10 psi, 10^2 and 10^3 psi. In other words, it did not matter how small the elastic modulus at the crack tip was chosen to be as long as it was several orders of magnitude less than the normal elastic modulus. This fact adds greatly to the versatility and generality of the Unimod technique.

Figure 3-7 is a normalized stress representation for 90-10 Brass for $\bar{\sigma}_y$ = 8.5 ksi. Unimod analysis stresses are somewhat higher than the normal program stresses near the crack tip. Both the

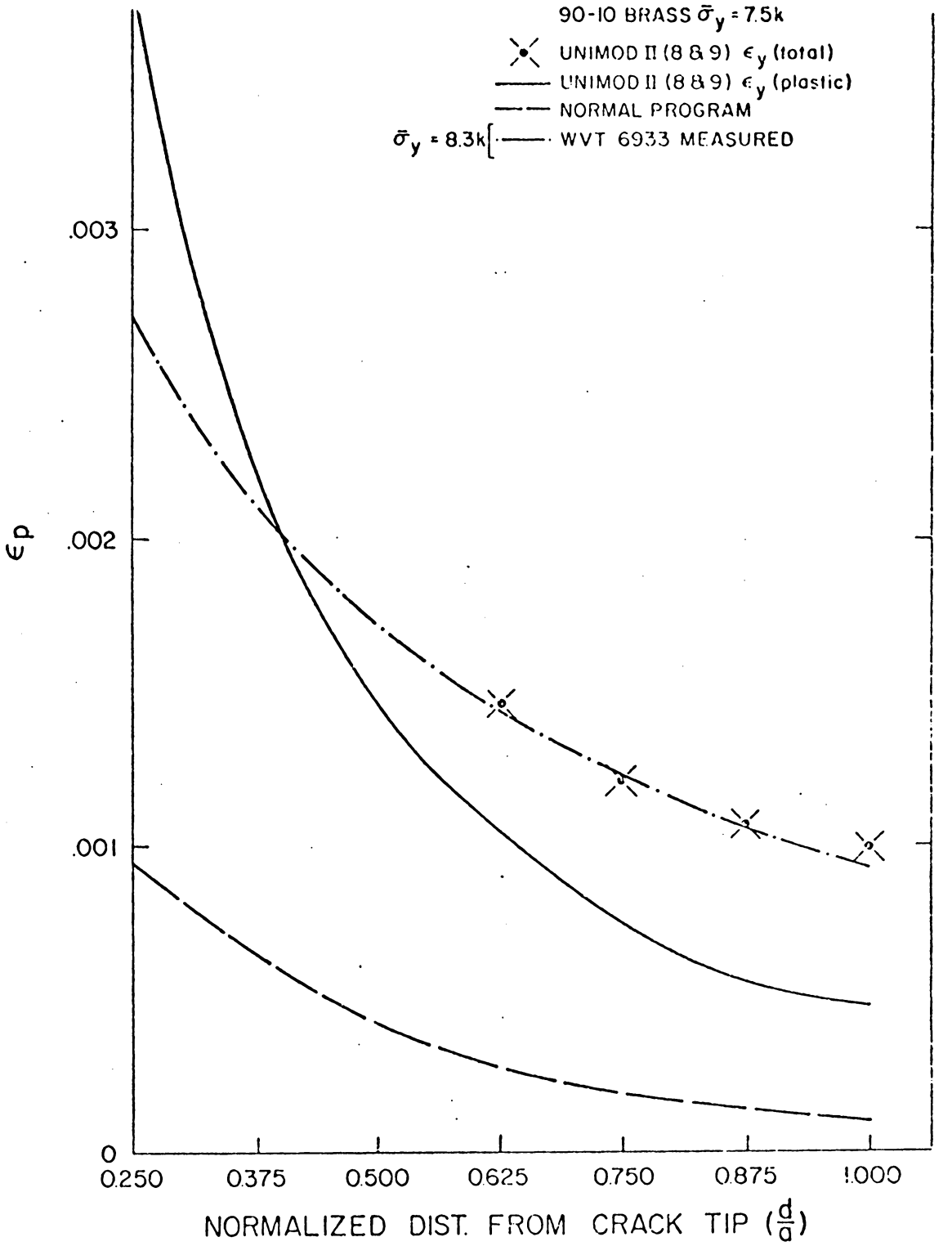

Figure 3-5. Plastic Strain Distributions vs. Distance Ahead of Crack Tip. 90-10 Brass. $\bar{\sigma}_y$ = 7.5 ksi.

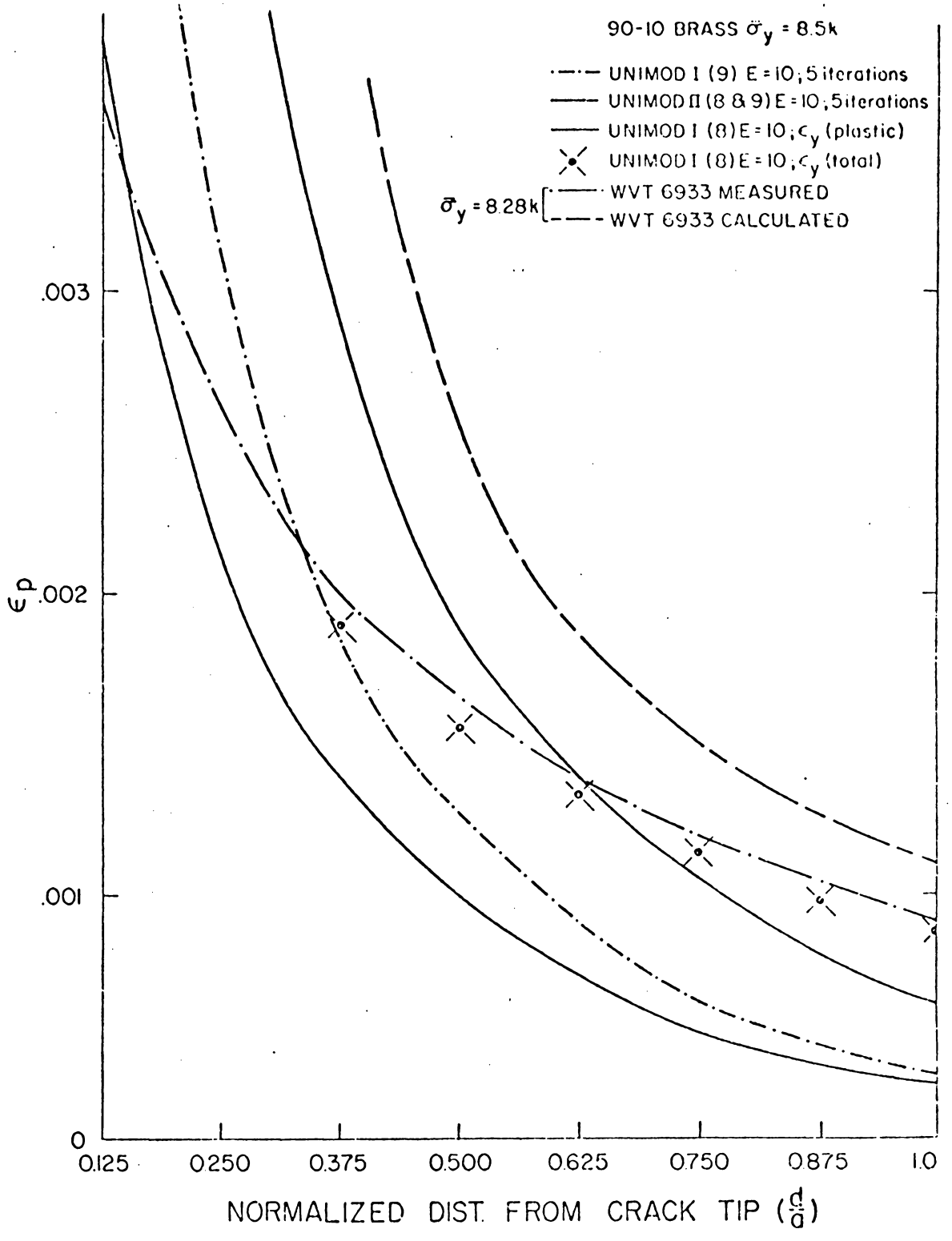

Figure 3-6. Plastic Strain Distributions vs. Distance Ahead of Crack Tip. 90-10 Brass. $\bar{\sigma}_y$ = 8.5 ksi.

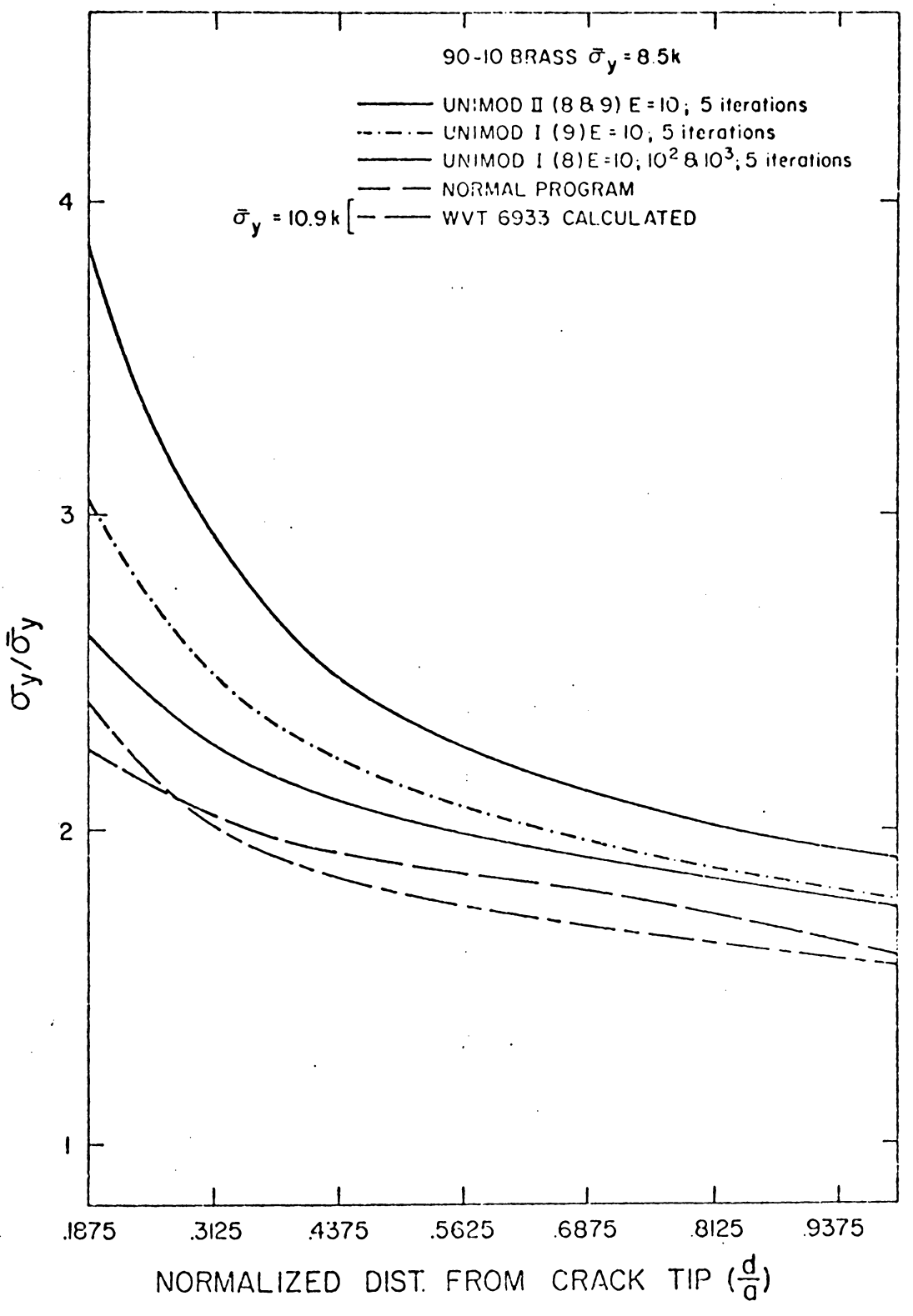

Figure 3-7. Normalized Stress Distributions vs. Distance Ahead of Crack Tip. 90-10 Brass. $\bar{\sigma}_y$ = 8.5 ksi.

stress (and strain) distributions converge away from the crack tip. This fact is also demonstrated by Figure 3-3.

In general, it was found that, with increasing remote load, Unimod II produced the best results for strain distributions at a singularity in the present case; at the same time, the corresponding stresses appeared to be reasonable. At lower remote loads either Unimod I (8) or Unimod I (9) was satisfactory. It is necessary, however, to establish a method of optimizing the choice of elements to be assigned reduced stiffness for problems when no experimental data is available to support a post-analysis evaluation. Two such methods, described below, are suggested by the author.

A fairly widely accepted criterion for the choice of an optimum finite element grid, in general, is the uniformity of the strain energy values for each element throughout the grid system. For singularity cases, this idea can be extended so that an optimum grid is one in which the average energy of the elements in the singular region is as near as possible to that of elements remote from the singularity in the uniform stress region. This technique is illustrated by Figure 3-8 and can be used as a quantitative method for the determination of the optimum number of relaxed elements. Figure 3-8 shows that the Unimod II analysis should be optimum for this case of high remote (applied) stress which is borne out by comparison with experimental data. (See Figure 3-4 for example). It so happens that the average energy per element for the Unimod II scheme is nearly identical to the remote average in this case. This criterion is a

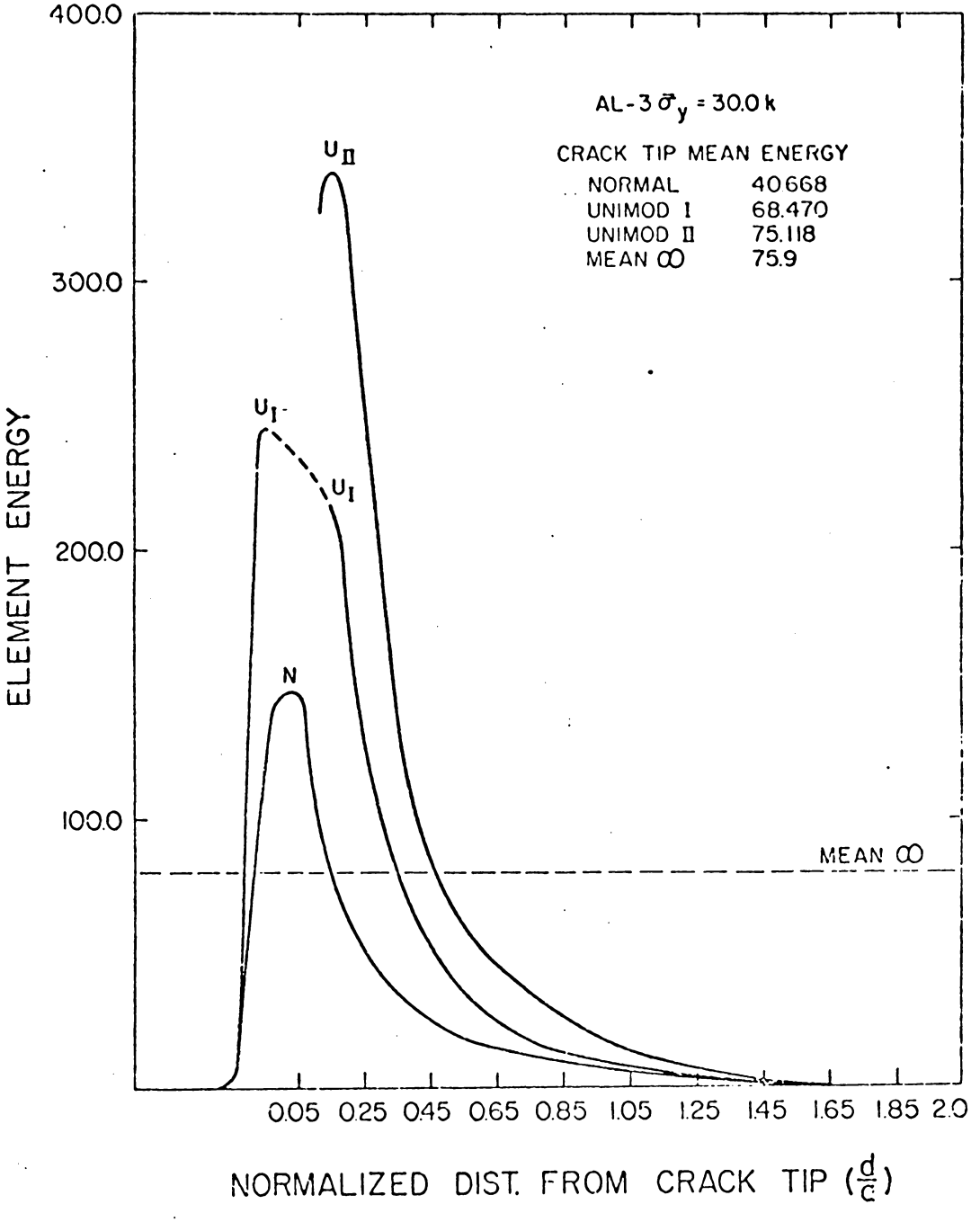

Figure 3-8. Strain Energy per Element as a Function of Distance from the Crack Tip Along the Crack Axis with Corresponding Average Values in the Singular and Remote Regions.

sensitive one as can be determined by the large differences between mean energies for Unimod II, Unimod I and the normal program.

A more direct optimization scheme is afforded by analogy to the Irwin correction factor for small scale yielding, as discussed in the introduction. If that analogy holds, r_y should predict the distance ahead of the crack that should be assigned negligible stiffness. For our edge crack specimen,

$$r_y = \frac{a}{2}\left[C\,\frac{\sigma_\infty}{\sigma_y}\right]^2 \qquad (3\text{-}2)$$

where C is a function of the ratio of crack length, a, to specimen width, w, and σ_∞ is the applied remote stress. For the present case of aluminum with σ_∞ = 20.0 ksi, σ_y = 39.8 ksi, C = 1.29 for a/w = 0.3 and a = 0.3 in for unit width, r_y = 0.063 in. For the present grid, two elements would have a width of 0.0625 in. so that this technique would predict that Unimod II results would be very good for this case. Figure 3-4 shows that this is, in fact, so. For the present case of aluminum with σ_∞ = 15.13 ksi, σ_y = 39.8 ksi, C = 1.29 for a/w = 0.3 for unit width, r_y = 0.036 in. The method then predicts that Unimod I should be used with the present grid for most accurate results. Figure 3-3 verifies this prediction with experimental evidence. Similar results are obtained for the brass analyzed. This simple and direct method worked very well, in general, for our present analysis. However, results obtained using r_y are most satisfactory for nearly-perfect plastic materials and small scale yielding.

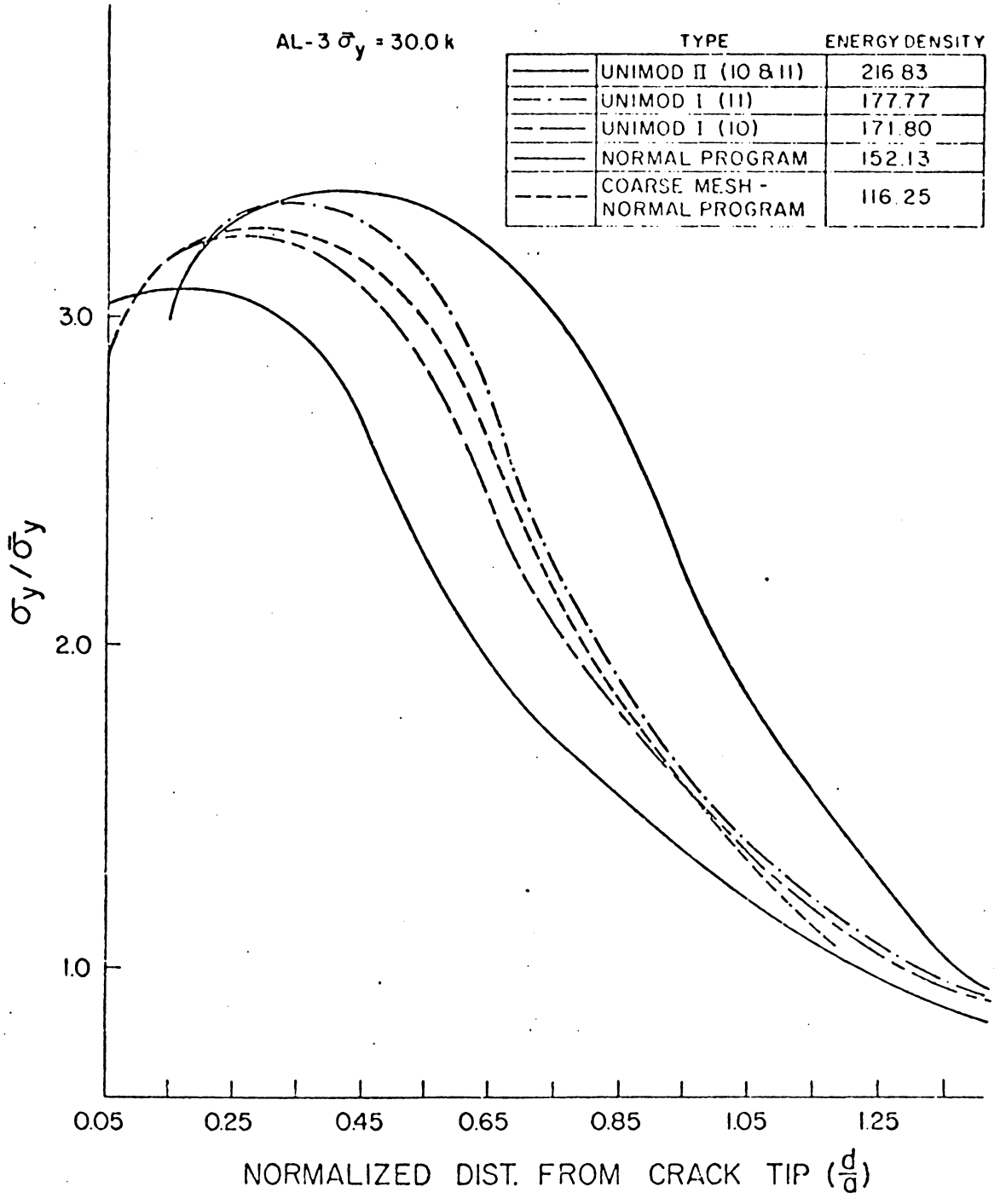

Figure 3-9. Normalized Stress Distributions vs. Distance Ahead of Crack Tip. 7076 AL. $\bar{\sigma}_y$ = 30.0 ksi.

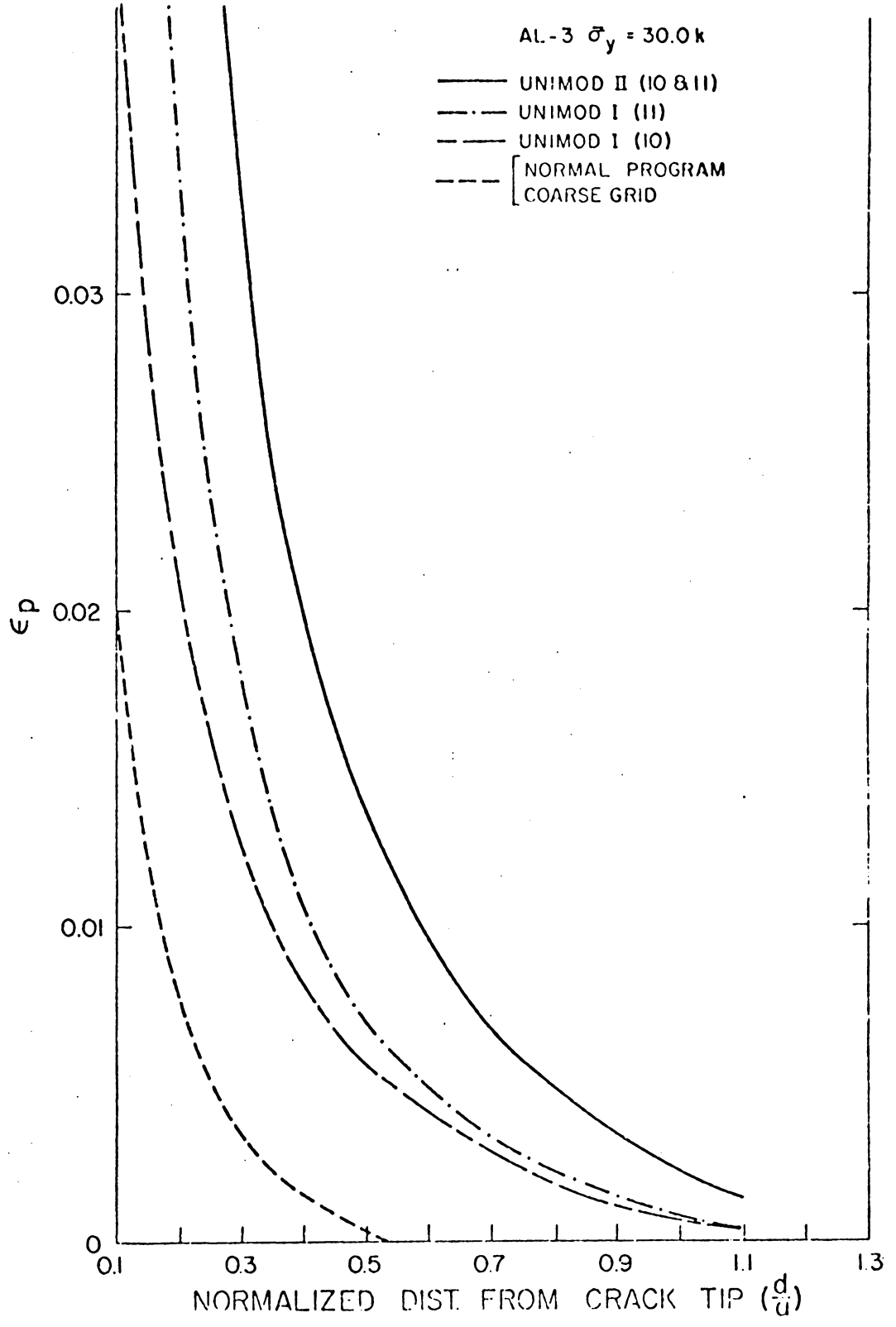

Figure 3-10. Plastic Strain Distributions vs. Distance Ahead of Crack Tip. 7076 AL. $\bar{\sigma}_y$ = 30.0 ksi.

Comparisons with change in grid size are studied in Figures 3-9 and 3-10. 7076 AL was modeled with $E_{plastic}/E_{elastic} \approx 0.0$ and a remote load of 30.0 ksi was applied. Figure 3-9 is a stress plot, and shows that the various curves tend to converge away from the crack tip. In the top of the figure is inset the stored strain energy values for the various types of analyses. The coarser the mesh, the lesser the stored potential energy. The changes in grid size are analogous to the various Unimod analyses. This aspect of the relationship can be verified by the respective stored potential energies in each case. Figure 3-10 shows a smaller plastic zone for the coarser grid size. As before, the high strain region is well developed by the Unimod analyses for this material with no strain hardening.

3.3 DISCUSSION AND CONCLUSIONS

The data reported above (as well as a larger body of data in reference [41]) indicate that a simple singularity element can be obtained by reducing the elastic-plastic modulus of the element to unity. Some advantages of the method are the following:

1. It is completely general, i.e., it can be used for any finite element program.
2. It is simple. It does not require major additions to a standard finite element program in order to develop a useful analysis of a crack or other singular defect.

3. It is extremely versatile. The most obvious point in support of this fact is made by noting that no special grid or specimen geometry is associated with the method. A crack, for example, can be inserted, removed, lengthened, or moved about from place to place using the same (reasonably fine) grid, a significant advantage to the fracture analyst or engineer. Moreover, changes of geometry do not affect it.
4. It is a flexible method. As shown by the present data, the method can be used for materials with widely varying strain-hardening characteristics. No special adaptation would be necessary to apply the technique to non-uniform materials.

The limitations of the Unimod technique should also be noted. To the extent that the choice of the number of elements near the crack tip to be relaxed to unit stiffness is discretionary, that decision represents a limitation on the accuracy of the method. However, this matter has been addressed from the standpoint of element strain energy values and relaxed length determinations based on the Irwin correction factor quite successfully in the present case. The degree to which this limitation can be overcome can be determined only by the success or failure of future applications. It should be noted that choosing the number of elements to be relaxed is an optimization process exactly analogous to choosing a specific discrete element grid. Changing the number of relaxed elements, however, is far simpler than

changing the element grid.

A second limitation is created by the relaxation process itself in that the data generated by the relaxed elements themselves are not necessarily representative, at least so far as we are able to interpret it at this time. This is an important limitation since crack tip information needed for some fracture criteria is lost. However, since the other data in the neighborhood of the tip is improved, criteria such as the J-integral could be used with improved accuracy.

Finally, it should be emphasized that Unimod does not, in general, produce data with the same accuracy as many of the highly sophisticated specialized singularity programs in use today. However, the author has found it to be a very useful alternative to such methods which we use in more demanding circumstances. It is also believed that there is an urgent need for relatively simple, general methods of analysis which can be used by engineers to solve practical fracture mechanics problems which are beyond the scope of linear elastic fracture mechanics. Unimod is a step in that direction.

CHAPTER IV

FINITE ELEMENT ANALYSIS WITH MATERIAL VARIATIONS

The inadequacy of a single parametric representation (namely, the stress intensity factor) of fracture phenomena was discussed in earlier chapters. With the introduction of spatial material variations into the crack tip region, the problem of defining an adequate functional form for the crack tip behavior becomes compounded. Singular elements generated for any finite element analysis are, therefore, subject to severe limitations.

In this chapter, a finite element analysis is carried out, using constant strain triangles (CST) and without any 'singular elements.' The purpose of this analysis was primarily two fold. First, to study the effect of material variation on the stress and strain distributions around a crack tip, and second, to determine the elastic-plastic boundaries in each case. It should be noted that by the very nature of the problem, the stress and strain values are obtained only at finite distances away from the crack tip. Here, the discretization process and the fineness of the respective mesh sizes are important.

4.1 FINITE ELEMENT DISCRETIZATION

Wilson's two dimensional program [40] was used in this analysis. By including spatial material variations, the symmetry of the

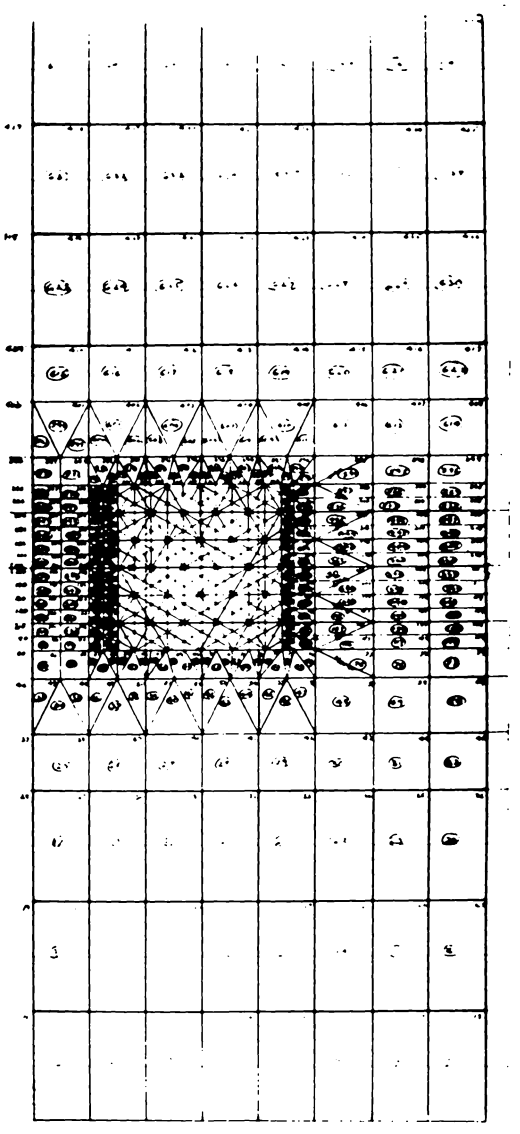

Figure 4-1. Finite Element Grid System.

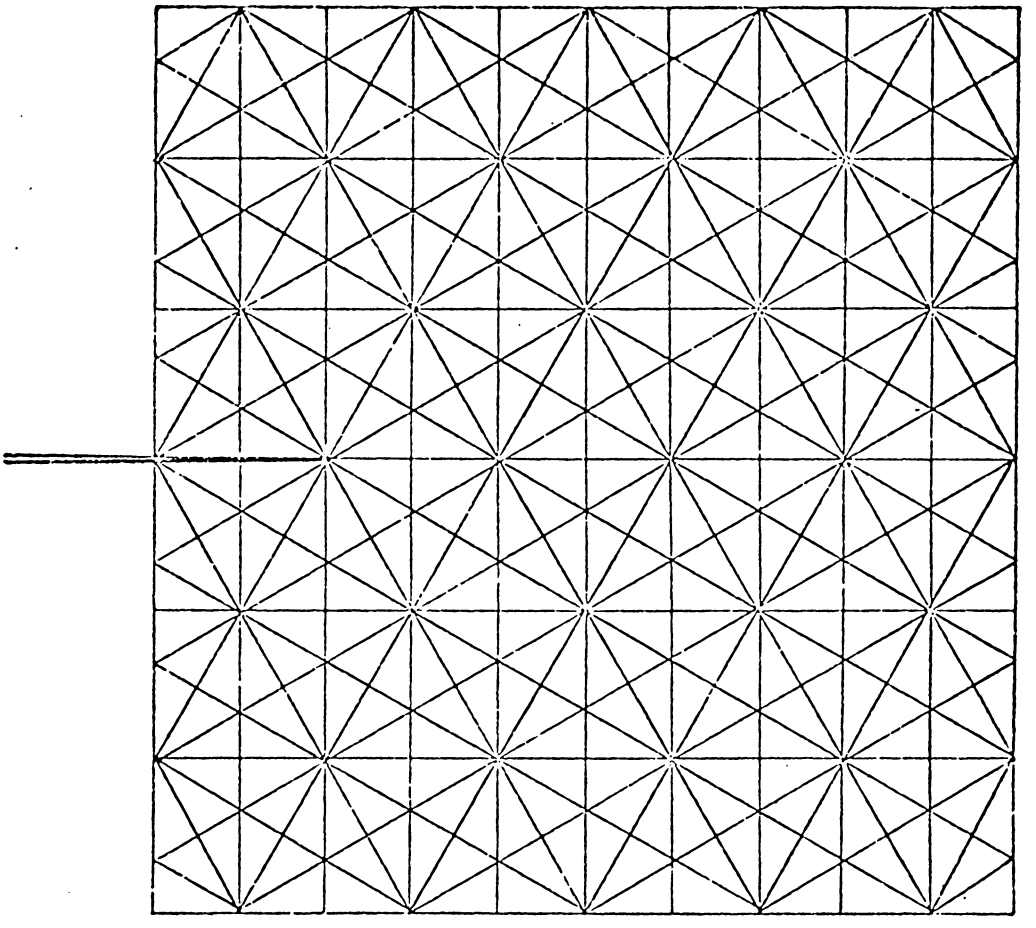

Figure 4-2. Crack Tip Region Fine Mesh.

plate under consideration was lost. As a result the entire edge cracked plate was discretized. The discretized system is shown in Figure 4-1.

The discretized system has 646 elements (both triangles and rectangles) and 444 nodes. The area of interest, i.e., the crack tip region, has a fine mesh of congruent triangles (Figure 4-2). This fine mesh was drawn in such a way so as to facilitate material variations in -90°, -60°, -30° and 0° directions around the crack tip. The edge crack was represented by a system of double noding. It was possible, with the above mentioned grid system, to keep a sufficient number of degrees of freedom, and at the same time maintain a small band width. The program was, therefore, efficiently used.

4.2 RESULTS OF SPATIAL MATERIAL VARIATIONS

Figures 4-3 and 4-4 are plots of stresses around the crack tip. Figure 4-3 was a -30° decreasing gradient case for two loading situations. Plasticity has fully developed for σ_∞ = 20.0 ksi and σ_∞ = 25.0 ksi. The extent of plasticity is represented by the straight line drawn below the stress plots. Numbers indicated on the plastic lines are the maximum strain energy values of an element for negative and positive angles. The unsymmetric nature of σ_r and σ_θ became prominent with higher loads. $\sigma_{r\theta}$ stresses show oscillatory behavior--it can be interpreted to be the edge effect in the finite element approximations. The maximum strain energy values appeared on the softer side. It is also evident that the plot of strain energy

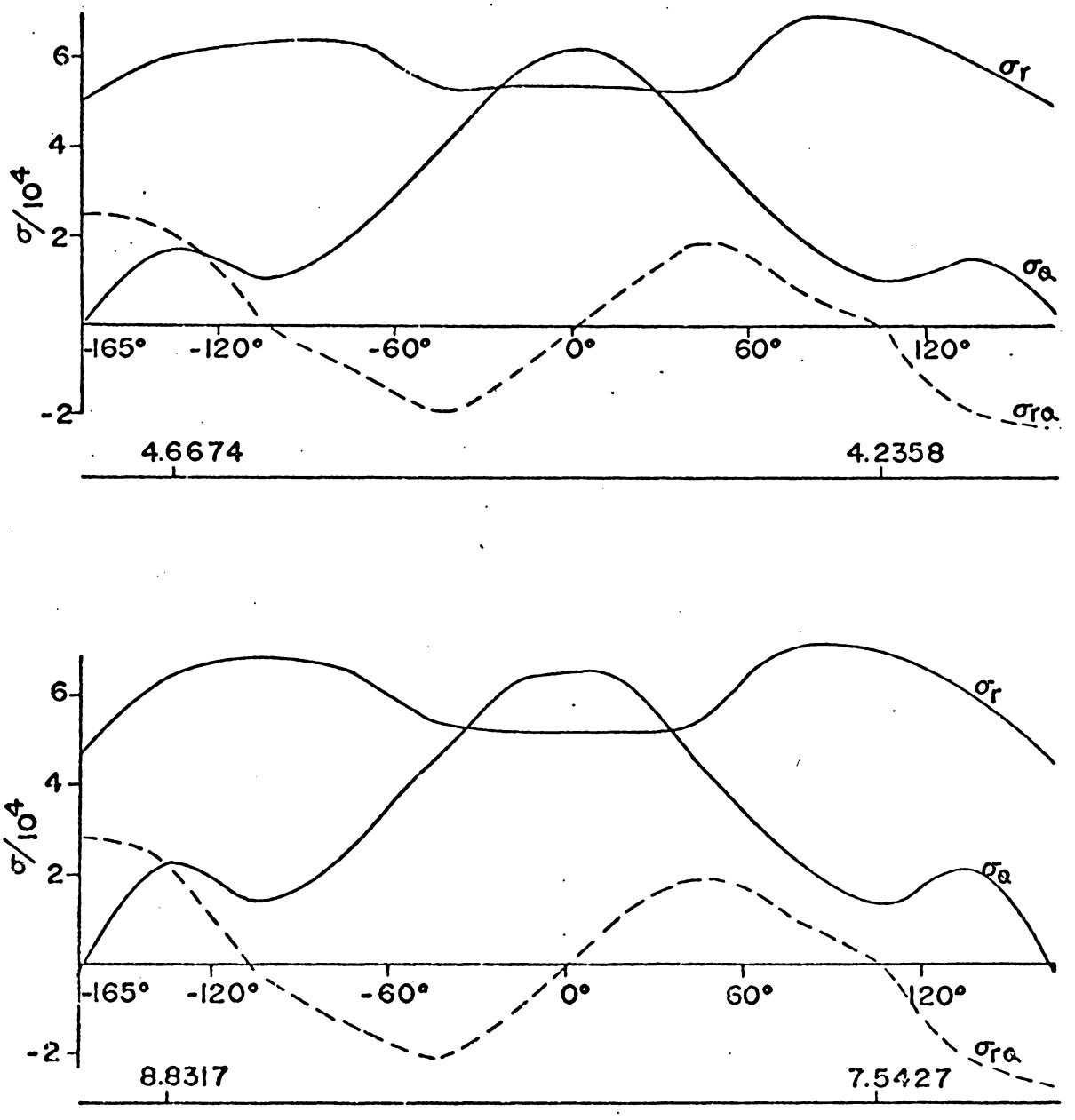

Figure 4-3. -30°; -GRAD a) 20.0 ksi b) 25.0 ksi.

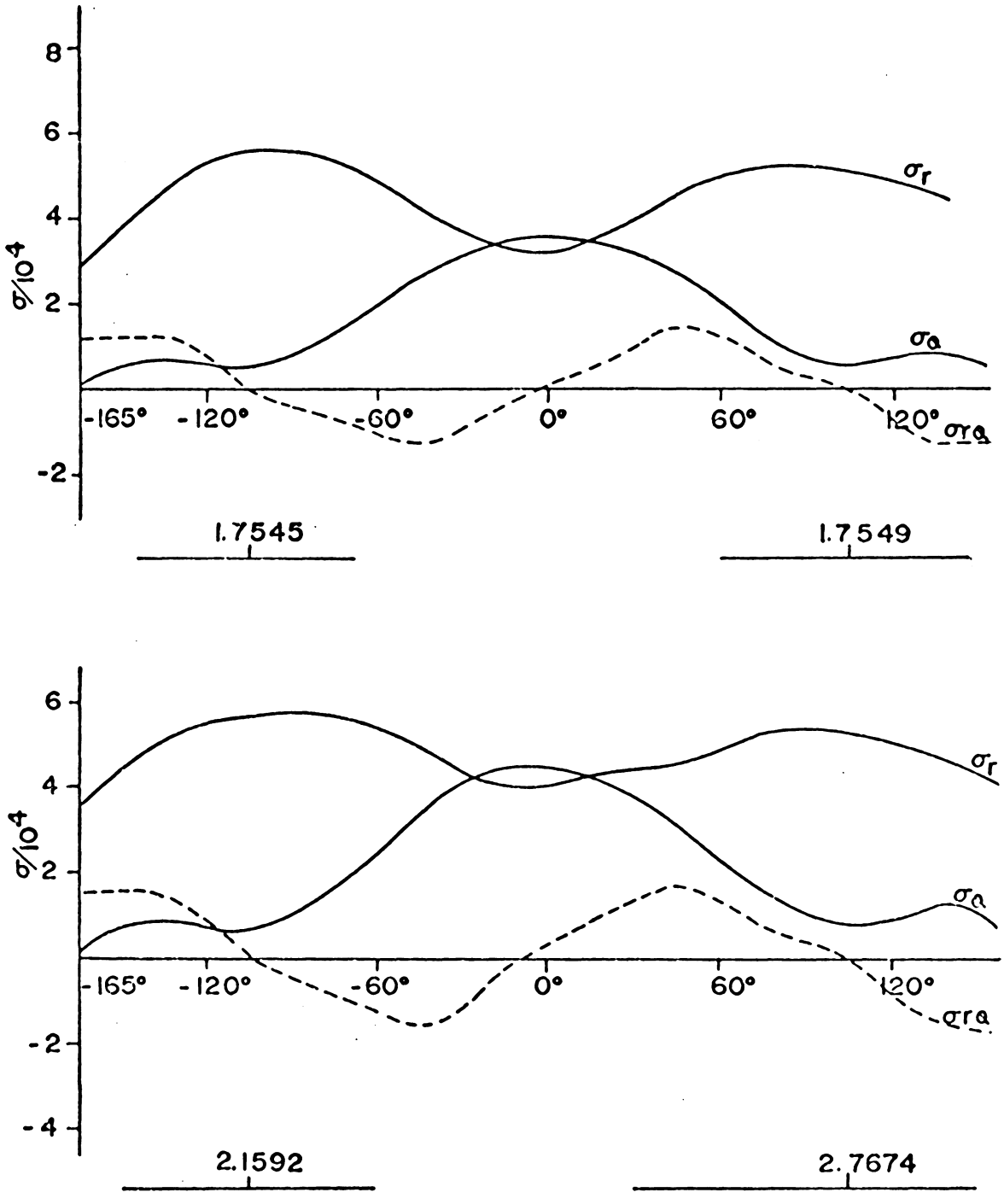

Figure 4-4. -90°; +GRAD a) 12.5 ksi b) 15.0 ksi.

around the crack tip would be unsymmetric. However, the maximum value of σ_r appeared on the harder side. The crack opening stress σ_θ maximized at the 0° angle for lower loads. There was a tendency for the σ_θ stress to maximize toward the harder material side. It is difficult to conjecture the exact effects of the material variations by looking at the stress plots. At the same time, there is adequate evidence of nonsymmetry in the pattern of stress distributions. Figure 4-4, a -90° increasing gradient case, displayed similar tendencies to those described for Figure 4-3. In this case plasticity had not completely developed around the crack tip.

Figures 4-5 and 4-6 are stress plots for a -60° decreasing gradient case with a remote applied stress of 30.0 ksi. The total stresses in Figure 4-5 do not show significant nonsymmetry. However, after removing the elastic stresses from Figure 4-5, Figure 4-6 was obtained--displaying the somewhat nonsymmetric plastic stresses. It is interesting to note the nonlinear behavior of σ_r. Also, in the 0° direction, σ_r behaves very irregularly. The asymptotic analysis of Hutchinson [4] also predicted irregularities in σ_r in the 0° direction.

Figures 4-7 through 4-10 are γ_{oct} (strain) distributions for decreasing gradient cases. The strain distributions are much more demonstrative than the stress plots. In all the strain distributions, the primary and dominant maxima occurred in the softer regions. With increasing load, the position of the maxima shifted marginally in the direction of the crack axis. There does not seem to be any

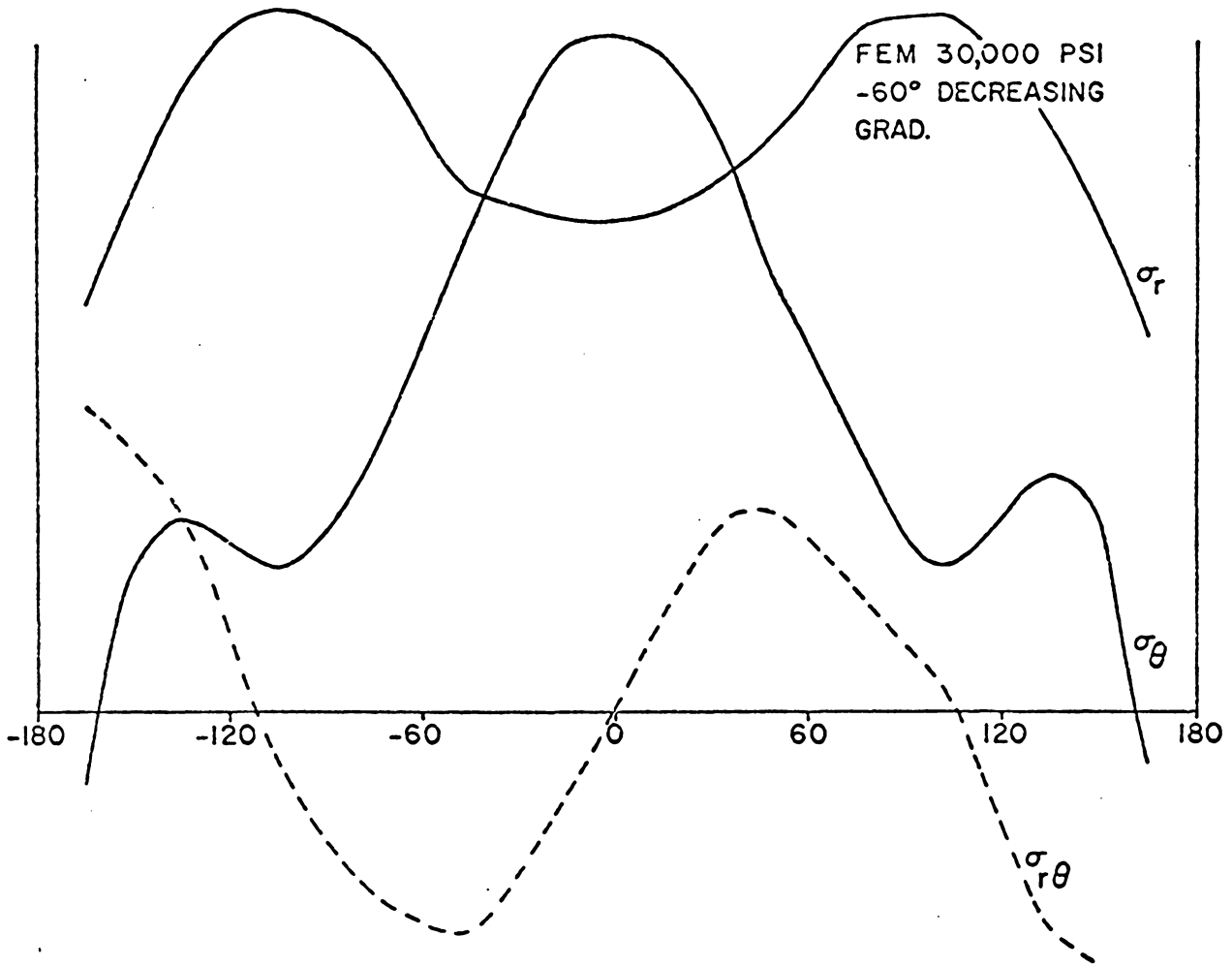

Figure 4-5. -60°; -GRAD, 30.0 ksi (Total Stresses).

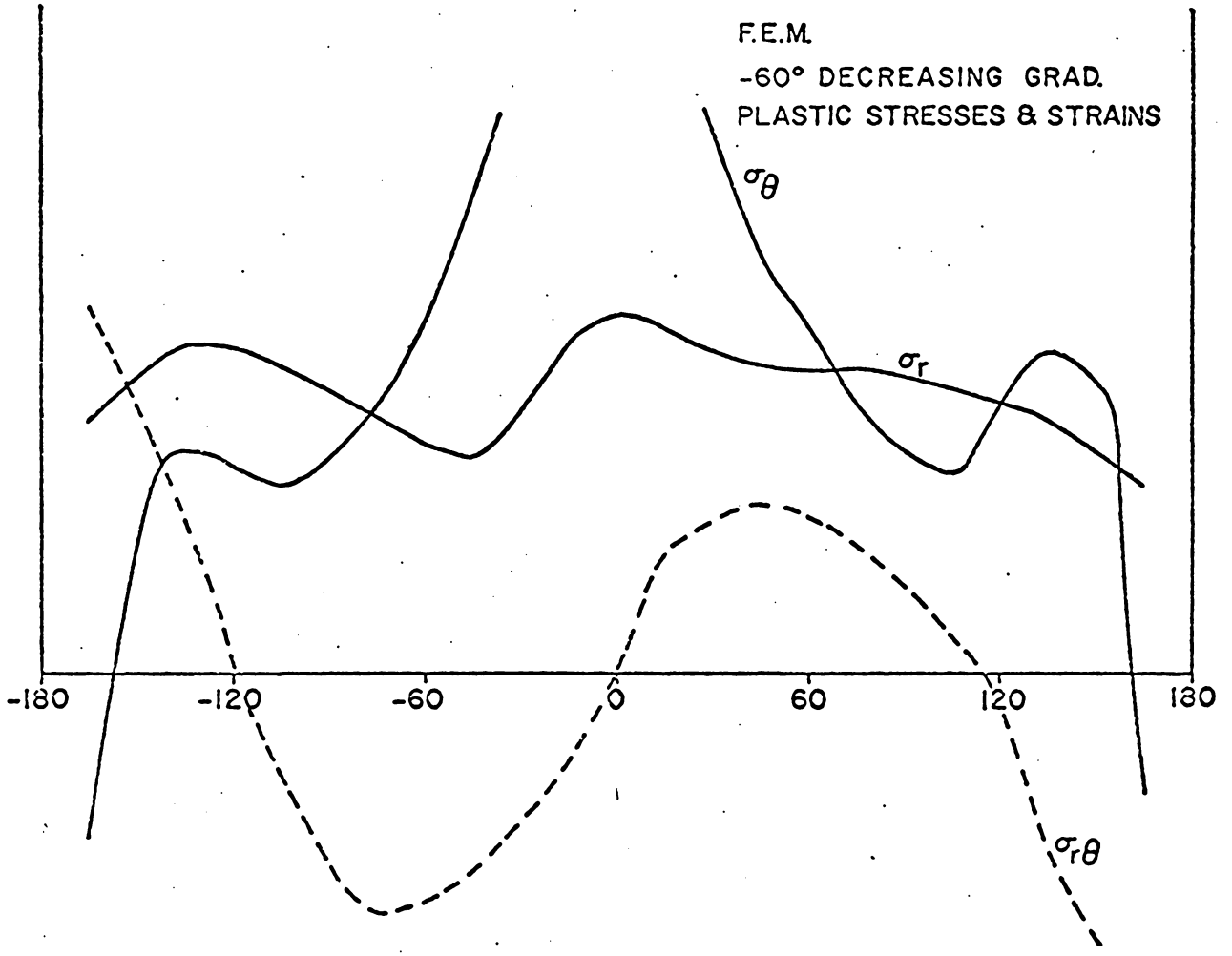

Figure 4-6. -60°; -GRAD, 30.0 ksi (Plastic Stresses).

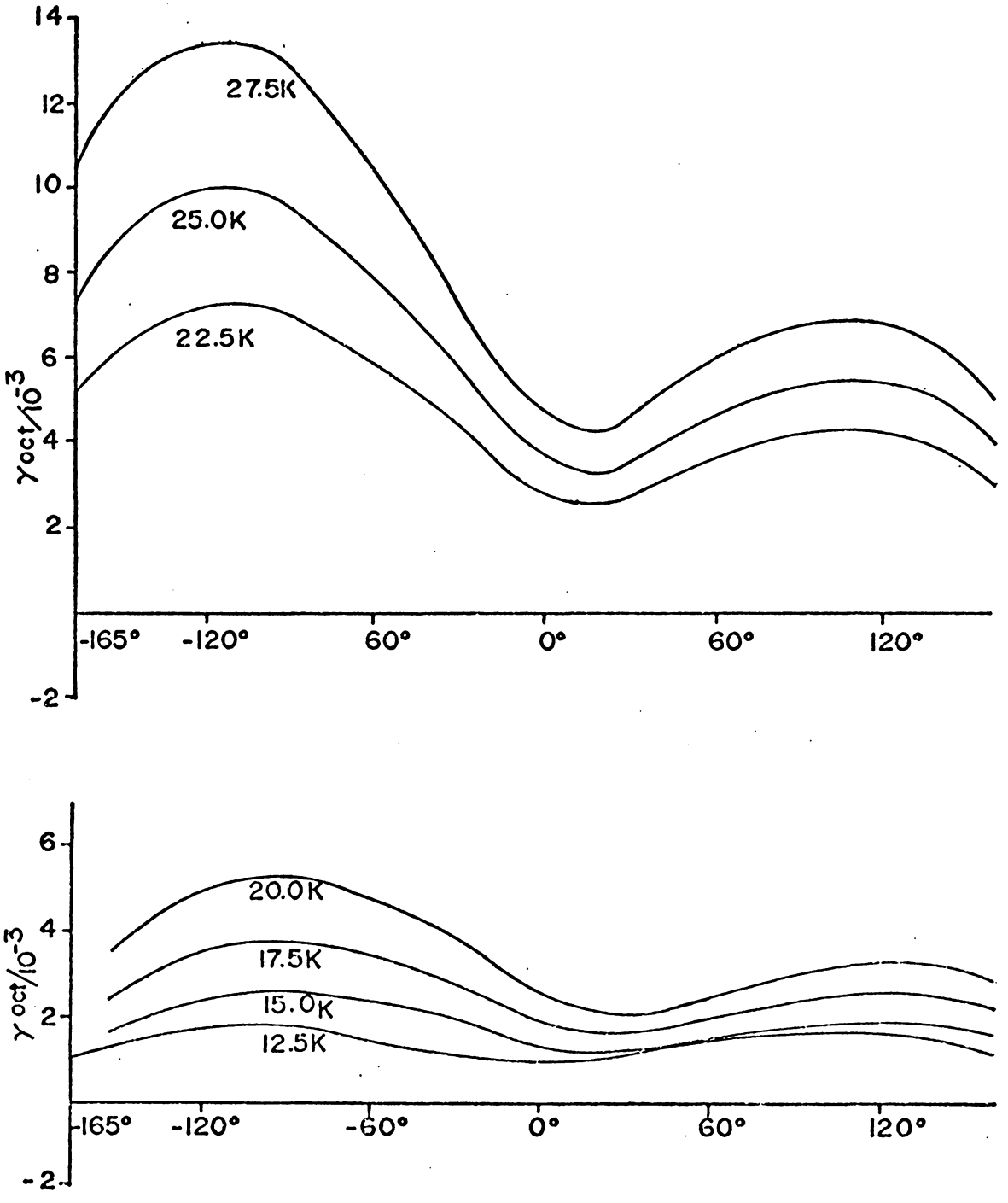

Figure 4-7. -90°; -GRAD, γ_{oct} Distribution.

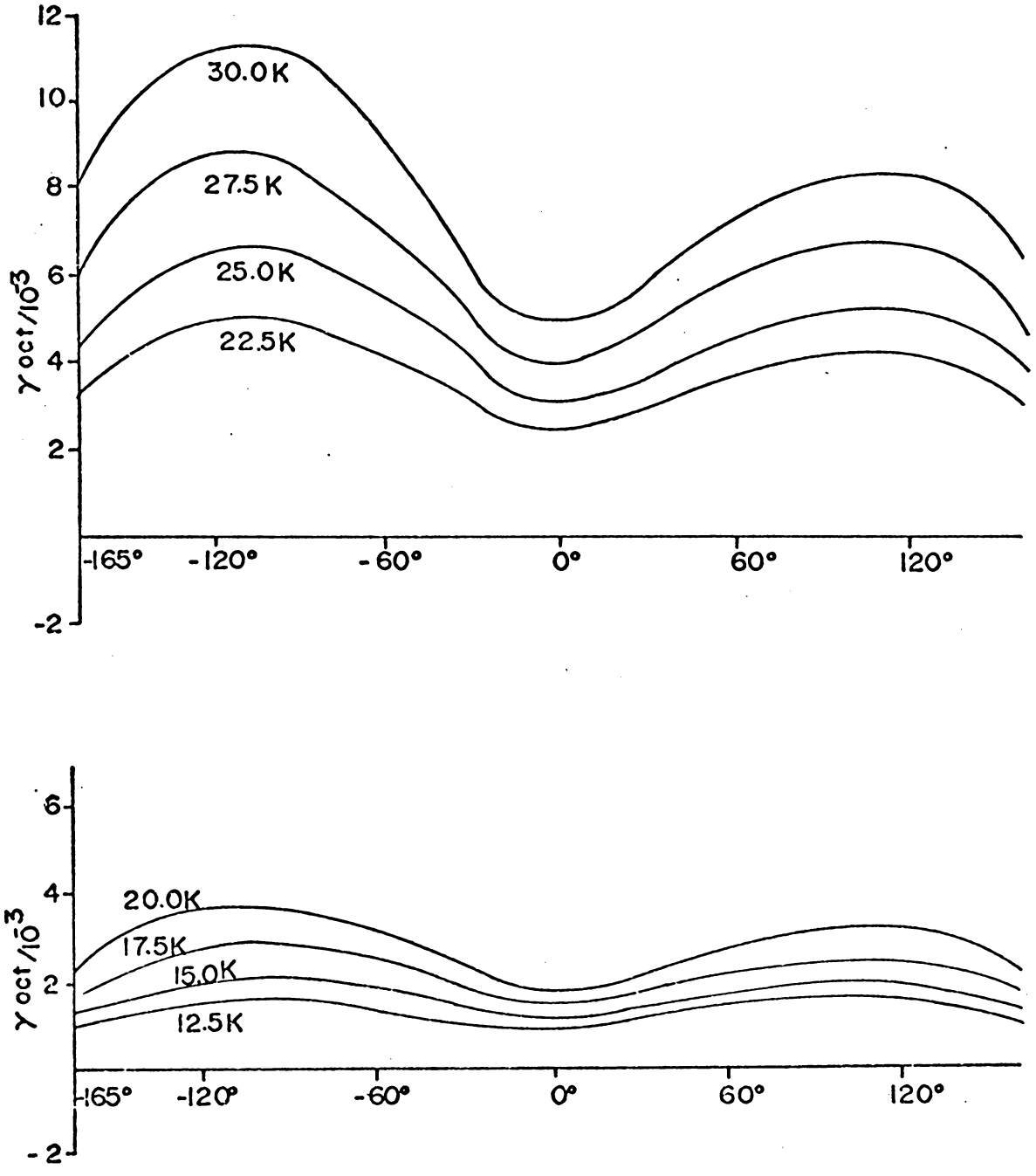

Figure 4-8. -60°; -GRAD, γ_{oct} Distribution.

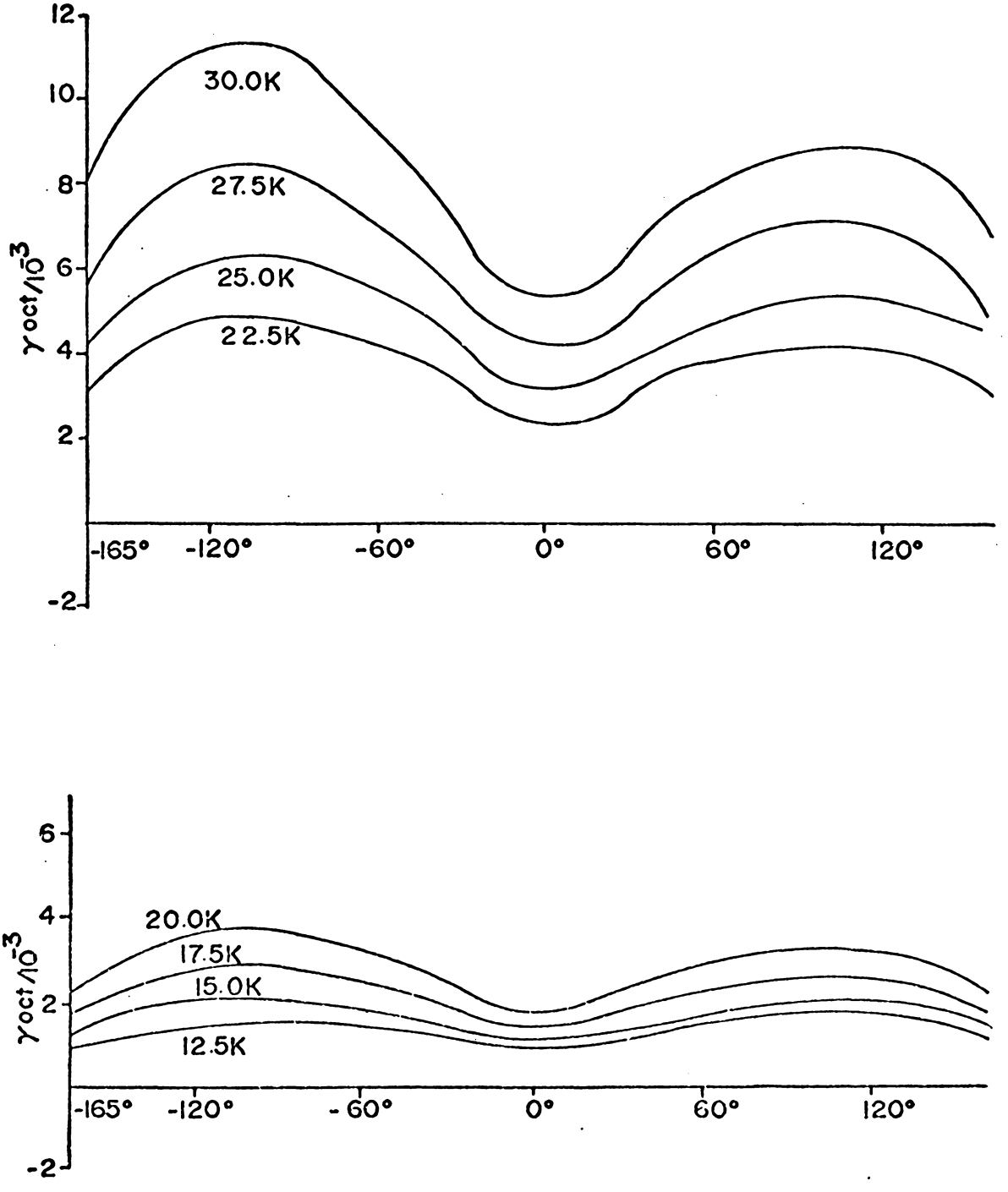

Figure 4-9. -30°; -GRAD, γ_{oct} Distribution.

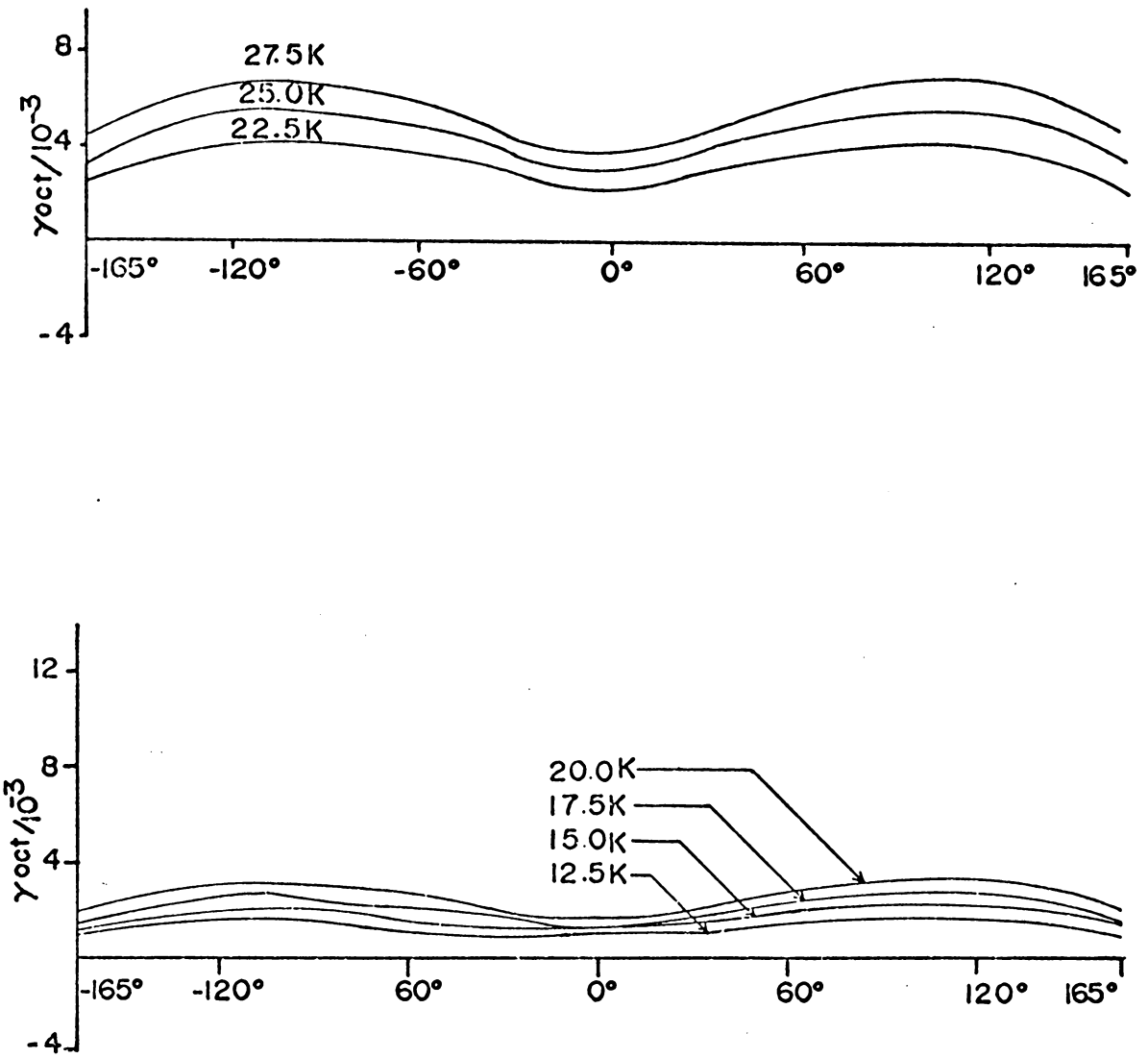

Figure 4-10. 0°; -GRAD, γ_{oct} Distribution.

linear dependence of strains on (increasing) loads. As the angle of gradient is increased from -90° to 0°, the difference between the primary and secondary strain maxima reduced.

In the next set of figures, Figures 4-11 through 4-14, the increasing gradients were considered. Here, again, the maximum strain occurred on the softer material side. Similar characteristics, as described for the decreasing cases, are applicable to the increasing gradient situations.

Figures 4-15 through 4-24 are plots of the elastic-plastic boundaries for different gradients and sequential loads.

Figures 4-15 and 4-16 represent data for a 0° decreasing gradient. Here, there is evidence of a butterfly-shape plastic zone developing with increasing load. The decreasing gradient enhances the plastic zone away from the crack tip. In contrast, Figures 4-17 and 4-18 (0° increasing gradient) show a retardation of growth of the plastic zone, in the gradient direction, for increasing loads.

The growth of the plastic zone was predominantly in the direction of gradient for decreasing gradient cases, as shown in Figures 4-19, 4-20 and 4-21. For the increasing gradients (Figures 4-22, 4-23 and 4-24) the plasticity growth was mainly in the weaker material direction, i.e., away from the gradient direction.

Finite element results for biface materials are presented in Figures 4-25 through 4-28. The deformation field for a crack at an interface (-90° biface) was calculated in Figure 4-25. Across the interface, σ_r shows an erratic behavior, whereas σ_θ is fairly well

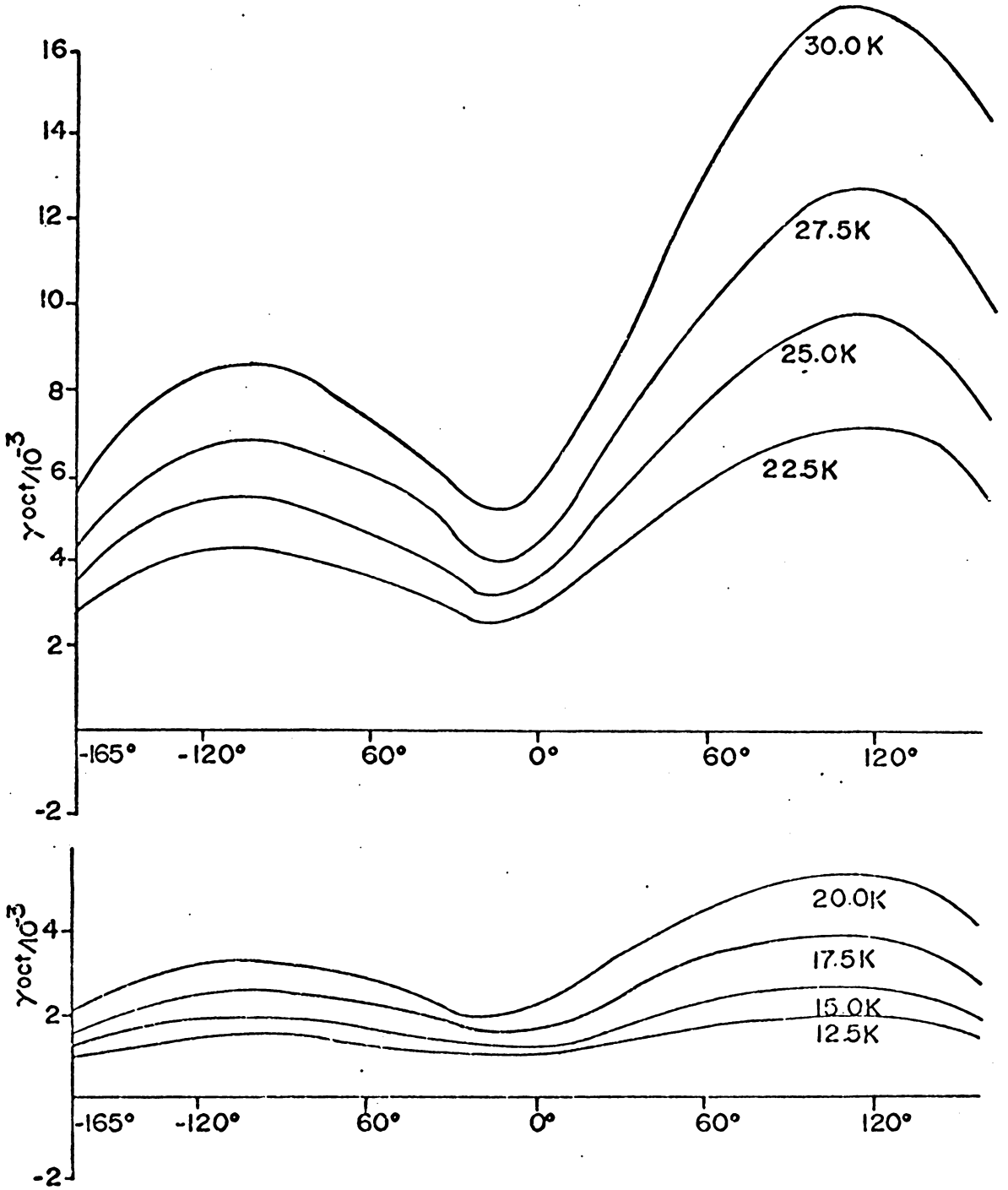

Figure 4-11. -90°; +GRAD, γ_{oct} Distribution.

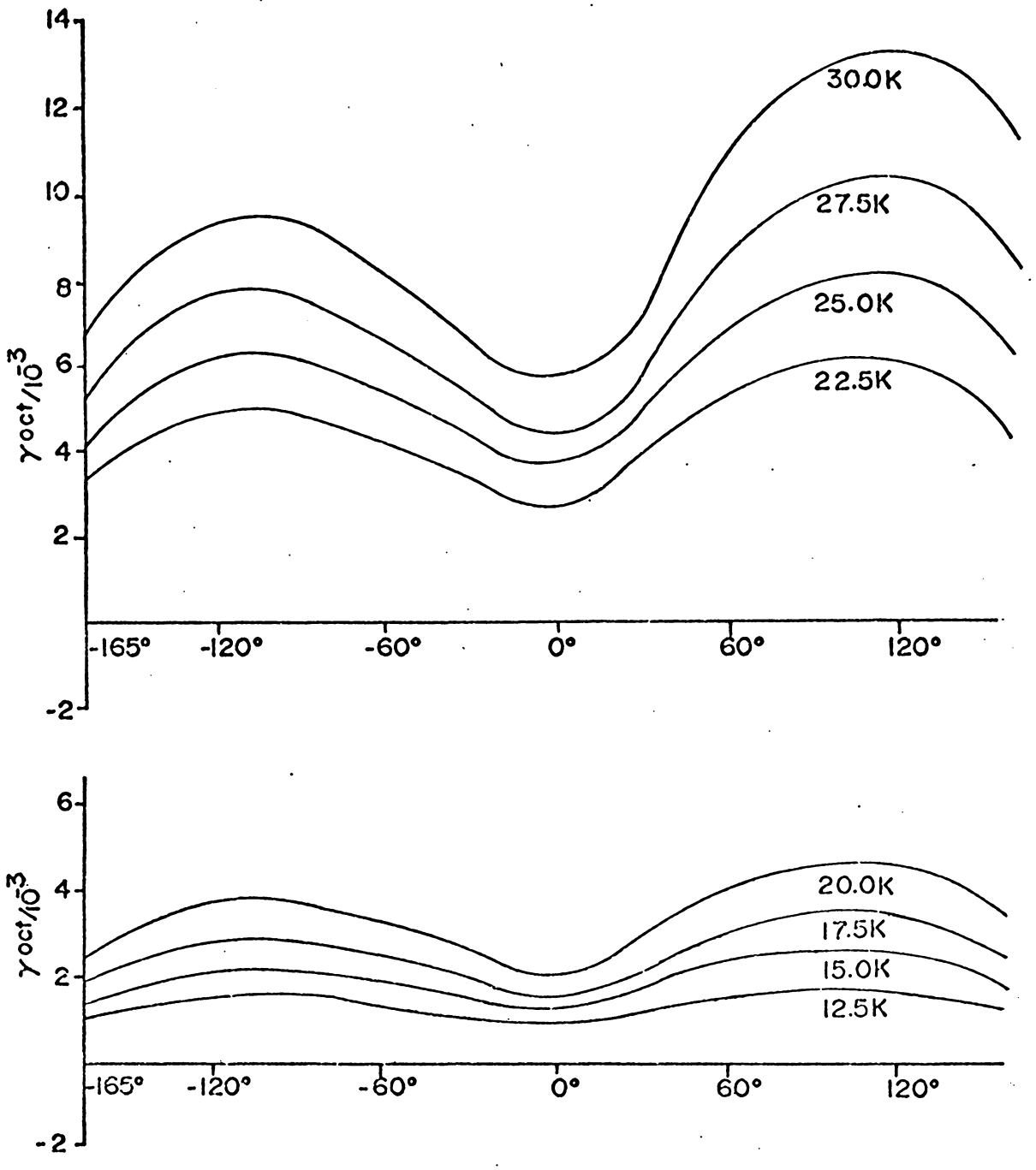

Figure 4-12. -60°; +GRAD, γ_{oct} Distribution.

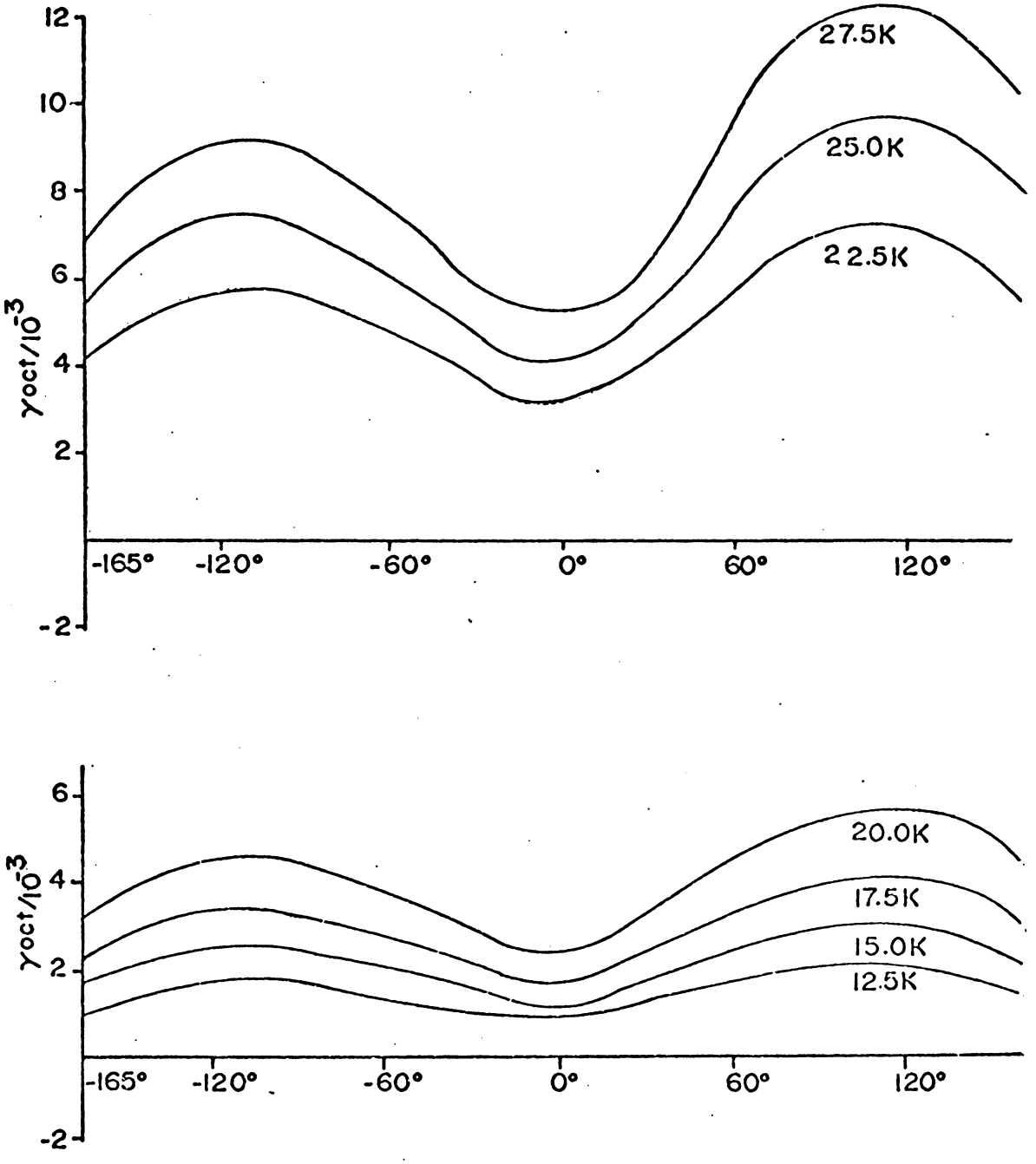

Figure 4-13. -30°; +GRAD, γ_{oct} Distribution.

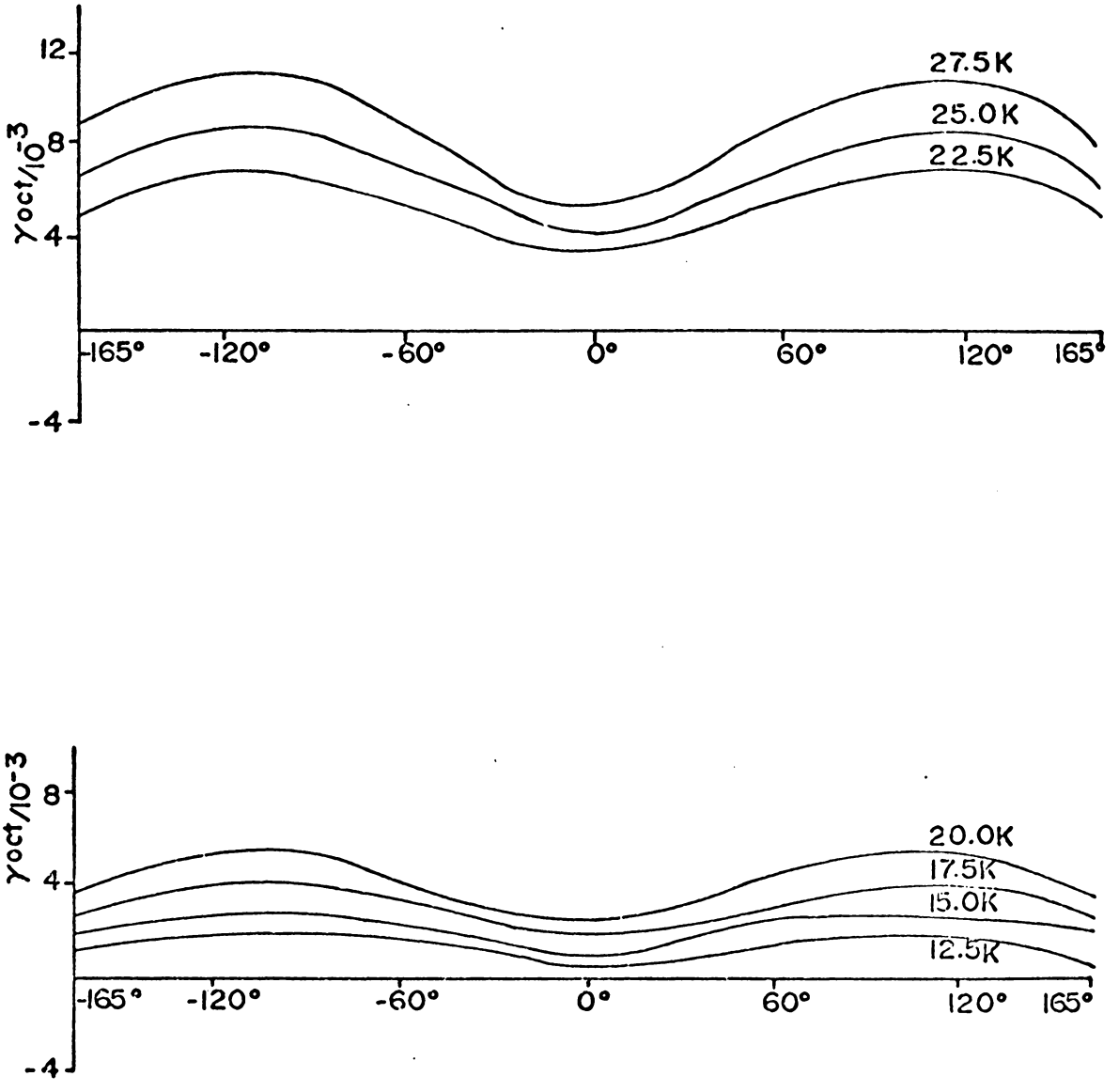

Figure 4-14. 0°; +GRAD, γ_{oct} Distribution.

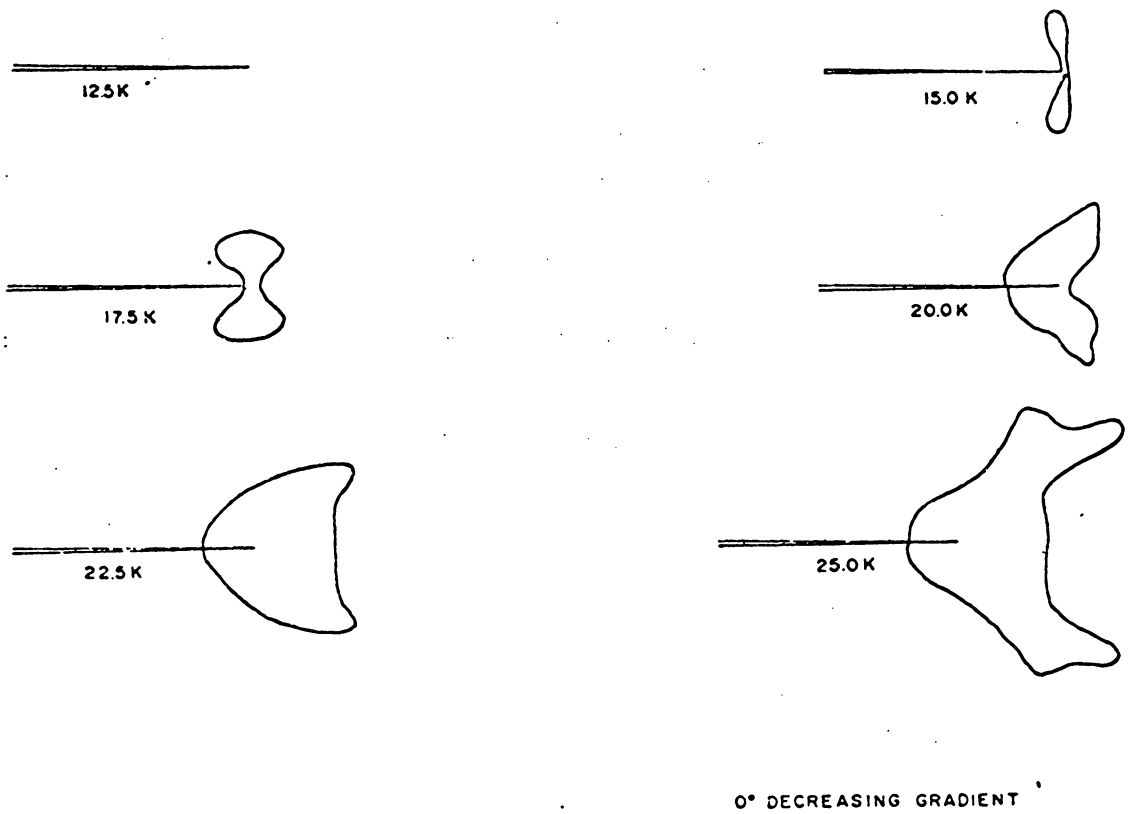

Figure 4-15. 0°; -GRAD, Elastic-Plastic Boundaries.

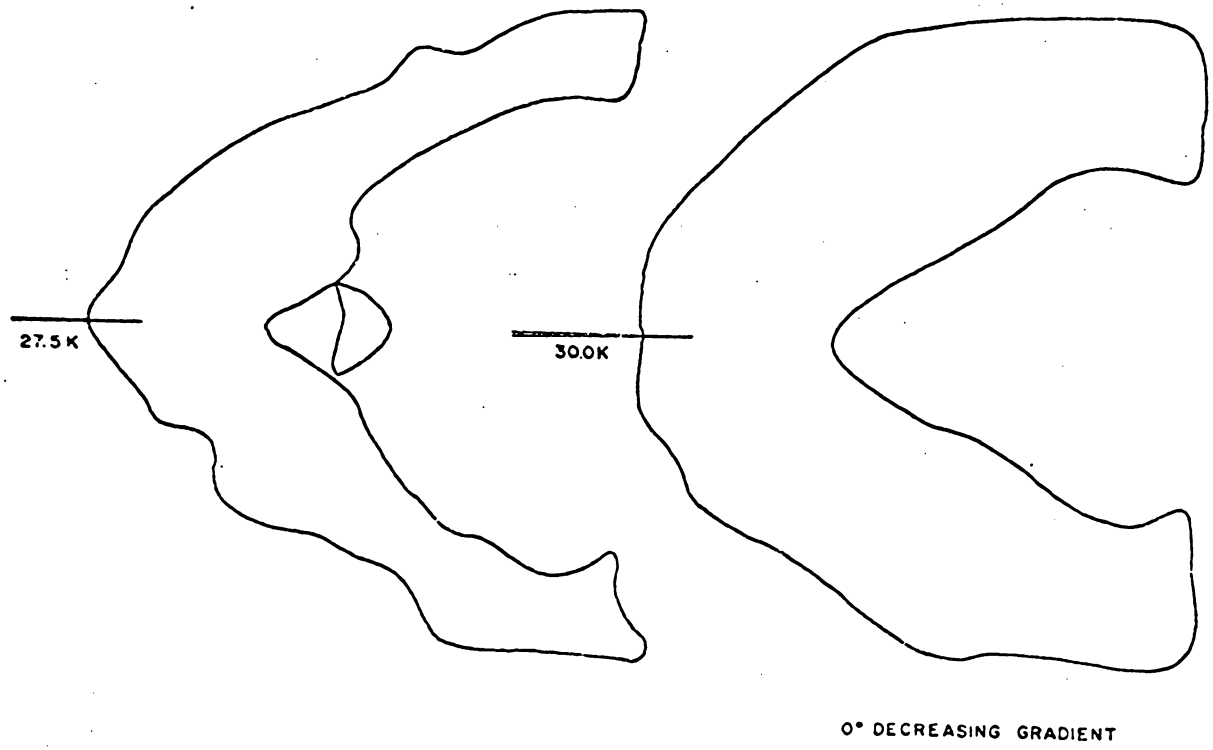

Figure 4-16. 0°; -GRAD, Elastic-Plastic Boundaries.

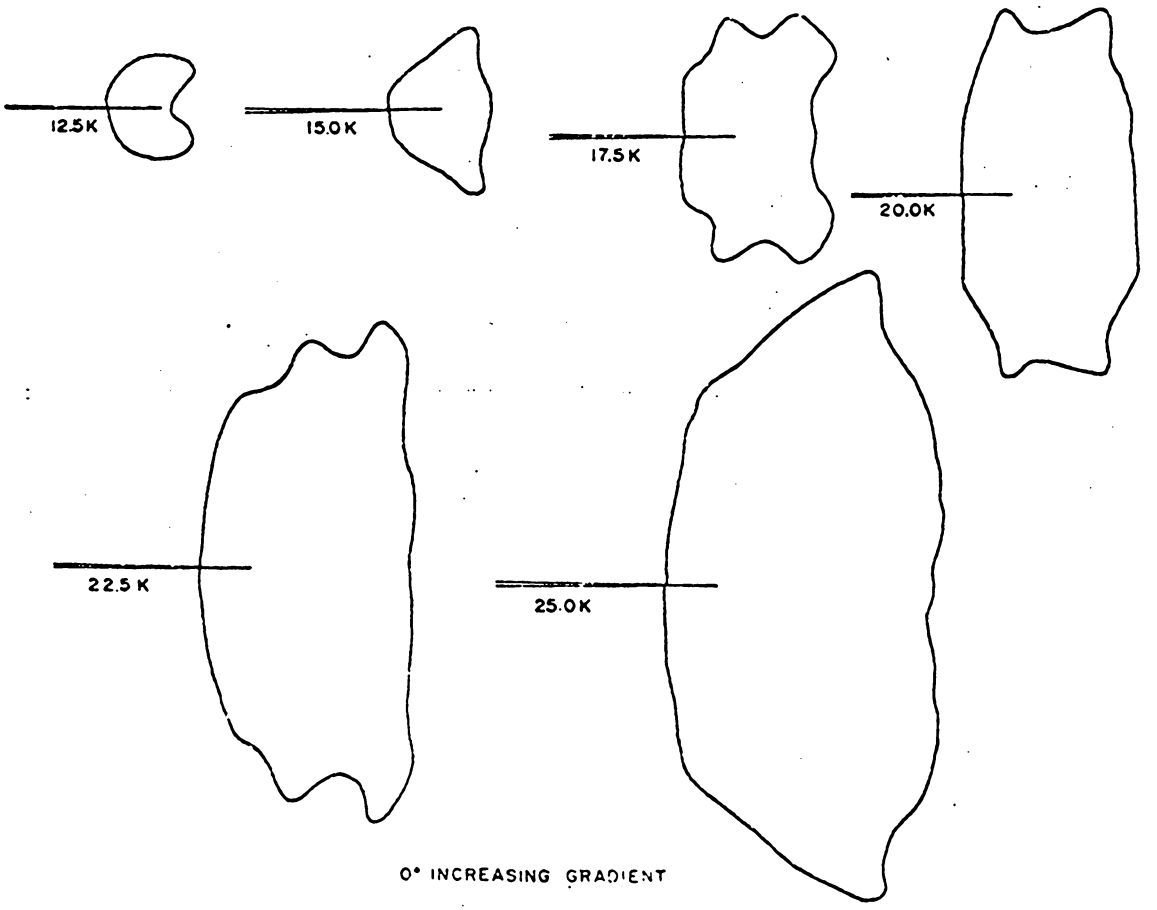

Figure 4-17. 0°; +GRAD, Elastic-Plastic Boundaries.

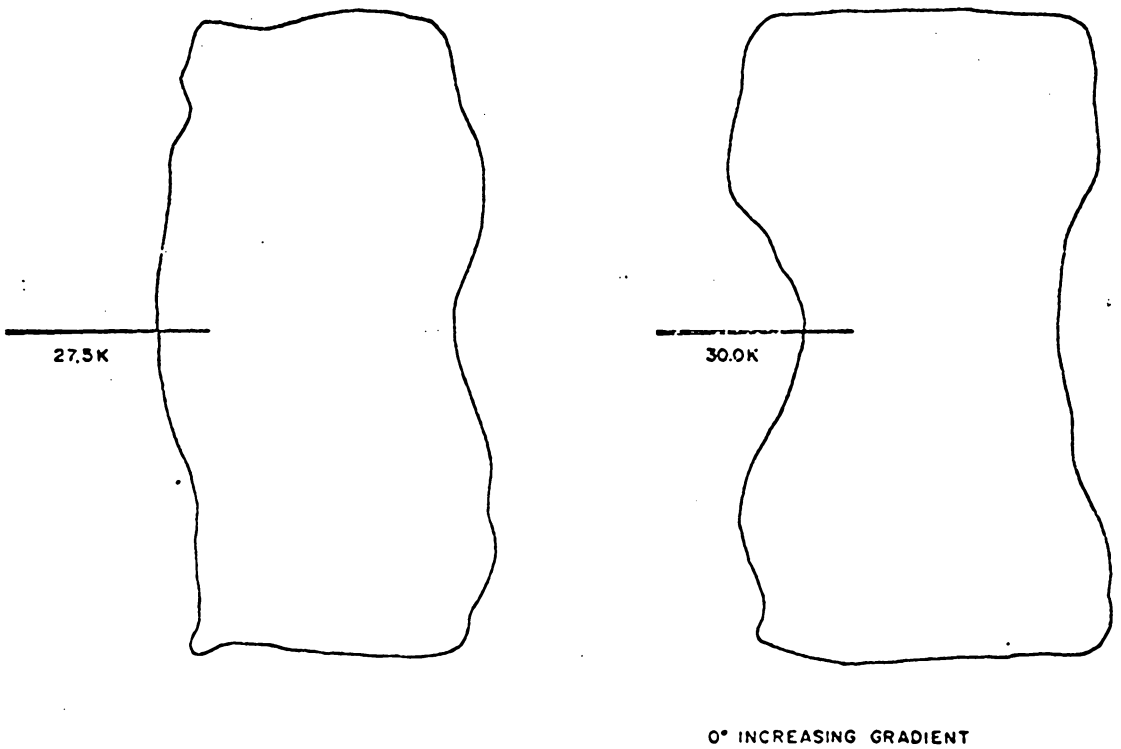

Figure 4-18. 0°; +GRAD, Elastic-Plastic Boundaries.

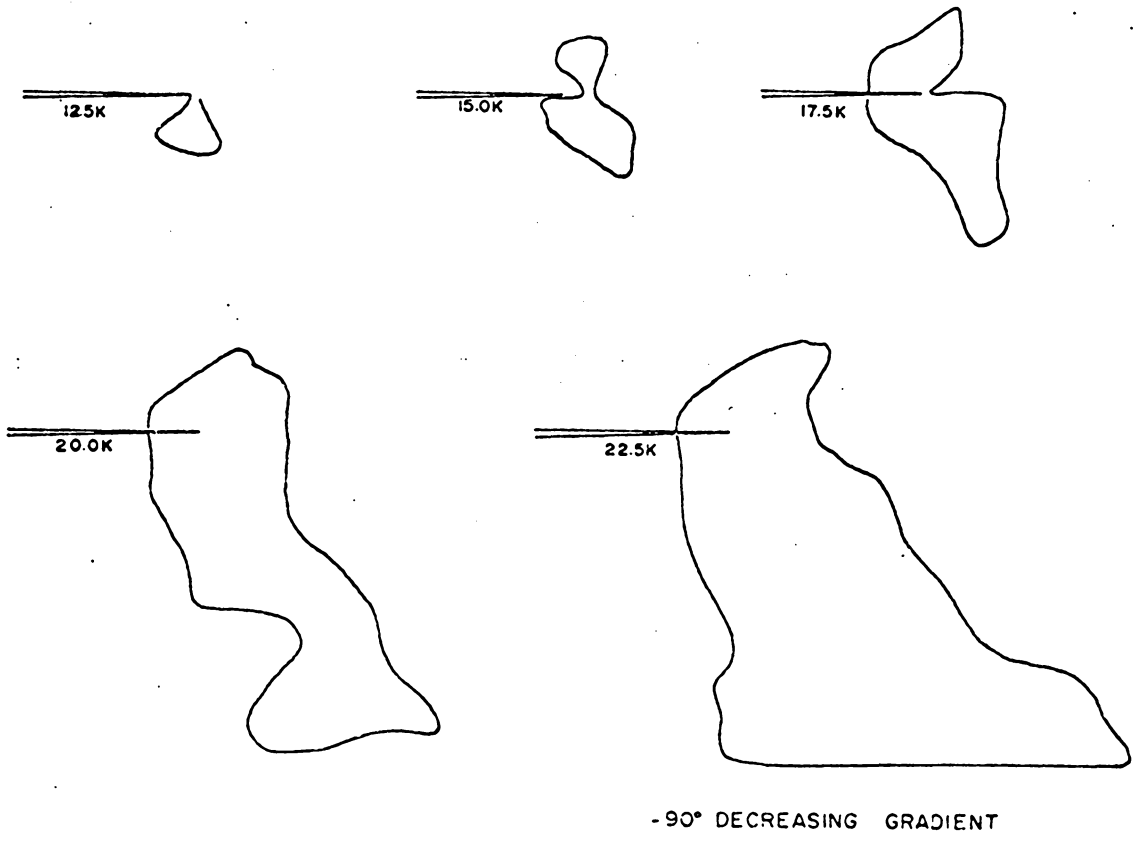

Figure 4-19. -90°; -GRAD, Elastic-Plastic Boundaries.

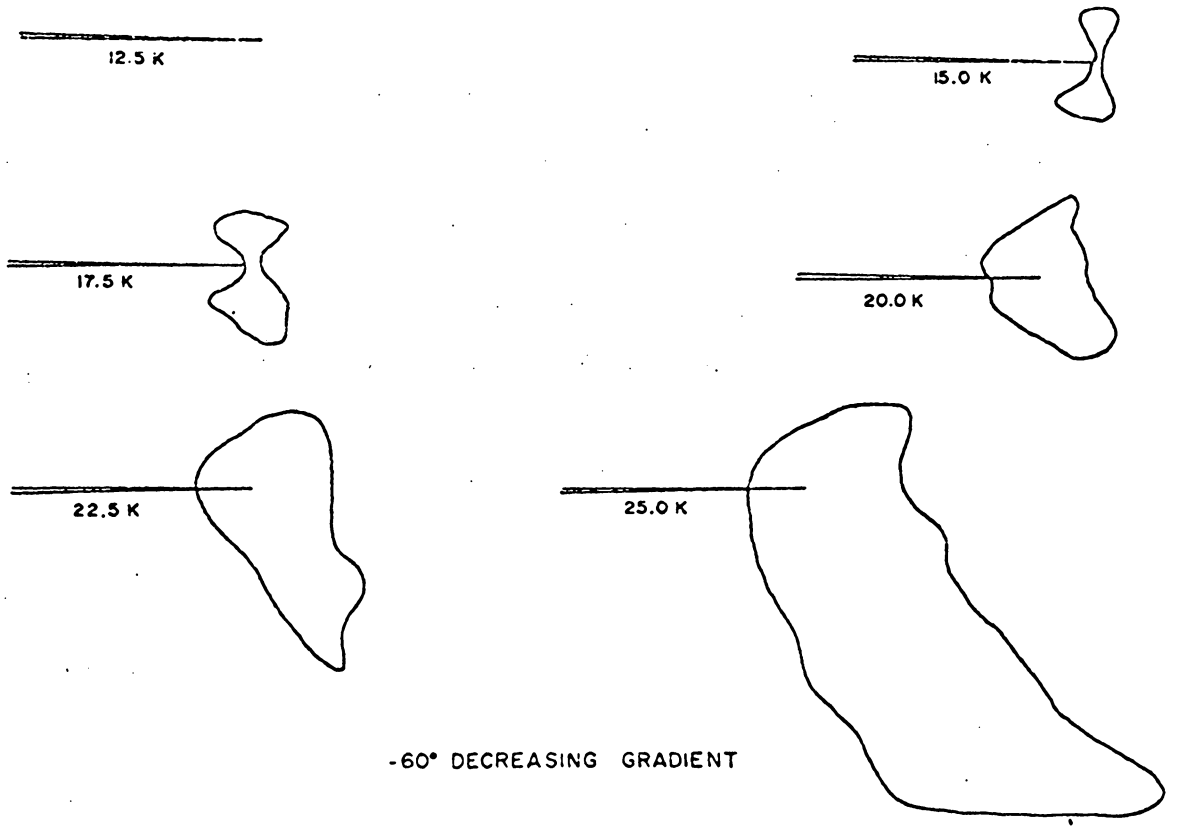

Figure 4-20. -60°; -GRAD, Elastic-Plastic Boundaries.

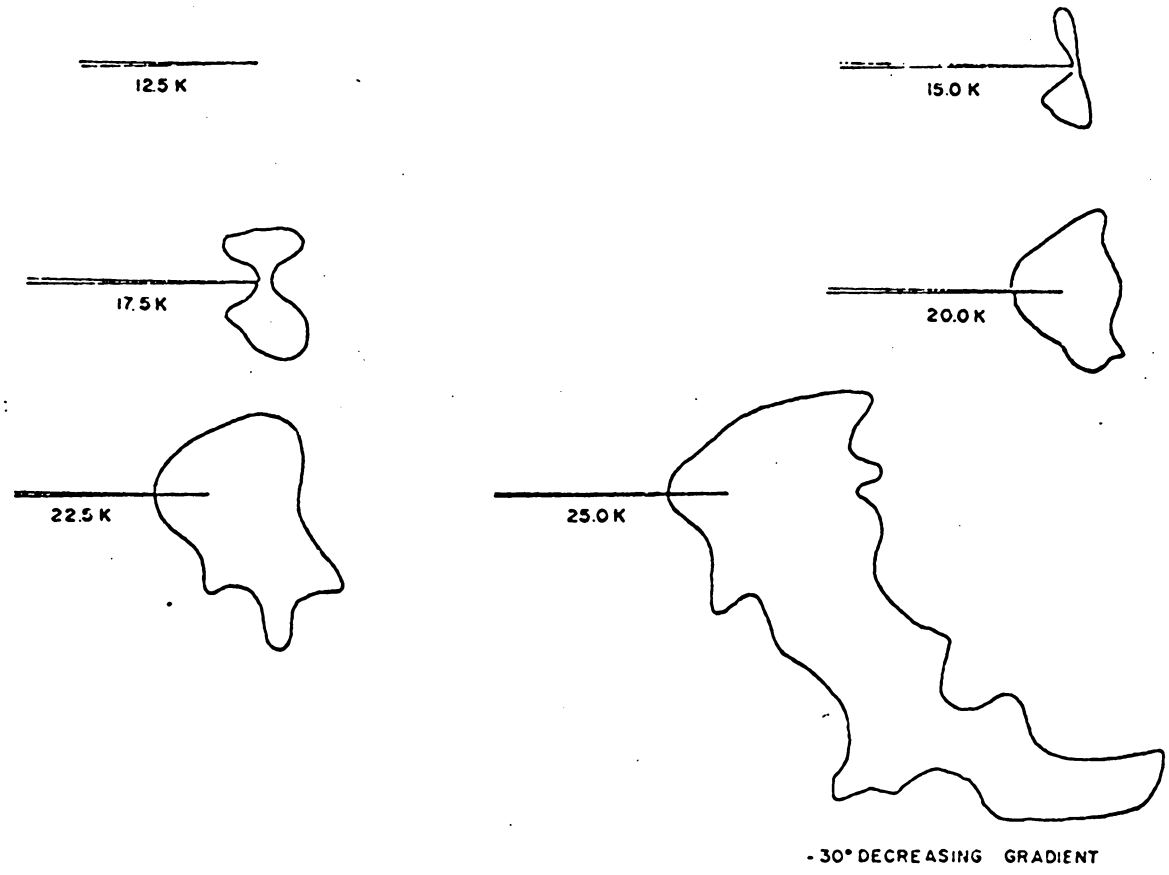

Figure 4-21. -30°; -GRAD, Elastic-Plastic Boundaries.

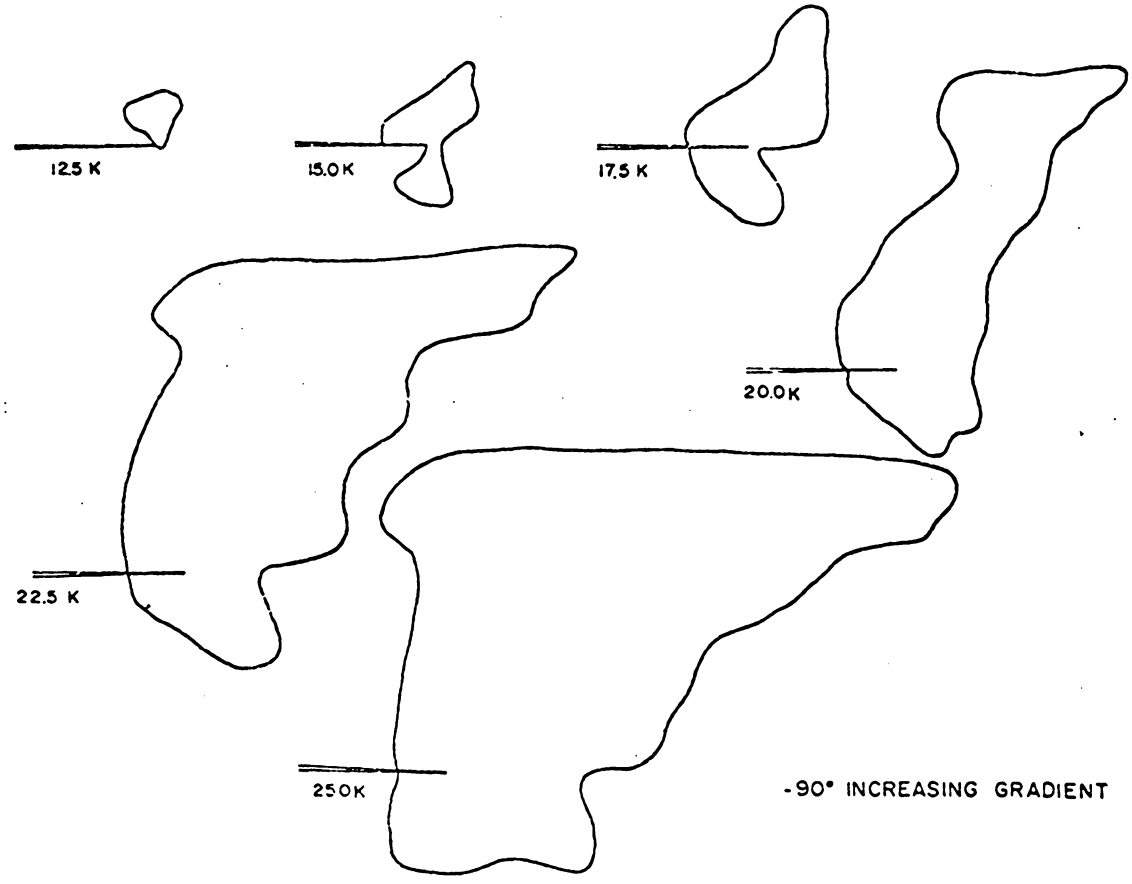

Figure 4-22. -90°; +GRAD, Elastic-Plastic Boundaries.

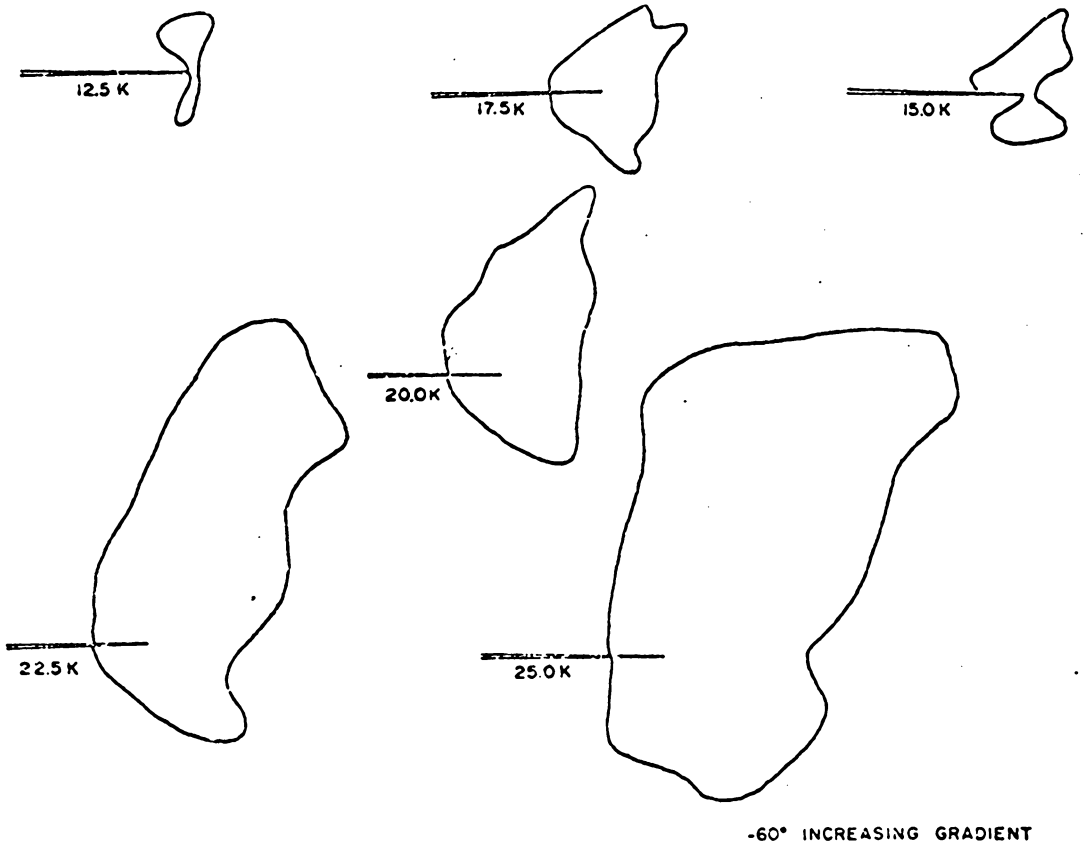

Figure 4-23. -60°; +GRAD, Elastic-Plastic Boundaries.

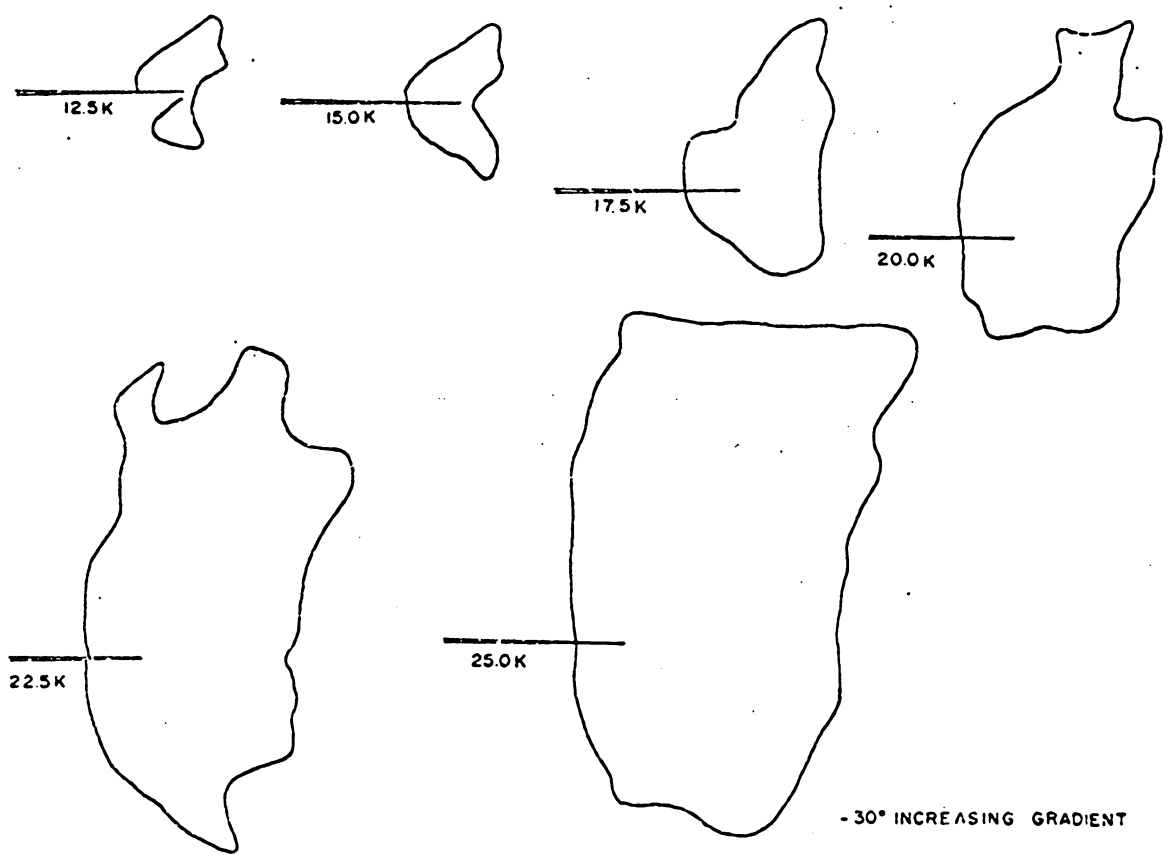

Figure 4-24. -30°; +GRAD, Elastic-Plastic Boundaries.

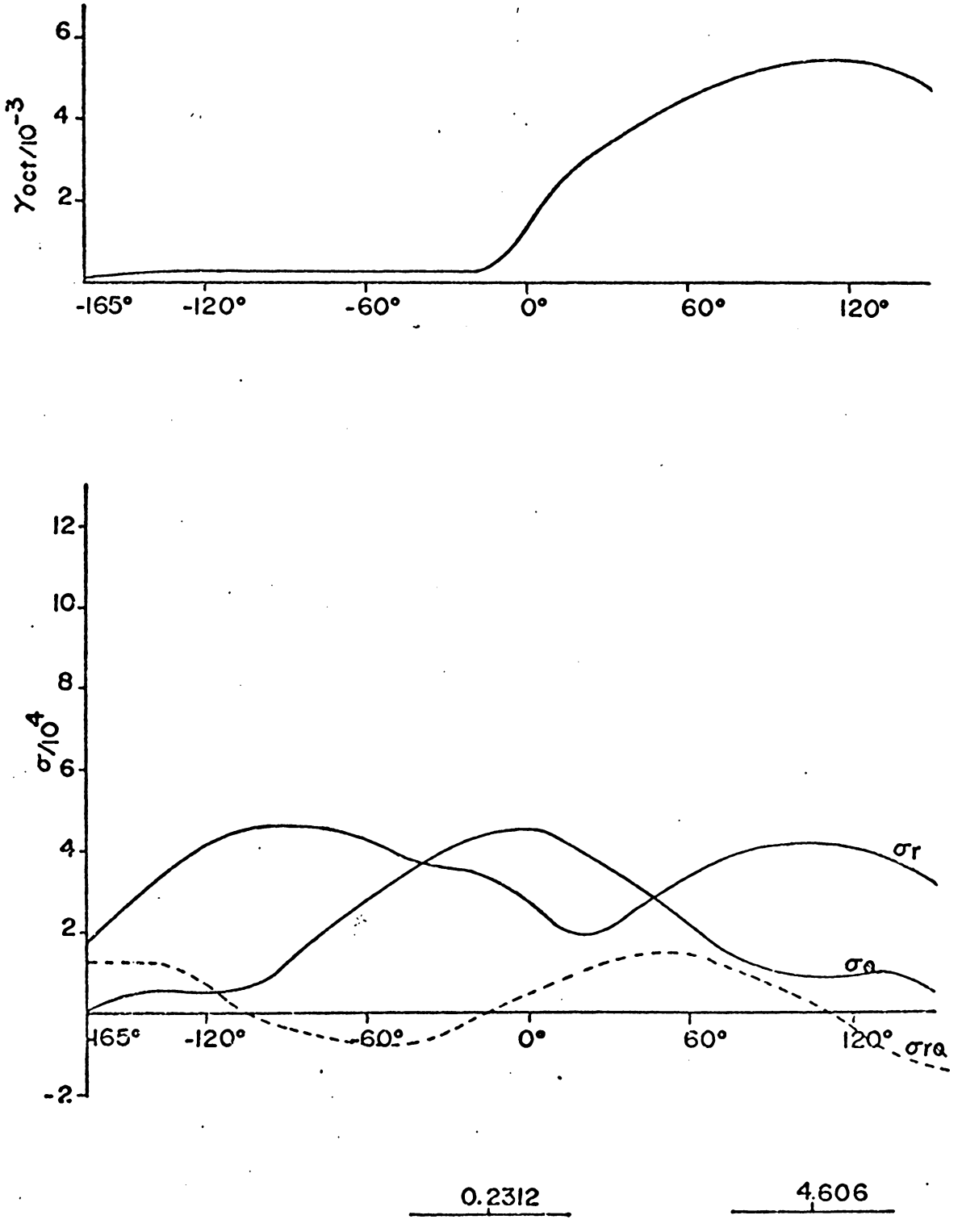

Figure 4-25. -90°; Biface 22.5 ksi; Stresses and Strain Distributions.

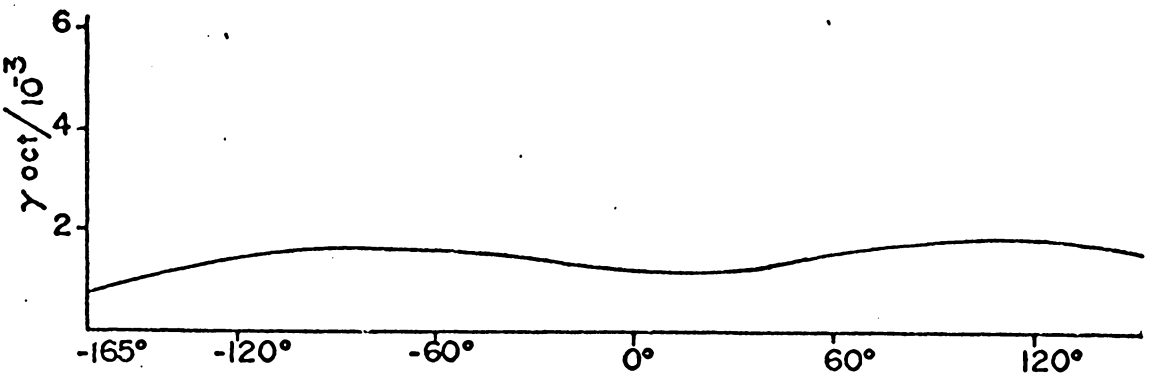

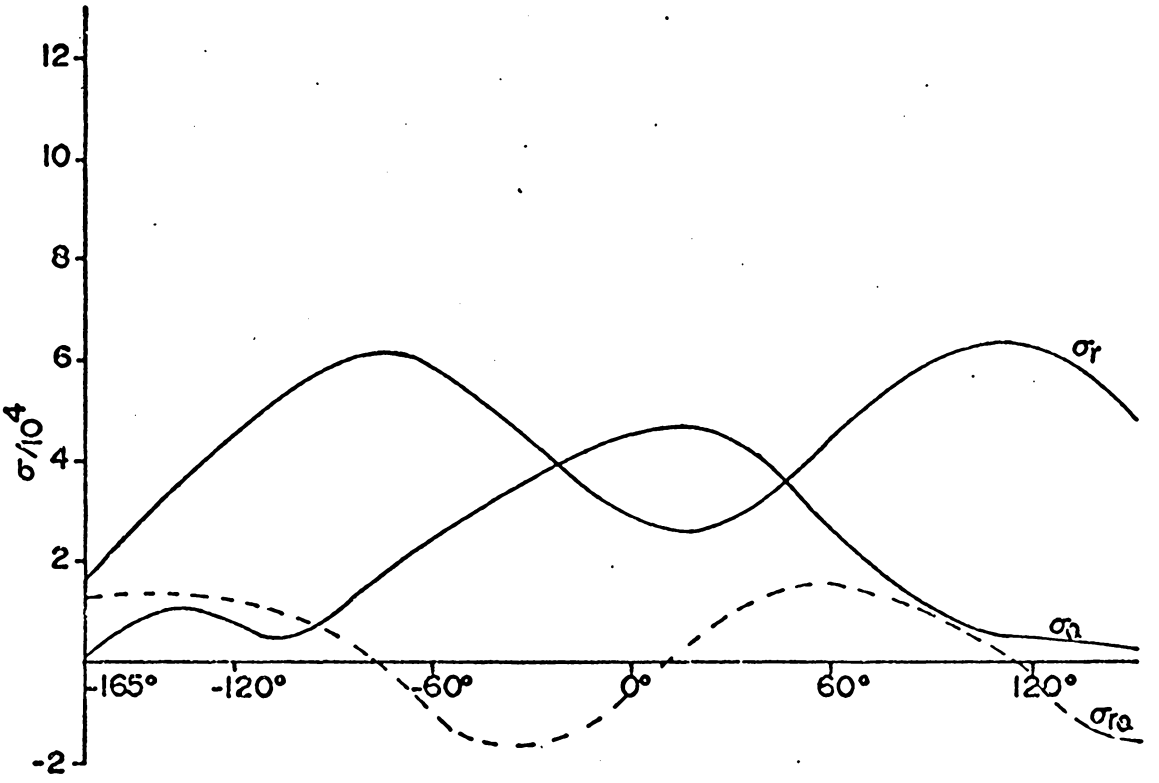

Figure 4-26. -60°; Biface 22.5 ksi; Stresses and Strain Distributions.

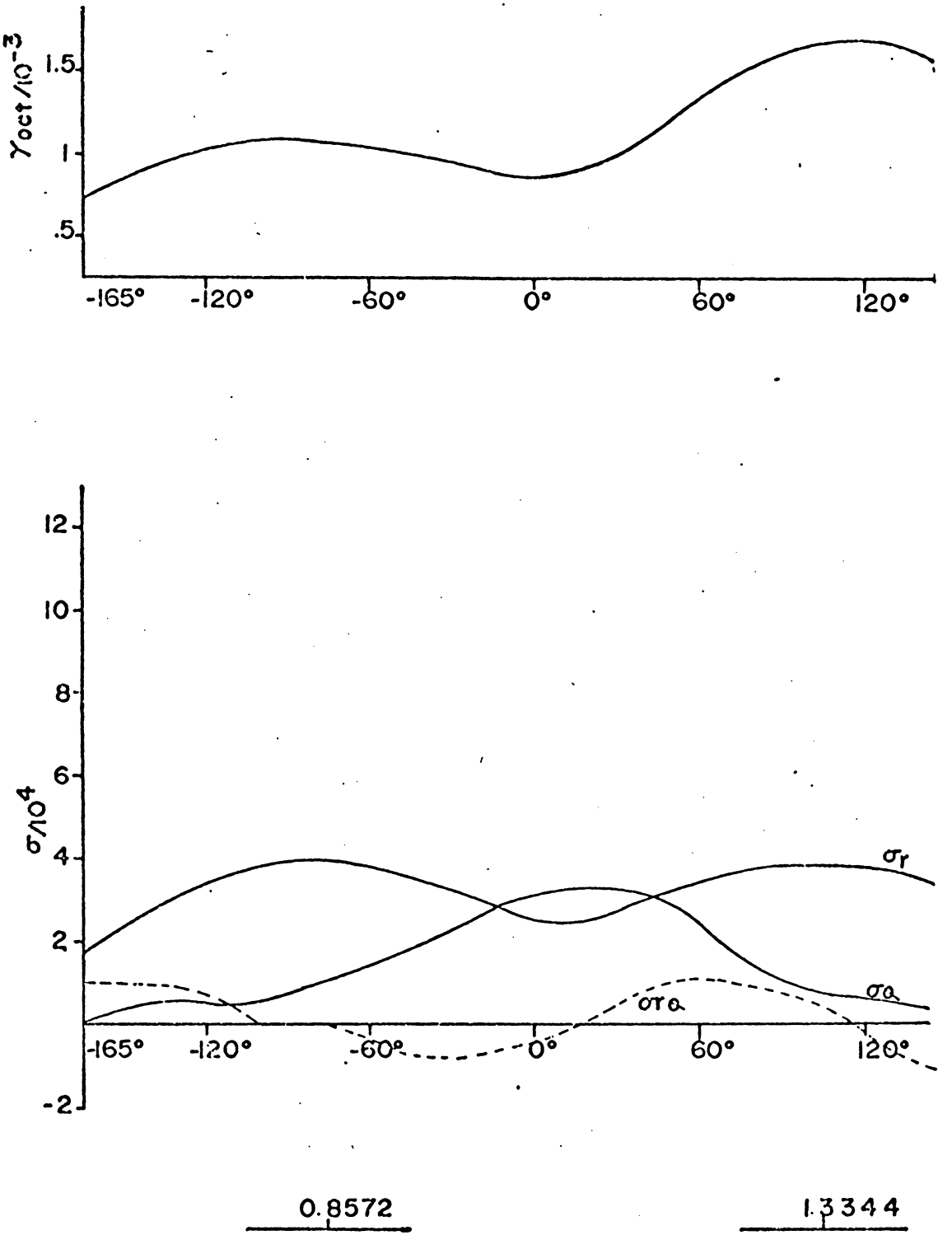

Figure 4-27. -30°; Biface 22.5 ksi; Stresses and Strain Distributions.

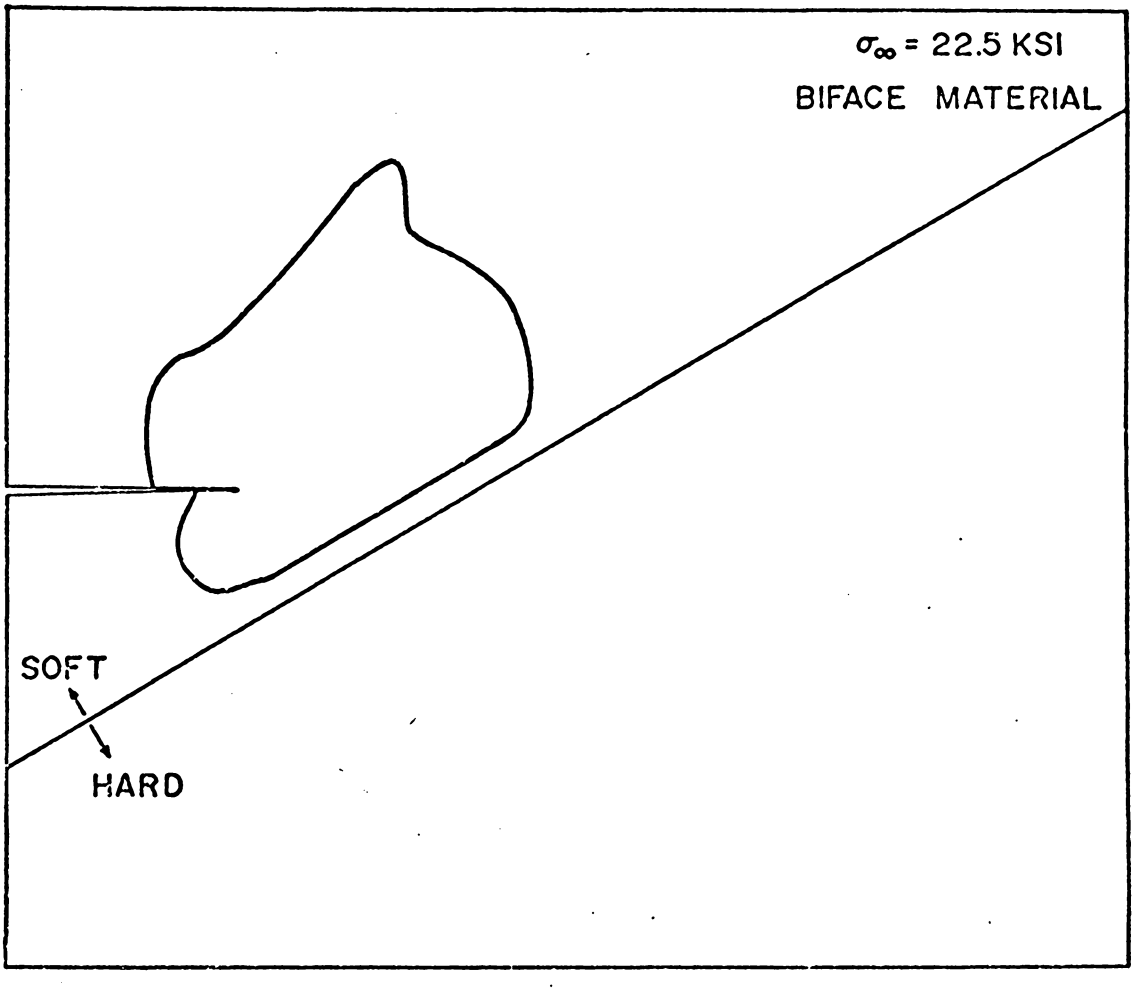

Figure 4-28. -60°; Biface 22.5 ksi; Elastic-Plastic Boundary.

behaved. Low strain values were observed in the hard material side. γ_{oct} peaked out in the +105° direction. Stress and strain distributions for -60° and -30° biface specimens are shown in Figures 4-26 and 4-27. Figure 4-28 is a plot of an elastic-plastic boundary for a -60° biface case.

4.3 DISCUSSION

One of the more interesting aspects of these data is the fact that the highly unsymmetric stress distributions generated by the asymptotic closed form analysis in Chapter II do not appear in the more distant region modeled by the finite element grid. Hence, it might be expected, at this point, that the unsymmetric effects dominate first at the crack tip and spread out to the surrounding region with increasing load. It should be possible to see such an effect experimentally. The stress distributions are influenced somewhat, and the strain energy values in the elements is altered by as much as 15% or so but the overall influence at this level of investigation is not great for the stresses. Figures 4-5 and 4-6 also support the premise that developing plasticity controls the extent of the stress change, and they also show that σ_r is more greatly affected than the other stress components.

The strain distributions and the elastic-plastic boundaries show much more prominent effects as expected for this plane stress analysis. Even for very small loads the deformation fields are unsymmetric for off-axis gradients, and the unsymmetry quickly dominates

the distributions as the applied load is increased.

Figures 4-29 and 4-30 show one other interesting aspect of the data. For both the increasing and decreasing gradient cases there appears to be some type of consistent similarity between the 0° stress distributions and the 60° directions, demonstrated here by σ_r plots for increasing loads. It is possible these tendencies would have some practical consequence such as influencing crack propagation direction at an interface.

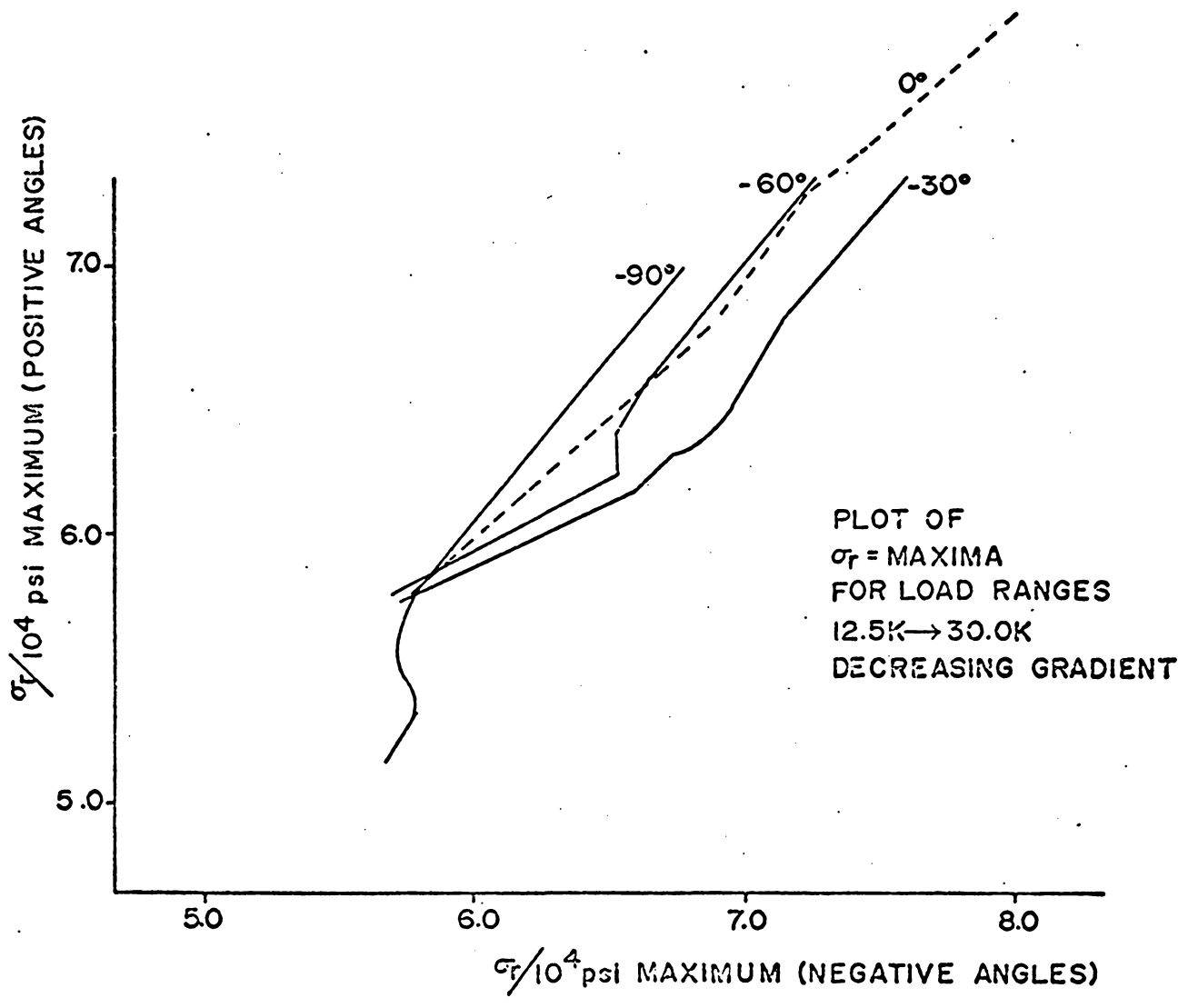

Figure 4-29. -GRAD; Plot of σ_r Maxima.

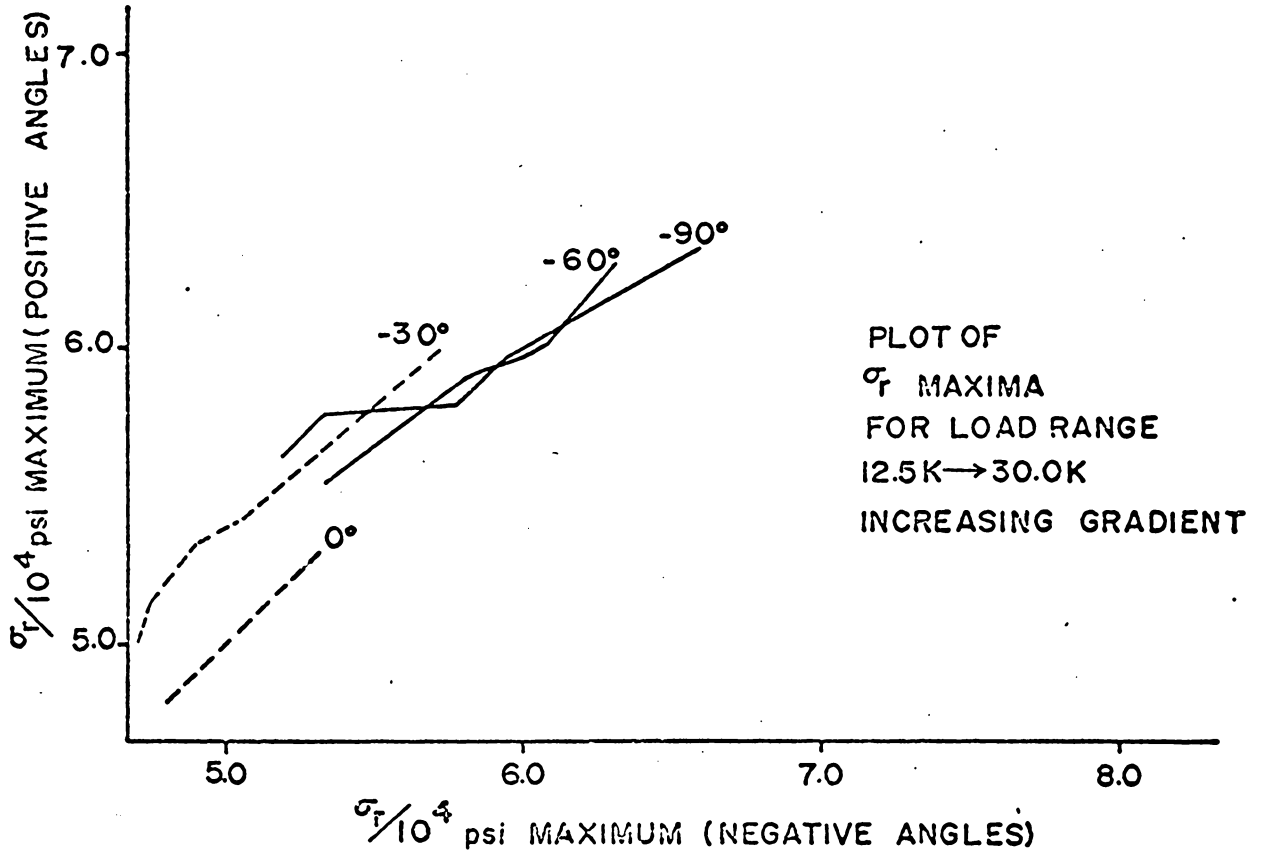

Figure 4-30. +GRAD; Plot of σ_r Maxima.

CHAPTER V

EXPERIMENTAL ANALYSIS

The nature of fracture in defected specimens depends on both the mode of loading and conditions local to the tip of a crack. Successful correlation between experiments and analysis has been mainly for relatively low load conditions.

Solutions to crack problems normally deal with the generation of singular solutions that are symmetric about a crack axis. Experimental evidence shows that crack tip deformation fields in real cases are sometimes far from symmetric. In this chapter, the effects of nonsymmetric deformation patterns in aluminum specimens under Mode I type loading are studied. Nonsymmetric deformations are caused by local material non-uniformities at the crack tip.

5.1 EXPERIMENTAL PROCEDURE

5.11 Purpose

Experimental crack tip deformation patterns were obtained using a light interference technique (Underwood, Swedlow and Kendall [32]). Aluminum specimens were used to give details of the plastic crack tip region. Details obtained by this technique could be interpreted only to within a distance of 0 (10^{-2}) inches from the tip of the crack. Experimental difficulties precluded obtaining data near the fracture loads. All specimens were interpreted as plane

stress and Mode I loading conditions. Preferential directional heat treatment of the specimens was used to obtain local yield strength variations at various angles to the crack axis. The focus of the study was centered on the nonsymmetric development of the deformation patterns with increasing remote load. Unloaded situations were also studied to give an idea of the residual stresses (strains).

5.12 Hardware

The major part of the light interference equipment was previously assembled at the Engineering Science and Mechanics (VPI&SU) research facility. A monochromatic light source with a wave length of λ = 5837A° was used. The fixture included an aircooling system which could be mounted directly on a Unitron microscope. This unit was placed on a saddle, which was positioned on an Instron testing machine. Once on the Instron, the microscope had all three translational degrees of freedom. Magnifications of 54 and 107 were used. At the eye piece of the microscope, a reflex camera was fixed. Plus-X Kodak film was used to record the patterns. To obtain the interference patterns, a lightly silvered optical flat was used on the polished specimen surfaces.

A Rockwell hardness testing machine was used to determine the spatial distribution of hardness. Hardness was then used to determine yield strength values. To obtain a sharp crack, edge notched specimens were fatigued to the desired length on an MTS servo-hydraulic fatigue machine.

5.13 Procedure Details

Various types and sizes of single-edge-notched (SEN) aluminum specimens were tried to obtain the optimum workable specimens. From previous experience, it was noted that thicker specimens were flatter after heat treatment and gave a better polished surface. Also, the load transfer to the specimen was better with increased thickness. Limitations on the thickness of the specimens were placed by constraints of the plane stress assumptions.

Smaller notched specimens (6" x 1" x 1/16") were tried, using standard wedge grips to transfer the load. Even though it was easier to obtain a satisfactory polished surface, it was not possible to obtain the desired heat treatment for these specimens. Also, putting in a fatigue crack was difficult in the narrow specimens.

It was then decided to maintain the size of the specimen (3" x 11" x 1/16"). These specimens were cut and milled from large sheets. At midsection, a 3/8 in. edge notch was sawed in to form the basic SEN specimen. A newly designed grip system provided sufficient load transfer without specimen failure at the grips. Using the thinner specimens (1/16 in.) it was found that, even though uniform heat treatment was possible, the specimens sometimes warped. This created new problems in getting a flat surface. The interference pictures obtained from these specimens were frequently difficult to analyze.

Finally, the specimens were modified, with increased thickness of 0.63 in. along a 1 in. band at the crack axis. Details are shown

in Figure 5-1. With controlled heat treatment, it was then possible to obtain usable flat specimens. 7071-T3, 6061 and 2024 type aluminums were used in the experimental work.

The specimen type described in Figure 5-1 was then carefully heat treated at various prescribed angles at a distance of about 3/8 in. away from the notch tip. Heat treatment was carried out using an oxy-acetelyne flame with part of the specimen submerged in water to effect the prescribed yield strength gradient at chosen angles. After cooling the specimen, strength gradients were established by hardness measurements.

Hardness measurements along gradient lines were taken. Using a relation between hardness and yield strength, strength gradients were established. Increasing penetration of the hardness measuring ball meant decreasing strength in the direction under consideration. Similarly, increasing strength gradients were obtained. The sketch below indicates a typical hardness gradient.

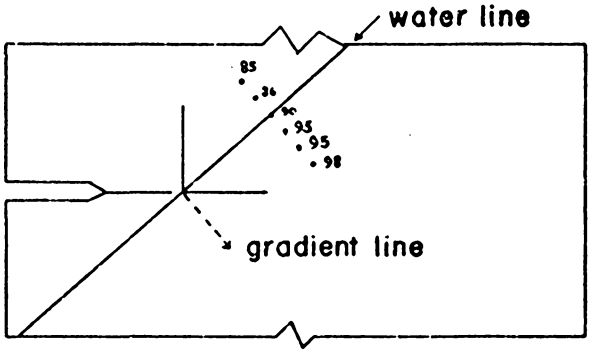

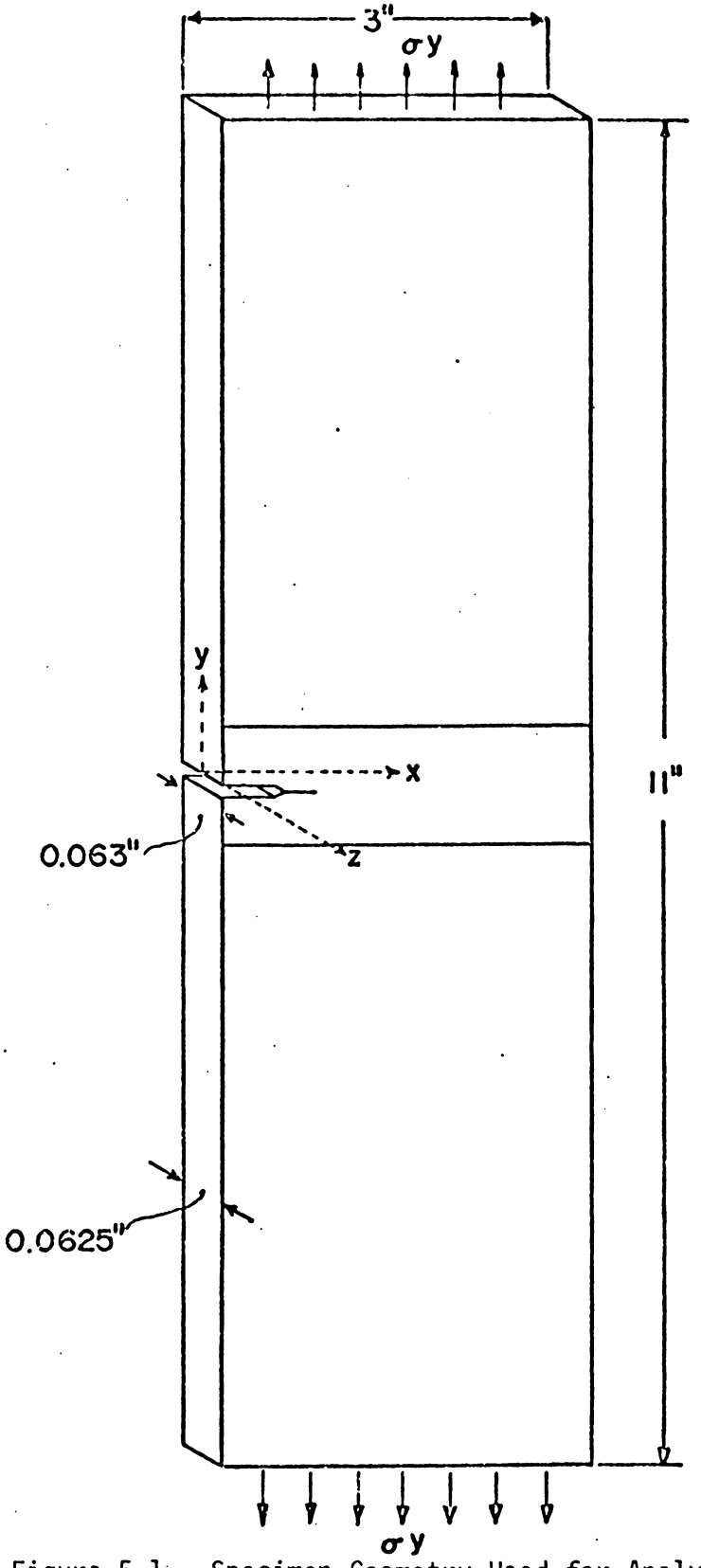

Figure 5-1. Specimen Geometry Used for Analysis.

Next the specimens were polished on the rasied specimen surface, which included the notch area. Polishing difficulties were experienced with the softer specimens. Harder material specimens provided increasingly better polished surfaces with continued polishing. In the softer ones, hard material particles from the specimen ploughed through and scratched the polished surfaces. For polishing, a very flat work table was used. Starting with a flat specimen, it was first sanded with no. 600 grit paper. For finer polishing, a microcloth was mounted on a horizontal rotating wheel electrically operated. The microcloth was then coated with a slurry of 1μ AlO_2 (aluminum oxide). After about 100 revolutions of the wheel, the specimen was rotated and polished for yet another 100 revolutions. The specimen was held to the wheel by a flat steel mount which, in turn, was held by hand. The above mentioned procedure was then used with a slurry of 0.3μ AlO_2. In this manner, a very good flat reflecting surface was obtained.

The specimen was then mounted on an MTS fatigue machine to generate a sharp crack. Working at 20 cps, a fatigue crack was propagated in from the notch tip. for a distance of approximately 3/8 in. This distance was suitably varied, in order to place the final crack tip at the center of the strength gradient in each specimen. Fatigue cracks propagated along the crack axis. The effect of mild gradients on the fatigue crack growth direction did not seem to be significant. However, there were noticeable effects of the gradients on the rate of propagation of the fatigue cracks. It was not possible to

categorize the exact effects on the rates of fatigue crack propagation, due to poorly defined gradients in this area of interest. The fatiguing process also relieved some of the residual stress fields generated by heat treatment.

Next, the specimen was mounted on an Instron testing machine, to load in tension and obtain the interference patterns. Loading on the Instron was done at a rate of 0.02 in. per minute. Initial estimates of failure loads were calculated using existing values of K_{IC}. Just before failure, the specimens were unloaded. The unloaded interference patterns were used to determine the residual deformation field. At near-failure loads, the interference patterns could not be obtained due to excess straining at the crack tip. Photographs of the specimen surface at the crack tip were then taken up to the inception of crack growth.

There was some difficulty in obtaining a uniform source of light on the specimen. This partly affected the quality of the pictures taken. Exposures of 1/4 sec. and 1/2 sec. were used.

Remarkable developments of nonsymmetric singularities were noticed. With further sophistication and better equipment, it is conjectured that the nonsymmetric phenomenon could be photographed with a movie camera.

5-2 EXPERIMENTAL RESULTS

The geometry of the specimens used in the present investigation is described in Figure 5-1.

Figure 5-2 is a light interference pattern showing the out-of-plane strain, ε_z, contours around the crack tip when the specimen was loaded symmetrically. The material properties vary at an angle from the crack tip. The nonsymmetry of the development of the singularity is very evident.

Figures 5-3 through 5-5 are the results of some of the analyzed light interference pictures for various strength gradients and loads. The plots are ε_z-strain distributions (given in terms of fringe order) around the crack tip, that is,

$$\varepsilon_z = \frac{\lambda n}{t}$$

where λ = wave length

t = thickness of specimen

n = fringe order.

In other words, given λ and t, ε_z is directly proportional to n. Figure 5-3 indicates the ε_z variations for a loading sequence, with a moderate decreasing gradient in the +55° direction. In this case a high magnification picture was analyzed. A + 65° decreasing gradient low magnification picture was analyzed in Figure 5-4; figures 5-3 and 5-4 represent data from 2024-T3 aluminum specimens. The data in Figures 5-5 and 5-6 were produced by 6061 aluminum specimens. At a low magnification, a -62° increasing gradient ε_z distribution, for a remote load of 9333.3 psi is shown in Figure 5-5. For a sequence of load values, with a -67° increasing gradient, the development of unsymmetric singularities is indicated in Figure 5-6.

Gradient directions and the crack propagation directions for a set of specimens are shown in Figures 5-7 through 5-9. Figure 5-7a

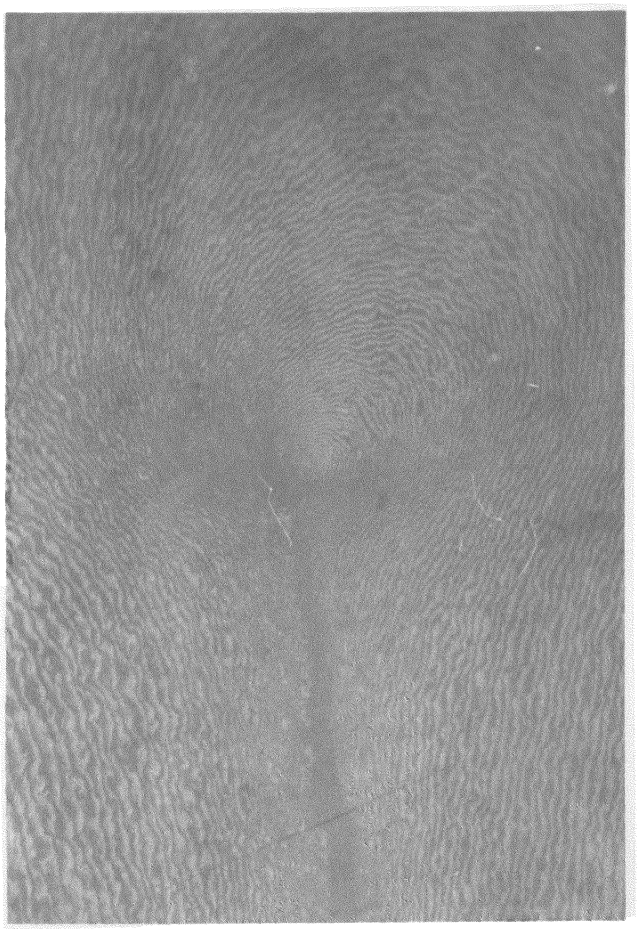

Figure 5-2. Light Interference Picture.

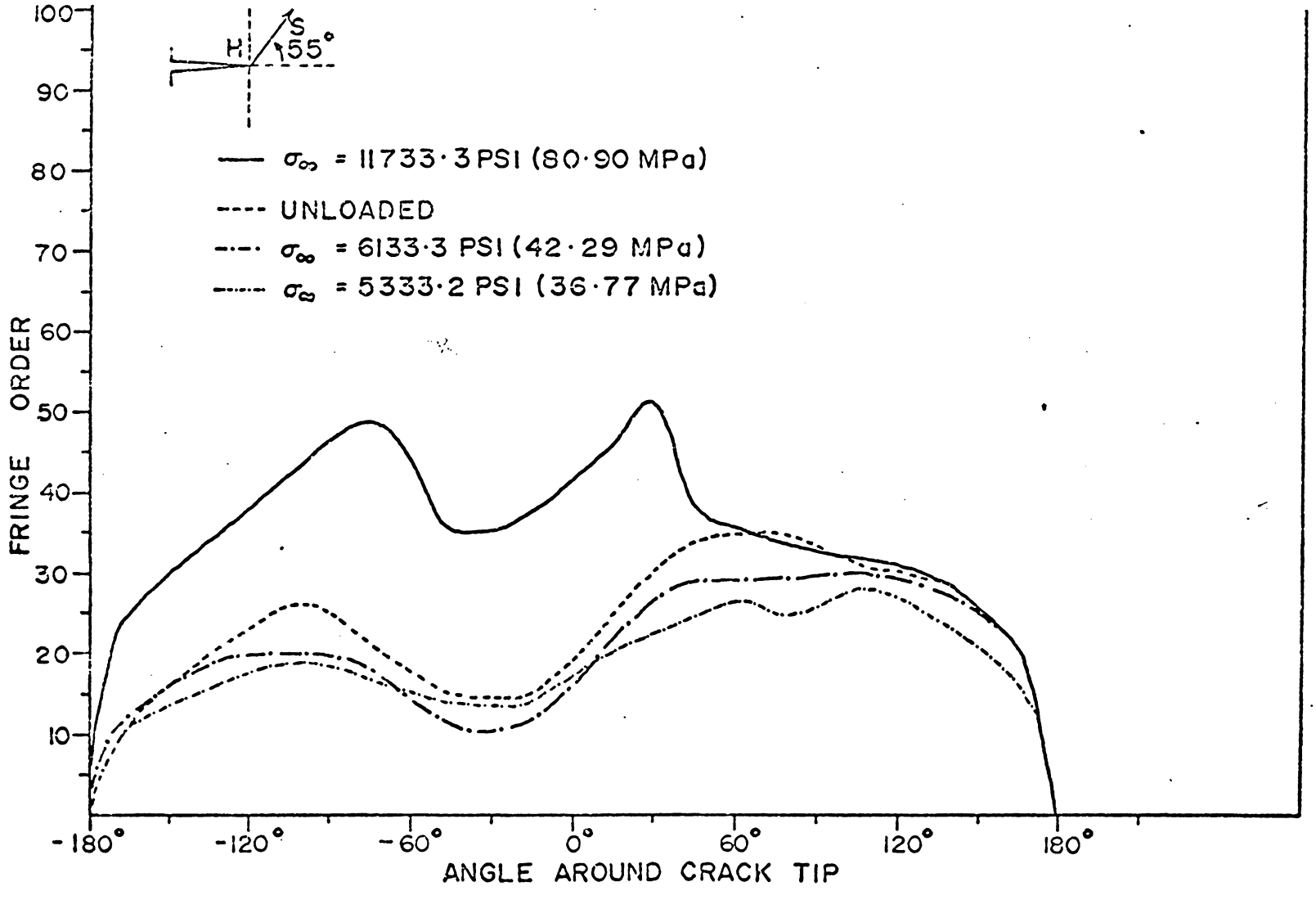

Figure 5-3. ε_z Distribution for a Loading Sequence in 2024-T3 AL (High Magnification).

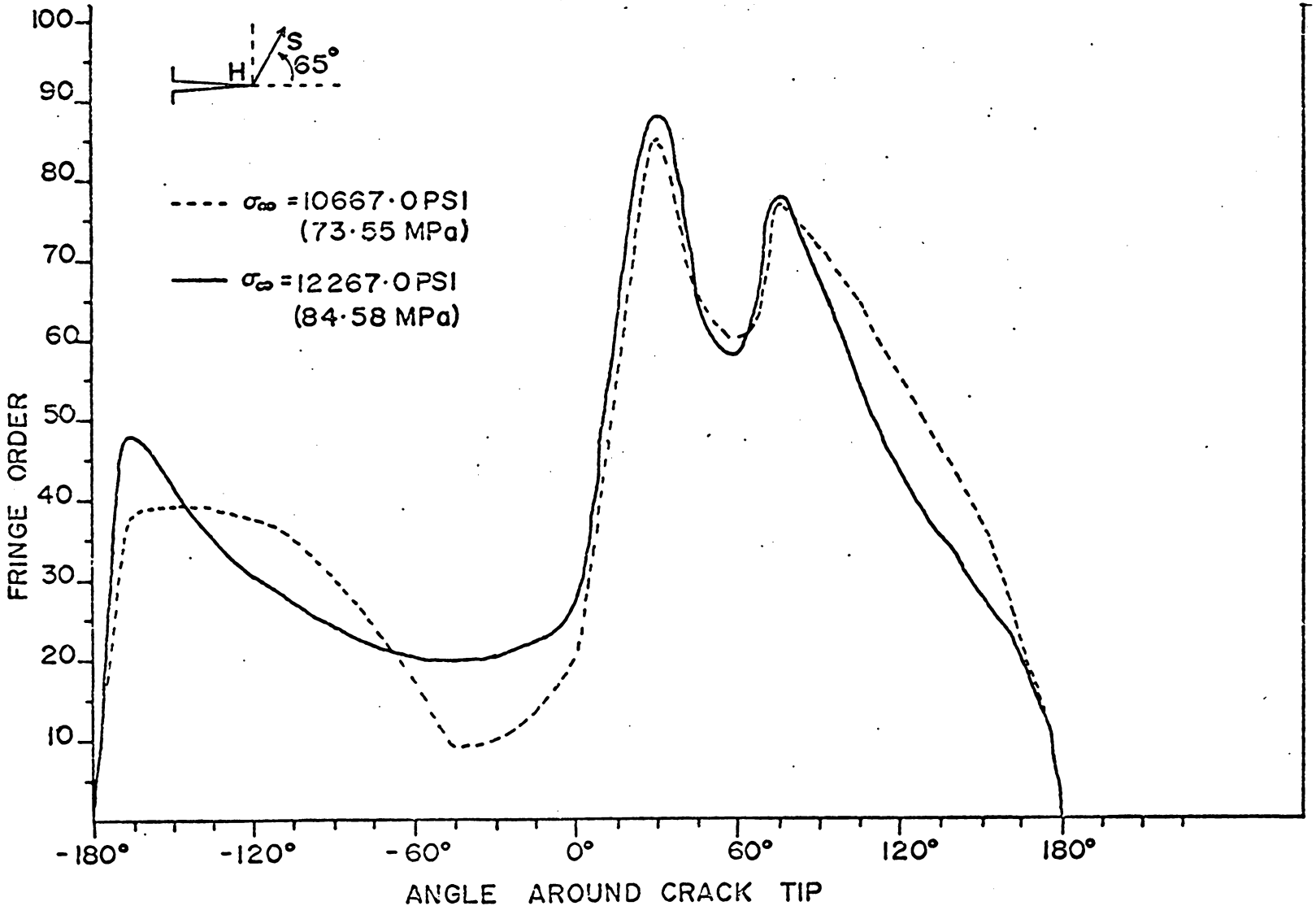

Figure 5-4. ε_z Distribution in 2024-T3 AL (Low Magnification).

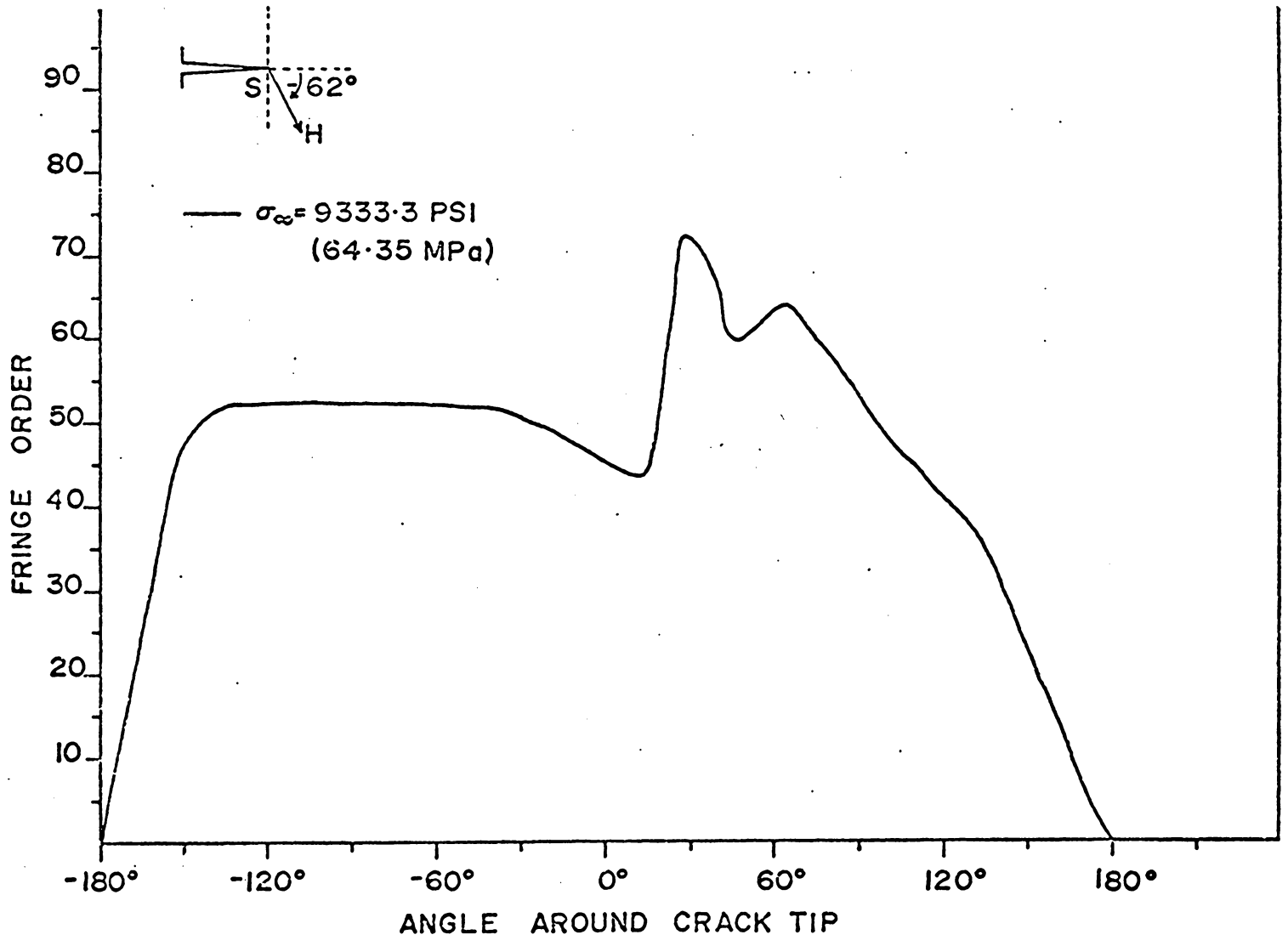

Figure 5-5. ε_z Distribution in 6061 AL (Low Magnification).

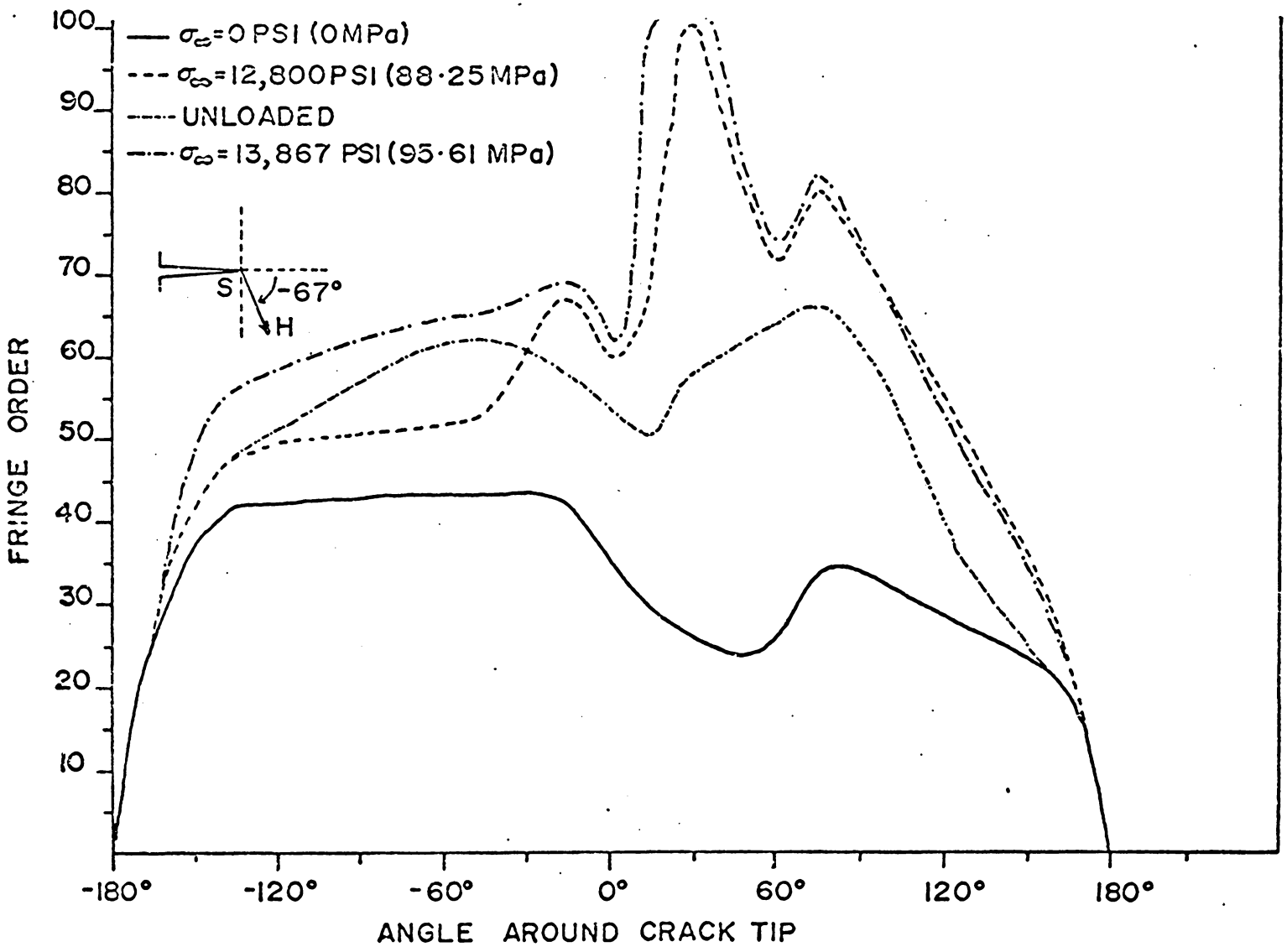

Figure 5-6. ε_z Distribution for a Loading Sequence in 6061 AL (High Magnification).

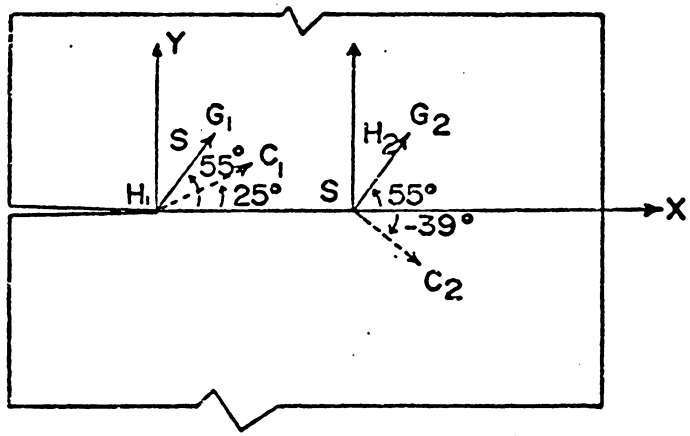

G_1 = 55° DECREASING GRADIENT

C_1 = CRACK DIRECTION 1

G_2 = 55° INCREASING GRADIENT

C_2 = CRACK DIRECTION 2

S H_1 H_2

S = SOFT

H_1 = HARD 1

H_2 = HARD 2

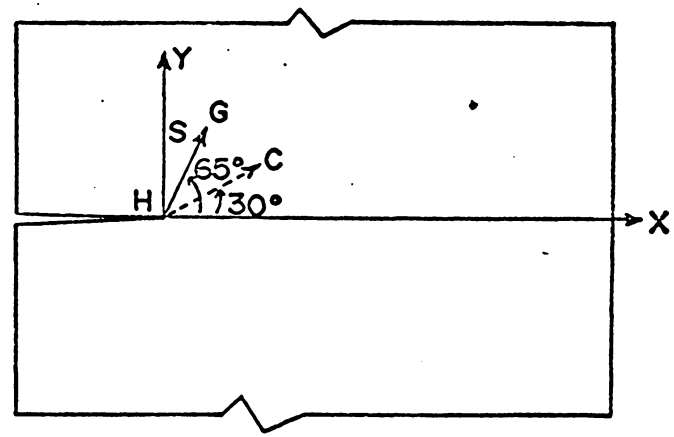

G = 65° DECREASING GRADIENT

C = CRACK DIRECTION

H = HARD

S = SOFT

Figure 5-7. Gradient Effects on Crack Propagation Direction in 2024-T3 AL.

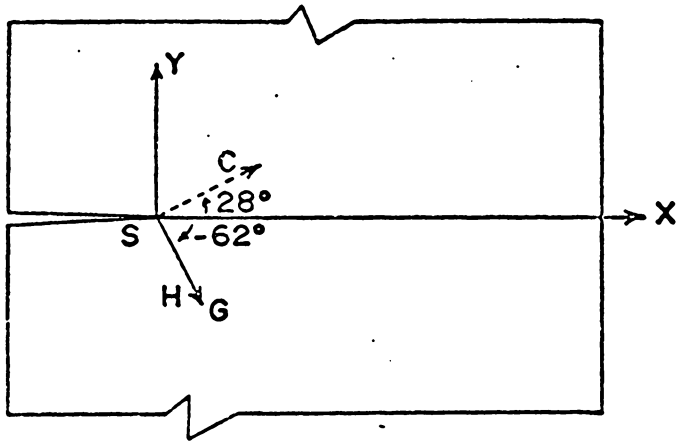

G = -62° INCREASING GRADIENT
C = CRACK DIRECTION
S = SOFT
H = HARD

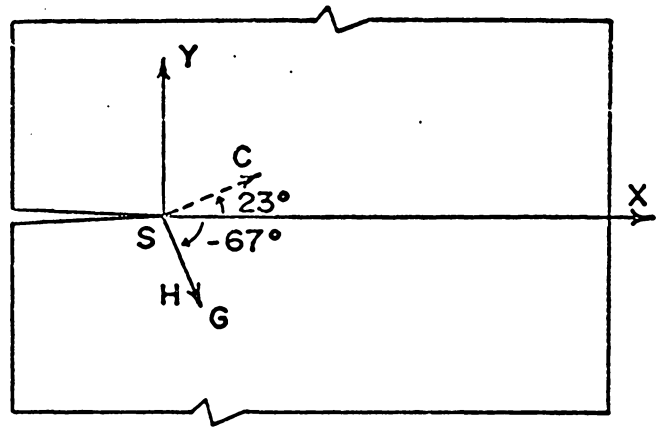

G = -67° INCREASING GRADIENT
C = CRACK DIRECTION
S = SOFT
H = HARD

Figure 5-8. Weak Gradient Effects on Crack Propagation Direction in 6061 AL.

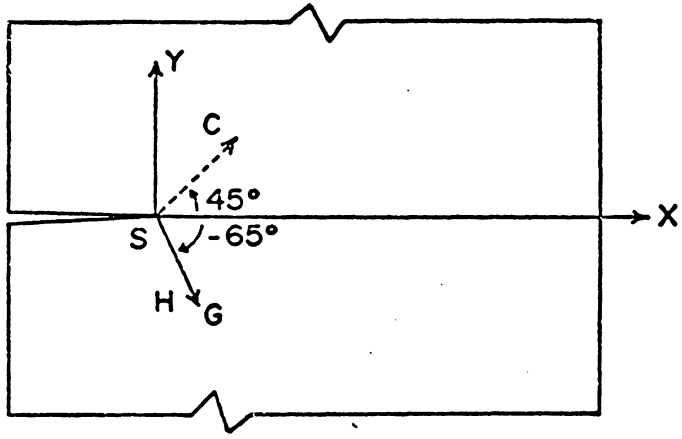

G = -65° INCREASING GRADIENT
C = CRACK DIRECTION
S = SOFT
H = HARD

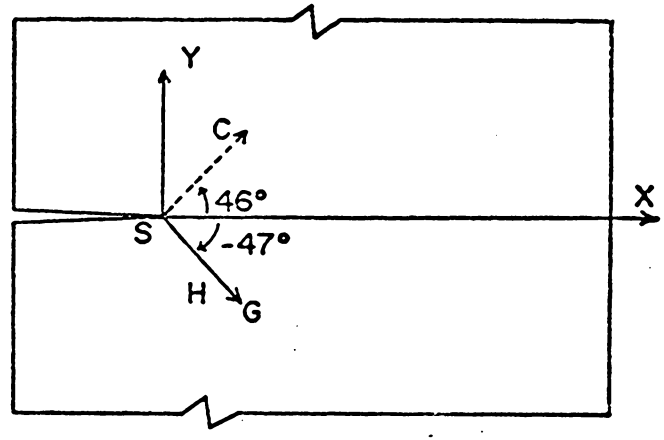

G = -47° INCREASING GRADIENT
C = CRACK DIRECTION
S = SOFT
H = HARD

Figure 5-9. Strong Gradient Effects (for Different Angles) on Crack Propagation Direction in 6061 AL.

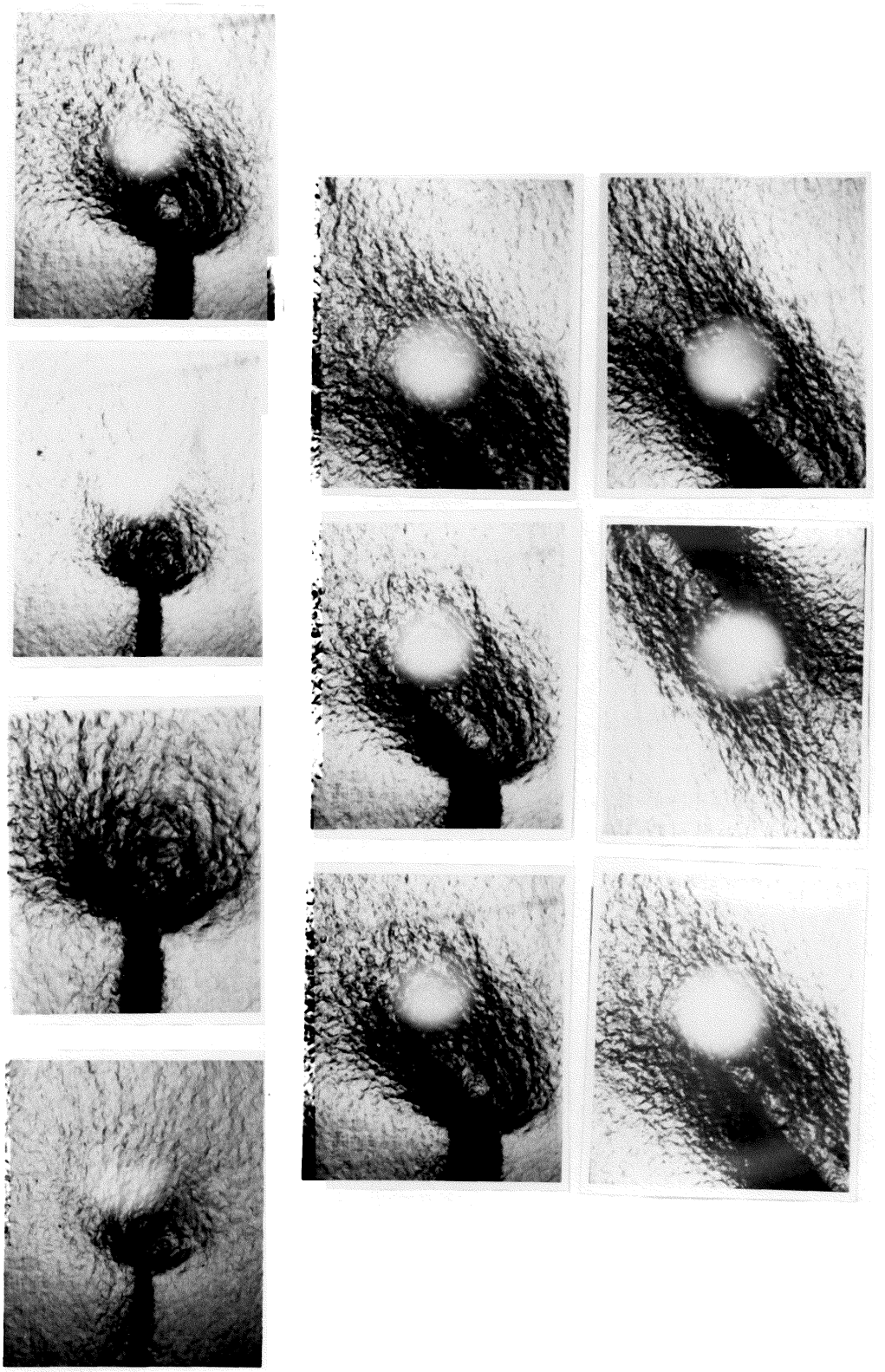

Figure 5-10. Deformation Development Pictures for 6061 AL.

was a specimen with two gradients, one decreasing and the other increasing along a +55° direction. In the decreasing gradient situation, the crack propagation direction was in the +25° direction. For the later case the crack took off at -39°. Figure 5-7b was a +65° decreasing gradient specimen and the crack direction was at a +30° angle. Figures 5-3 and 5-4 were generated from the singularities of the specimens in Figures 5-7a and 5-7b, respectively, at sub-critical crack-growth loads.

Effects of weak and strong gradients were studied by specimens represented in Figures 5-8 and 5-9. Figure 5-8a was an increasing gradient at -62° and the crack propagated at +28°. In a similar fashion, a -67° increasing gradient, with a +23° crack direction is seen in Figure 5-8b. Figures 5-8a and 5-8b are analyzed in Figures 5-5 and 5-6. Stronger gradient effects on the eventual crack propagation direction are shown in Figures 5-9a and 5-9b, for different angles of gradients.

Figure 5-10 is a deformation development sequence of pictures for the 6061 aluminum specimen described in Figure 5-9b.

5-3 DISCUSSION AND SUMMARY

Singularity analyses commonly predict crack tip stresses and strains as $r \to 0$. However, measurements in experimental investigations can only be taken at finite distances from the crack tip. The precision measurements made in this investigation cannot be taken in some arbitrarily small region near the crack tip. The data analyzed

here represent positions at a distance of approximately 0.015 inches and 0.0075 inches for low and high magnification respectively, from the crack tip. Considerable straining at the crack tip prevented any further quantitative examination of details in the smaller areas of interest.

Even though care was exercised during the heat treatment, it was not possible to ascertain exact magnitudes of the strength gradients. Hence, the results are based on relative magnitudes of the gradients.

The symmetric geometry specimen in Figure 5-1 is shown to have a nonsymmetric singularity development in Figure 5-2. It was noted that the initial patterns (before loading) for most specimens were symmetric fatigue-type displacement contours.

The loading sequence in Figure 5-3 shows prominent strain (ε_z) maxima development in the softer region along with a secondary maxima on the harder side. It can, again, be noted that the directions at which the peaks occur are markedly different with changing loads. At the lower load level, both the primary and secondary peaks develop more or less symmetrically about the crack axis, i.e., at ±105°. With increased load (nearer the fracture loads), both the peaks move towards each other. The progress of the movement is controlled by the strength of the gradient--in this case a weak decreasing gradient in the +55° direction. In the unloaded situation, residual stresses exist, and the peaks move away from each other. The initial peak positions are, however, not recovered. Reloading seems initially to

relax the strains of the unloaded situation a bit. Near the fracture loads the difference between the primary and secondary peaks rapidly increases. With the ensuing instability, the crack propagates in the direction of the limiting case of the primary peak of ε_z strain. For a (greater) angle of +65° decreasing gradient (Figure 5-4), the pattern of peak development is slightly different. Here the primary and secondary peaks develop on the soft side exclusively, with the primary maxima closer to the crack axis direction. However, only high-stress data was recorded for this case.

Very similar behavior of the peaks occurred in the increasing gradient situations. In Figures 5-5 and 5-6 both the primary and the secondary ε_z-strain maxima develop on the softer side.

Maximum relaxation ε_z strains are seen in the greater plasticity region in the unloaded condition shown in Figure 5-6. In this case, (an increasing -67° gradient), there was a pre-existing residual strain field due to severe heat treatment of the specimen. As a consequence, at the lower initial loads, the smaller peaks developed on the softer side. With higher load values both the primary and the secondary consolidated on the softer side.

At smaller angles of gradient the ε_z maxima develop on both sides of the crack axis, with the primary peak in the softer zone. With larger angles of gradient, both the primary and the secondary maximas develop on the soft side (especially at high stresses), with the primary maxima nearer the crack axis. In the case of an increasing gradient, besides the two peaks already described there is

a tertiary peak on the harder side. The tertiary peak is not evident in the decreasing gradient situation.

Figures 5-7, 5-8 and 5-9 show how the cracks eventually propagated after instability at high loading occurred. Figure 5-7a shows the bi-gradient specimen. The direction of crack propagation adjusts to the material strength variations. In all cases the crack propagates in the softer zone. For moderate increasing gradients, the crack propagates in the iso-strength direction, i.e., perpendicular to the gradient. For steep increasing gradients the crack moves away from iso-strength lines into the softer zone. Loading symmetry seems to have more effect on the decreasing gradient case.

The prominence of a sharp nonsymmetric primary singularity on the soft side was predicted by Nair and Reifsnider [42]. Again, it should be pointed out that experimental results are for finite distances from the crack tip. Further verification of these results is available from finite element analysis (to be reported soon) performed on a symmetric specimen with nonuniform material properties.

It is useful to compare an earlier analysis of crack tip defromation in materials with yield strength gradients with the present results. In that singularity analysis, Nair and Reifsnider [42] showed that the strain ε_z can be expressed as

$$\frac{\bar{\varepsilon}_z}{\bar{\bar{\varepsilon}}_y}(r,\theta) = \beta\bar{\alpha}(\theta)\, K^n \left(\frac{r}{L}\right)^{-\left(\frac{n-p}{n+1}\right)} \frac{\bar{\varepsilon}_z}{\bar{\bar{\varepsilon}}_y}(\theta) \tag{5-1}$$

where $K^n = \gamma \left(\frac{\bar{\bar{\sigma}}_s}{\bar{\bar{\sigma}}_y}\right)^{\frac{2n}{n+1}}$ (5-2)

where n is the hardening coefficient

p = yield strength variation parameter

γ = a specimen material constant

β = gradient amplitude factor

$\bar{\alpha}(\theta)$ = yield strength variation wrt. θ.

L = half crack length

$\bar{\varepsilon}_y$ = yield strain

$\bar{\sigma}^{\infty}$ = applied remote stress

$\bar{\sigma}_y$ = yield stress

Therefore,

$$\frac{\bar{\varepsilon}_z}{\bar{\varepsilon}_y}(r,\theta) = T \left(\frac{\bar{\sigma}^{\infty}}{\bar{\sigma}_y}\right)^{\frac{2n}{n+1}} \left(\frac{r}{L}\right)^{-\left(\frac{n-p}{n+1}\right)} \frac{\bar{\varepsilon}_z}{\bar{\varepsilon}_y}(\theta) \qquad (5\text{-}3)$$

where $T = \beta\, \bar{\alpha}(\theta)\, \gamma$ (5-4)

For a constant value of θ, $\bar{\varepsilon}_z(\theta)$ and $\bar{\alpha}(\theta)$ become constant.

Therefore,

$$\frac{\bar{\varepsilon}_z}{\bar{\varepsilon}_y} = T_1 \left(\frac{\bar{\sigma}^{\infty}}{\bar{\sigma}_y}\right)^{\frac{2n}{n+1}} \left(\frac{r}{L}\right)^{-\left(\frac{n-p}{n+1}\right)} \qquad (5\text{-}5)$$

where $T_1 = T \frac{\bar{\varepsilon}_z}{\bar{\varepsilon}_y}(\theta)$ (5-6)

For very large n, expression 5-5 reduces to the Hutchinsons [4] prediction,

$$\frac{\bar{\varepsilon}_z}{\bar{\varepsilon}_y} \simeq \left(\frac{\bar{\sigma}^{\infty}}{\bar{\sigma}_y}\right)^2 \left(\frac{r}{L}\right)^{-1} . \qquad (5\text{-}7)$$

Figure 5-11 is a plot of relative $\frac{\bar{\varepsilon}_z}{\varepsilon_y}$ values from equation (5-5), versus distance from the crack tip for several values of p. All curves have a common value for large r/L values. For increasing gradient cases ($-1 < p < 0$), the strain is greater near the crack tip in the crack direction. As p increases, the strain distributions flatten out indicating increasing preference for deformation away from the tip for decreasing strength gradients. In fact, for $p = n$ the curve would be flat (theoretically) indicating uniform strain values in the singular region, a situation which is unlikely to occur in a real material circumstance.

Figure 5-12 shows data taken along radii at various angles from the crack direction for a decreasing gradient in the +55° direction. In the positive 30 and 15° directions there is an increased strain development at some distance from the crack tip. A $p = 0$ curve from Figure 5-11 is included in Figure 5-12 for comparison. It should also be noted that the strain distributions in the 0 and 45° directions are similar.

Figure 5-13 is a comparison of some of the present data with earlier results by Underwood, et. al. [32]. The figure shows unloaded strain values in the crack direction as a function of distance from the crack tip. The data were matched at the extreme point from the tip to correct for the non-zero fringe order at the edge of our interference patterns. The three starred points nearest the crack tip (from the Underwood, et. al., report) have been adjusted to allow for finite root radius by extrapolating the other data, guided by

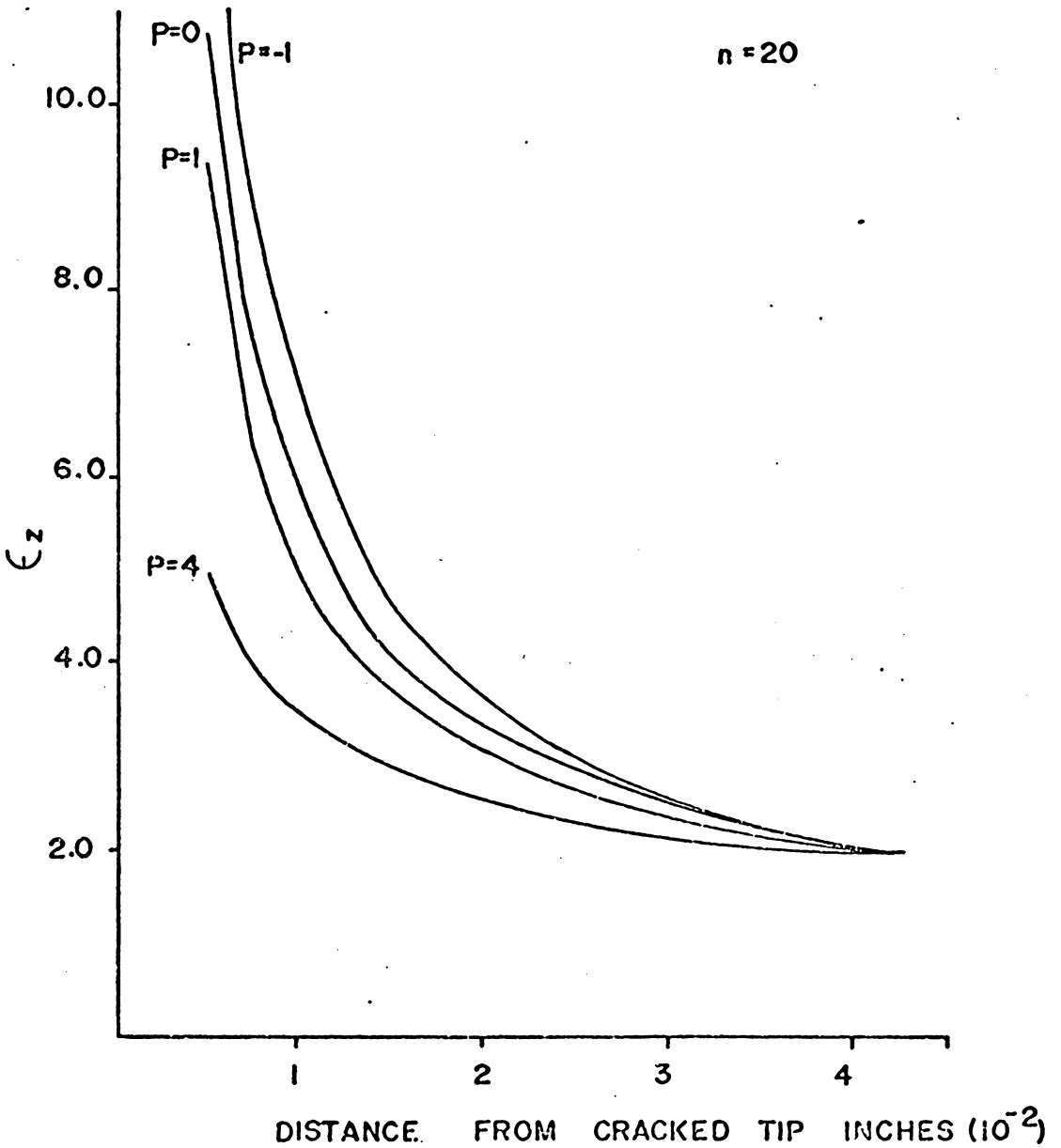

Figure 5-11. $\bar{\varepsilon}_z$ Strain (Theoretical) Distribution vs. Distance from Crack Tip.

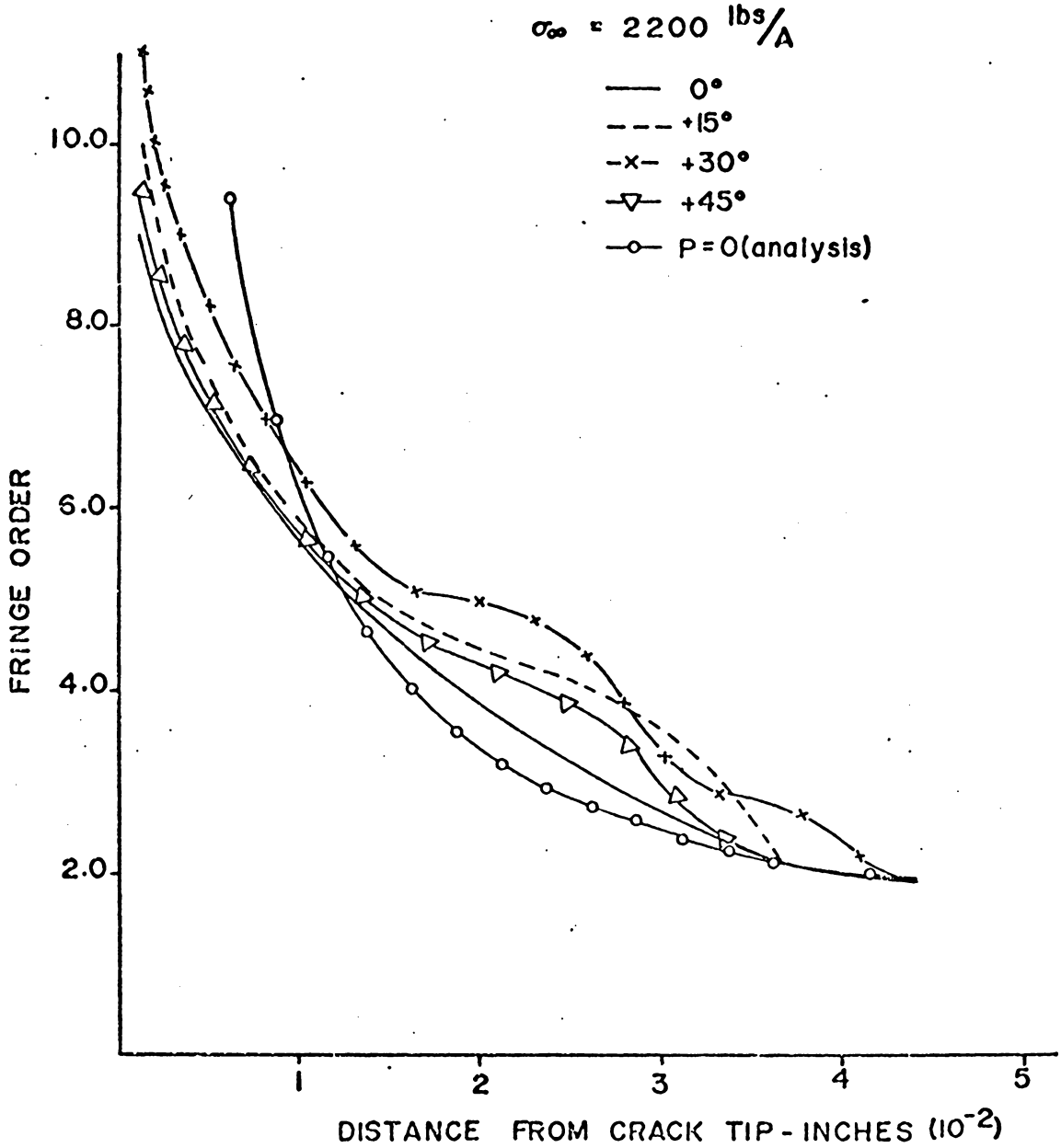

Figure 5-12. $\bar{\varepsilon}_z$ Strain (Experimental) Distributions at Various Angles to the Crack Axis vs. Distance from Crack Tip.

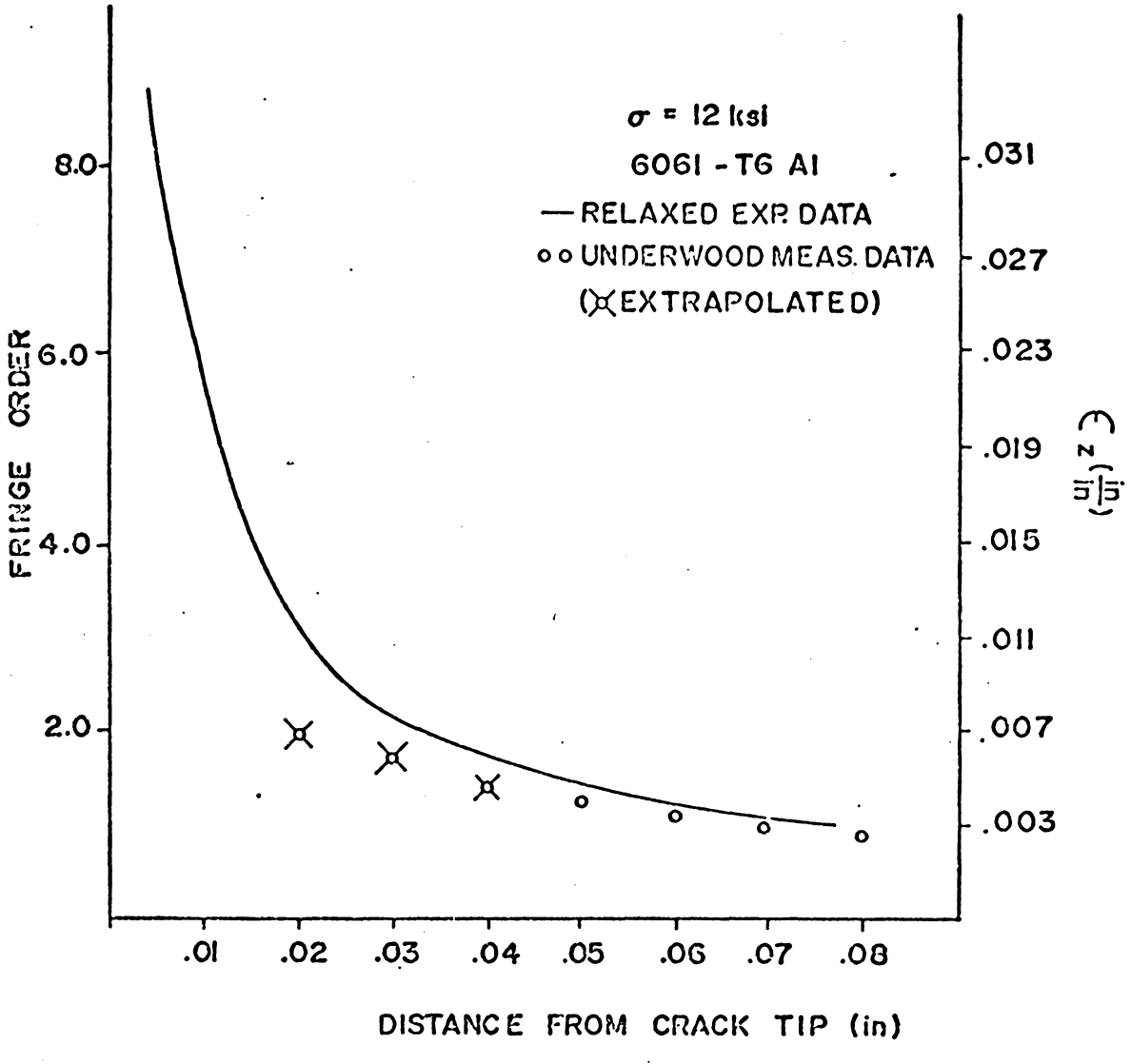

Figure 5-13. A Comparative Study of $\bar{\varepsilon}_z$ Strain Distribution.

the actual data points.

5-4 CONCLUSIONS

The present data indicate that the development of the singular stress field near a crack tip can be significantly altered by spatial variations in material yield strength. More particularly, if those variations do not occur with a symmetric distribution about the crack axis, the deformation field may not be symmetric either. The degree to which this unsymmetric deformation develops depends, at least in part, on the extent of plasticity at the crack tip. However, since the crack tip represents a singularity, the unsymmetric effects can be expected to appear in the near-tip region in any case. The analysis of Nair and Reifsnider [42] shows that these unsymmetric effects will dominate all other contributions to the deformation field in a sufficiently small region around the crack tip. Since our data were taken from a large finite region around the tip, one might expect the unsymmetric effect to become more and more prominent for our fixed level of observational magnification as the applied load is increased and greater plastic strain develops. This is, in fact, so, as seen in Figures 5-3 and 5-6. If this interpretation is valid, the relative maxima of the strain distributions should shift progressively further away from the crack axis as the remote load is increased as the unsymmetric behavior spreads into the field of view. Figure 5-3 appears to show a clear indication of that tendency. The deformation patterns can, therefore, be viewed as a superposition of

the symmetric elastic singular solution and the unsymmetric elasto-plastic solution, the latter of which contributes in proportion to the local plasticity.

The quasi-static unstable crack growth indicated in Figures 5-7 through 5-9 showed a strong tendency to propagate along iso-strength lines for the increasing gradient cases, even when that direction deviated as much as 46° from the crack axis, the maximum crack opening stress direction. The decreasing gradient appears to be less effective in "luring" the crack away from the original crack axis than the increasing gradient is in "forcing it aside." Deviations of 30° were caused, however, so that significant effects did appear. It should be mentioned that the quasi-static crack propagation was observed carefully through the microscope. In all cases the crack propagated in an unstable manner, advancing in abrupt jumps as the load was increased. No evidence of a tearing process could be observed in the microscope.

Figures 5-11 and 5-12 bring another important point to light. The inflection point in the strain values at some distance from the crack tip for the 15° and 30° case cannot be represented by a variables-separable equation, such as the classical form:

$$\varepsilon_{ij} = K_{\varepsilon} \frac{1}{r^m} \bar{\varepsilon}_{ij}(\theta) \ . \qquad (5\text{-}8)$$

Hence, while an asymptotic solution of that form may well be satisfactory quite near the crack tip, it will not represent reality throughout the region influenced by the singularity in this case.

There is a related point of considerable importance. It is possible that, in the region where 5-8 fails, the local stresses and strains may not be proportional to the applied load in which case deformation theory plasticity could not be used as a complete model of the plastic deformation. There is no direct evidence in this report that this is the case, only that proportional loading expressions such as 5-8 are inadequate. However, Figure 5-12 shows that the asymptotic solution of Nair and Reifsnider [42] is not an unreasonable approximation to the strains. A decreasing gradient curve ($p = 4$, for example) would have fit the near tip data better as it should since the data is for a decreasing strength case.

CHAPTER VI

DISCUSSION AND CONCLUSIONS

Most materials of engineering interest display some ductility when fractured. As yet, there is no precise analysis to account for the ductility under completely general conditions. The need, therefore, exists, to sustain efforts towards a better understanding of real material response at fracture.

One of the most serious misrepresentations of real materials by ideal models is the assumption of uniform material properties. A great number of fracture problems arise where this is simply not true. Common examples include cracks starting at welds, or joints, or surfaces and flaws developed in manufactured members affected by forging and forming, and further influenced by service conditions including radiation, temperature and aggressive chemical environments.

In the previous chapters a comprehensive study of the effects of non-uniform material properties on crack tip deformation fields was undertaken.

The essential highlights of the investigation can be summarized as follows.

1. It has been shown that the concept underlying Irwin's 'small-scale yielding correction factor (r_y)' can be extended to provide a very useful method for using a finite element technique to analyze problems involving plasticity at crack tips, i.e., Unimod.

That method appears to provide very good data under widely varying conditions and has numerous computational advantages, namely, it is simple, easily used, quick, versatile, with respect to geometry changes, and above all easy to understand.

2. It has been shown that severely unsymmetric nonlinear deformation fields can develop in crack tip regions if material strength variations occur in directions other than the crack axis.

3. It has been shown that these unsymmetric effects can dominate local near-tip deformation fields at all levels of applied stress in a sufficiently small region near the crack tip.

4. It has been shown that these unsymmetric effects become more dominant for materials which do not strain harden much during their plastic response.

5. It has been shown that the maxima of the major load (crack opening) stress can be shifted away from 0° to as high as 90° by a symmetric property gradient, raising the possibility of a crack turning away from the 0° direction even in a symmetric case.

6. It has been shown that the field stress (strain) amplitude, singular nature of the local stress (strain) field (r dependence) and the θ dependence of the stresses (strains) are all significantly altered by gradients of material strength, even for small scale yielding.

7. A considerable amount of experimental evidence has been generated which supports, in general, the above predictions concerning the unsymmetric deformation fields.

8. The investigation revealed some experimental evidence that the proportional representation of stress and strain distributions is not possible in some cases, i.e., the classical form

$$\sigma_{ij} = \frac{K}{r^m} f_{ij}(\theta)$$ is not completely representative in general.

On the basis of these results it would appear that:

9. Any fracture behavior influenced by local nonlinear deformations, especially fatigue and crack nucleation, would be expected to be greatly affected by the details of this investigation.

10. A proper treatment of nonlinear local behavior is not a simple extension of linear elastic fracture mechanics.

11. While the F.E.M. is helpful for gross calculations in practical situations, it must be complemented by closed form solutions to get information close to the crack tip where the deformation most critical to the fracture process is occurring.

12. Increasing and decreasing strength cases are not simple inverses of each other analytically or experimentally; they are quite distinct.

Additional, possible and extensional work that should be done with respect to the actual effect on fracture are:

--when is a crack actually arrested or advanced by these effects?

--when does a crack tend to develop along a material boundary?

--how does the strength and toughness trade-off enter into these considerations?

--can these effects significantly influence fracture for plain strain conditions?

The results and methods developed here appear to have immediate applications in the fracture analyses of nuclear reactor components. Also, intensive investigations are underway by various other investigators, including Benet Laboratories, Watervliet, New York, to apply these and other related results to the understanding of crack behavior in laminated composites.

REFERENCES

[1] Larsson, S. G. and Carlsson, A. J., J. Mech. Phys. Solids, Vol. 21, 263, 1973.

[2] Rice, J. R., "Limitations to the Small Scale Yielding Approximation for Crack Tip Plasticity", J. Mech. Phys. Solids, Vol. 22, pp. 17 to 26, (1974).

[3] Hutchinson, J. W., "Plastic Stress and Strain Fields at a Crack Tip", J. Mech. Phys. Solids, Vol. 16, 1968, pp. 337-347.

[4] Hutchinson, J. W., "Singular Behavior at the End of a Tensile Crack in a Hardening Material", J. Mech. Phys. Solids, Vol. 16, 1968, pp. 13-31.

[5] Rice, J. R. and Rosengren, G. F., "Plane Strain Deformation Near a Crack Tip in a Power-Law Hardening Material", J. Mech. Phys. Solids, Vol. 16, 1968, pp. 1-12.

[6] Hilton, P. D. and Hutchinson, J. W., "Plastic Intensity Factors for Cracked Plates", Engn. Frac. Mech., Vol. 3, 1971, pp. 435-451.

[7] Knowles, J. K. and Sternberg, Eli, "An Asymptotic Finite-Deformation Analysis of the Elastostatic Field Near the Tip of a Crack," Technical Report No. 27, California Inst. of Technology, 1973.

[8] McGowan, J. J. and Smith, C. W., "A Finite Deformation Analysis of the Near Field Surrounding the Tip of Crack-like Ellipses", VPI-E-74-10, College of Engineering, VPI&SU, May 1974.

[9] Rice, J. R., "A Path Independent Integral and the Approximate Analysis of Strain Concentration by Notches and Cracks", J. of App. Mechanics, pp. 379-386, June 1968.

[10] Sih, G. C., "Methods of Analysis and Solutions of Crack Problems", Mechanics of Fracture I, edited by G. C. Sih, p. xxi, 1973.

[11] Pu, S. L., Scanlon, R. D. and Hussain, M. A., "Stress Singularities Associated with a Crack Inclined to a Bi-Material Interface", Development in Mechanics, Proceedings of the 13th Midwestern Mechanics Conference, Vol. 7, 26, pp. 349-364.

[12] Chan, S. K., Tuba, I. S. and Wilson, W. K., "On the Finite Element Method in Linear Fracture Mechanics", Engr. Fracture Mech., 2, pp. 1-17, 1970.

[13] Hayes, D. J., "Some Applications of Elastic Plastic Analysis to Fracture Mechanics", Ph.D. Thesis, Imperial College of Science and Technology, 1970.

[14] Kobayashi, A. S., Chiu, S. T., and Beeuwkes, R., "A Numerical and Experimental Investigation on the Use of J-Integral", A Report.

[15] Barone, M. A. and Robinson, A. R., "Approximate Determination of Stresses near Notches and Corners in Elastic Media by an Integral Equation Method", Univ. of Illinois Civil Engr. Studies, Structural Res. Ser., No. 374, 1971.

[16] Rice, J. R., "Some Remarks on Elastic Crack Tip Stress Fields", Brown Univ. Tech. Report, NGL 40-002-080/5 to NASA, 1971.

[17] Wilson, W. K., "On Combined Mode Fracture Mechanics", Westinghouse Research Laboratory, Research Dept. 69-IE7-FMECH-R1, Pittsburgh, 1969.

[18] Byskov, E., "The Calculation of Stress Intensity Factors Using the Finite Element Method with Cracked Elements", Int'l. J. Fracture Mech., 6, pp. 159-167, 1970.

[19] Tracey, D. M., "Finite Elements for Determination of Crack Tip Elastic Stress Intensity Factors", Engr. Fracture Mech.

[20] Levy, N., Marcal, P. V., Ostergren, W. J. and Rice, J. R., International J. of Fracture Mechanics, 7, pp. 143-156, 1971.

[21] Rice, J. R. and Tracey, D. M., "Computational Fracture Mechanics", Numerical and Computer Methods in Structural Mechanics, edited by S. J. Fenves et al.

[22] Tracey, D. M., "On the Fracture Mechanics Analysis of Elastic-Plastic Materials Using the Finite Element Method", Ph.D. Thesis, Brown University, Providence, 1973.

[23] Verette, R. M. and Wilhem, D. P., "Development and Evaluation of Methods of Plane Stress Fracture Analysis", Tech. Rept. AFFDL-TR-73-42, May 1973.

[24] Kawata, K., "Analysis of Elasto-Plastic Behavior of Metals by Means of Photoelastic Coating Method", Jnl. Sci. Res. Inst., Tokyo, 52, 17-40 (1958).

[25] Dixon, J. and Visser, W., "An Investigation of the Elastic-Plastic Strain Distribution Around Cracks in Various Sheet Materials", Proc. Internat. Symp. Photoelasticity, Chicago, 1961.

[26] Ault, R. and Spretnak, J., "Initial Yielding and Fracture in Notched Sheet Molybdenum", Report ASD-TDR 62-223, Wright Field, April 1962.

[27] Post, D., "Photoelastic Stress Analysis for an Edge Crack in a Tensile Field", Proceedings, Soc. of Experimental Stress Analysis, Vol. 12, No. 1, pp. 99-116, 1954.

[28] Fessler, H. and Mansell, D. O., "Photoelastic Study of Stresses Near Cracks in Thick Plates", J. Mech. Eng. Sc., Vol. 4, No. 3, pp. 213-225, Sept. 1962.

[29] Smith, D. G. and Smith, C. W., "Photoelastic Determination of Mixed Mode Stress Intensity Factors", VPI-E-70-16 Report, June 1970.

[30] Gerberich, W. W., "Plastic Strains and Energy Density in Cracked Plates: I. Experimental Technique and Results", Expt. Mech., Vol. 4, No. 11, pp. 328-335, 1964.

[31] Hahn, G. T. and Rosenfield, A. R., "Local Yielding and Extension of a Crack Under Plane Stress", Acta Metallurgica, Vol. 13, March 1965.

[32] Underwood, J. H., Swedlow, J. L. and Kendall, D. P., "Experimental and Analytical Strains in an Edge-Cracked Sheet",

Benet R. & E. Laboratory, Technical Report WVT-6933, Sept. 1969, Watervliet, N. Y.

[33] Barenblatt, G. I., Adv. in Appl. Mech., New York: Academic Press, p. 55, 1962.

[34] Bilby, B. A., Cottrell, A. H. and Swinden, K. H., "The Spread of Plastic Yield from a Notch", Proc. Roy. Soc., A 272, pp. 304-314, 1963.

[35] Kahl, M. and Reifsnider, K., "Influence of Local Variations of Yield Strength on Plastic Zones at Crack Tips", Engn. Frac. Mech., Vol. 4, 1972, pp. 653-664.

[36] Reifsnider, K. and Kahl, M., "The Effect of Local Yield Strength Gradients on Fatigue Crack Propagation", VPI-E-73-4, College of Engineering, Virginia Polytechnic Institute and State University, Blacksburg, Virginia.

[37] Carroll, W. E., "An Optimum Idealizations in Discrete Element Analysis", Doctoral Dissertation, Dept. of Engr. Sci. & Mech., VPI&SU, 1971.

[38] McClintock, F. A., "Effects of Root Radius, Stress, Crack Growth and Rate on Fracture Instability", Proc. Roy. Soc. A285, pp. 58-72, 1965.

[39] McClintock, F. A. and Irwin, G. R., "Plasticity Aspects of Fracture Mechanics", Fracture Toughness Testing and Its Applications, STP No. 381 ASTM, pp. 85-113, 1964.

[40] Wilson, E. L., "Finite Element Analysis of Two Dimensional Structures", Ph.D. Dissertation, University of California, Berkeley, Calif., 1963.

[41] Reifsnider, K. and Nair, P., "Unimod: An Applications-Oriented Finite Element Scheme for Fracture Mechanics Analysis", VPI-E-73-18, Report, April 1973.

[42] Nair, P. and Reifsnider, K., "Unsymmetric Deformation Fields in Symmetric-Geometry Specimens with Non-Uniform Properties", Developments in Theoretical and Applied Mechanics, vii SECTAM, edited by M. Chi and S. R. Heller, pp. 183-196, 1974.

The vita has been removed from the scanned document

INVESTIGATION OF NONLINEAR CRACK TIP DEFORMATION INCLUDING THE EFFECTS OF UNSYMMETRIC SPATIAL VARIATIONS OF MATERIAL PROPERTIES

by

Prasad K. Nair

(ABSTRACT)

An extensive investigation of non-uniform material effects on static fracture analyses is undertaken. Included in the study are theoretical, experimental and numerical techniques of focusing attention on the nonsymmetric deformation fields around a crack tip in a non-uniform yield strength varying material. Each analysis independently shows that the material non-uniformities alter stress and strain distributions drastically and that a statically stressed crack can propagate in directions other than the crack axis direction, depending on local conditions at the crack tip. An extremely simple and versatile finite element technique called "Unimod" is developed for use in real material modelling of crack tip material elements.